Department of Precision and Microsystems Engineering

Predicting the elastic properties of lattice materials, a geometrically nonlinear approach

Demi van Megen

Report no : 2022.007
Coach : Dr. Can Ayas
Professor : Prof.dr.ir. A. van Keulen
Specialisation : Engineering Mechanics
Type of report : Master thesis
Date : February 23, 2022

TU Delft Delft University of Technology

Predicting the elastic properties of lattice materials, a geometrically nonlinear approach

by

Demi van Megen

A thesis submitted to
Delft University of Technology,
Mechanical, Maritime and Material Engineering (3ME),
Precision and Microsystems Engineering (PME).

In partial fulfillment of the requirements for the degree of
Master of Science,

to be defended publicly on Thursday March 3, 2022 at 15:00 CET.

Student number:	4372255	
Project duration:	October, 2020 – March, 2022	
Thesis committee:	Prof. dr. ir. A. van Keulen,	TU Delft
	Dr. C. Ayas,	TU Delft, supervisor
	Ir. J.M. van der Zwet,	TU Delft

An electronic version of this thesis is available at `http://repository.tudelft.nl/`.

TU Delft

Abstract

In recent studies, selection criteria for lattice materials suitable for active shape-morphing have been composed. These criteria have directly resulted in the proposal of a lattice that is able to compete with the Kagome lattice, which in the literature is identified as a lattice material with optimal in-plane stiffness and shape-morphing capabilities. The selection of suitable lattice materials is mostly related to the properties of the lattice before shape-morphing. Naturally the question 'What is the effect of morphing on the macroscopic properties of the lattice material?' arises.

This research investigates the relationship between kinematic properties of the pin-jointed Kagome truss and elastic macroscopic properties of the welded-jointed Kagome lattice during deformation. The kinematic properties of the Kagome truss are explored at all possible collapse configurations. The same collapse configurations of the pin-jointed truss are then used to determine the elastic response of the welded-jointed twisted lattice with the use of the commercial finite element program ABAQUS.

The results show that only the pin-jointed initial configuration of the Kagome truss can support all macroscopic loads without inducing a collapse of the truss, no other pin-jointed configuration shares this property. Indicating different elastic responses of the initial welded-jointed lattice and the twisted lattices. The results of the finite element analysis support this finding, as it can be shown that the type of deformation of the initial configuration of a welded-jointed lattice differs from the deformation of any other twisted configuration. A stark difference between Young's modulus is observed between the initial configuration and the twisted configurations. The deformation induced by single member actuation creates a weak layer in the lattice. Therefore the attractive properties of the Kagome lattice are not preserved during shape-morphing.

Acknowledgements

This thesis was written to fulfill the program of the track High-Tech engineering within the master Mechanical Engineering at the Delft University of technology. The study aims to contribute to the ongoing research field of lattice materials.

I have received a great deal of support and guidance throughout the writing of this thesis. I'd like to express my deepest gratitude to my supervisor dr. Can Ayas. Without your patient and kind guidance I would not have been able to complete this thesis. This one is for you Can, Ty Ty!

I'd also like show my appreciation for my friends. Who have helped me during my project whenever I got stuck on my project by sometimes providing advice and mostly providing happy distractions. In addition, I would also like to thank my parents for their support during this period in my life. Special mention to my 41 plants, who have kept me company during the long days of the pandemic, I'm glad most of you were cacti.

Demi van Megen
Delft, February 2022

Contents

1. Introduction

1.1 Lattice materials

Lattice materials are a subclass of cellular solids. They are made up of a large number of uniform lattice elements, that are slender beams or rods. Lattice materials are generated by tessellating a periodic unit cell throughout space [6]. Consequently, a repetitive micro-architecture is attained unlike other cellular solids e.g. open cell foams. The term lattice material is used to emphasize that these tessellated lattices can be treated as a homogenised continuum with effective macroscopic *material* properties such as elastic moduli and yield strength when the dimension of the lattice is orders of magnitude larger than the unit cell itself [1].

A lattice material can be referred to as a 2D lattice if the out-of-plane thickness is much smaller than the in-plane dimensions. Lattices that conform to this requirement can be modelled assuming plane stress conditions [2].

Relative density $\bar{\rho}$ is commonly used to compare the properties of cellular solids. In lattice materials it can be determined by the volume fraction of the unit cell occupied by the rods. In 2D, considering the rods with identical rectangular cross-sections and neglecting the size of the joints, it is equal to the sum of the rods lengths $l^{(i)}$ multiplied by the in-plane rod width w, divided by the unit cell area A_c:

$$\bar{\rho} = \frac{1}{A_\mathrm{c}} \sum_{i=1}^{N} l^{(i)} w \tag{1.1}$$

where N is the number of rods in the unit cell [11].

A 2D lattice comprising isotropic material is not by definition in-plane isotropic itself, rather the micro-architecture determines whether a lattice material can be considered isotropic or not. In-plane symmetry can be used instead to determine if a lattice is in-plane isotropic, in-plane orthotropic or in-plane anisotropic. A lattice with fourfold symmetry will be in-plane orthotropic and a lattice with a threefold or sixfold symmetry will be in-plane isotropic [2].

The macroscopic properties of a lattice are dictated by three factors, namely: material properties of the rod material, relative density $\bar{\rho}$, and the micro-architecture of the unit cell [1].

1.1.1 Shape morphing

A possible application for lattice materials is shape morphing. The structure will take on a predetermined shape in response to stimuli such as temperature changes or internal actuation. In 2D lattices a few rods in the lattice will be replaced with actuators that can extend or shorten, impacting the shape of the lattice. Ideally, the lattice material features high macroscopic elastic moduli and strength so that it will remain stiff when loaded by external macroscopic loads, while being compliant when the actuators are deployed.

Pronk *et al.* [15] proposed a set of design criteria for 2D lattices, in order to find lattice materials that are able to full fill the requirement of being stiff to macroscopic external forces while at the same time being compliant to actuation.

1.1.2 Pin-jointed trusses

This thesis will discuss both pin-jointed trusses and rigidly-jointed lattices. Lattice materials are rigidly-jointed but their mechanical responses can be traced back to the response of their pin-jointed counterparts.

Pin-jointed trusses have smooth frictionless joints and can exhibit collapse mechanisms. Subfigure 1.1(a) shows a truss that has a mechanic. Applying a tensile force on the top right node and the bottom left node will result in the beams rotating around the pins, therefore the frame collapses with no resistance. A welded-jointed equivalent lattice cannot rotate around the joints and will therefore bend the beams when the same load is applied. The welded-jointed lattice reacts in a bending-dominated manner.

Subfigure 1.1(b) will not collapse if a load is applied to the truss, it will remain square. The welded-jointed equivalent lattice will therefore stretch the beams when a tensile load is applied. The welded-jointed lattice is therefore stretching-dominated. Lattices that are stretching-dominated will have a higher macroscopic stiffness than lattices that are bending-dominated. This is due to the axial stiffness being higher than the bending stiffness of slender beams.

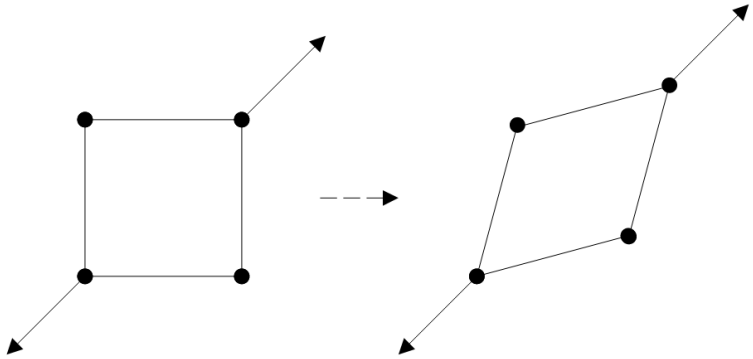

(a)

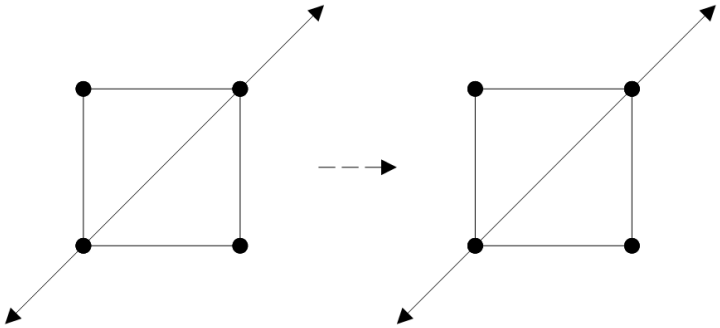

(b)

Figure 1.1: (a) A pin-jointed truss containing a collapse mechanism. (b) A pin-jointed truss that is considered rigid.

1.2 Lattice micro-architectures

The most important lattice micro-architecture for this research will be the Kagome lattice. This is due to the fact that it has very favourable properties and is a relatively simple structure making it the ideal structure for a thorough investigation.

1.2.1 The Kagome lattice

The Kagome lattice has been extensively studied in the literature. Hyun and Torquato (2002) [10] have shown that the rigidly-jointed Kagome lattice has optimal in-plane stiffness when compared to isotropic lattices with bars of equal lengths. Hutchinson and Fleck (2005) [8] explored the stiffness and strength of the rigidly-jointed Kagome lattice, and have demonstrated shape morphing capabilities. And the excitation of a finite mechanism of the pin-jointed Kagome truss was studied by Hutchinson and Fleck (2006) [9].

It was noted by Hutchinson and Fleck (2006) [9] that a close link exists between the pin-jointed Kagome truss, the triangular-triangular truss (T-T) and the fully triangular truss. A finite collapse mechanism with a single degree of freedom, shown in figure 1.2, causes the pin-jointed Kagome truss to collapse into the triangular-triangular configuration. It can even be taken further where the collapse approaches the fully triangular configuration. The full collapse can of course only happen in theory as the full collapse would require a jump in connectivity of the nodes from 4 to 6. The collapse of the truss is accompanied by a decrease in unit cell area due to the movement of the bars, without the lengths of the bars changing.

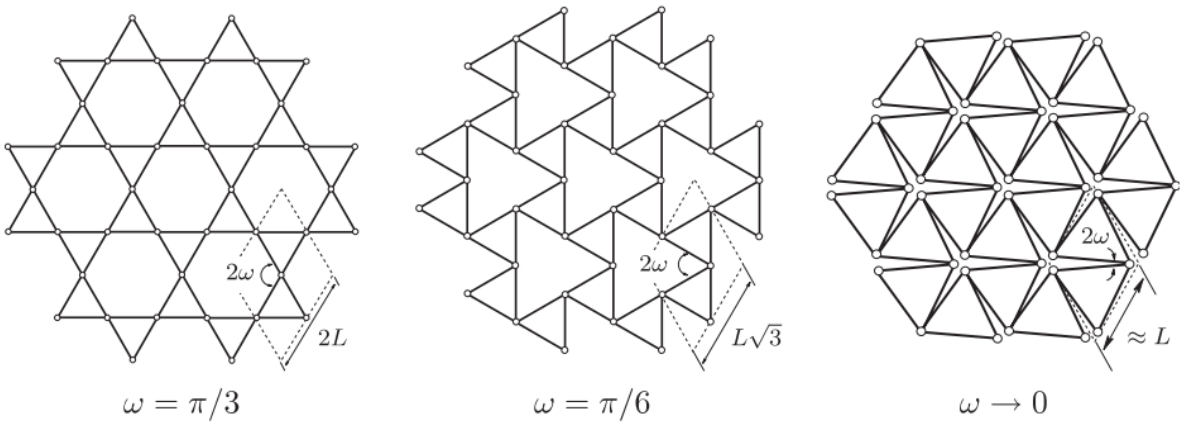

Figure 1.2: Finite mechanism that links the Kagome truss, the T-T truss and the fully triangular truss, reproduced from Hutchinson and Fleck (2006) [9].

The collapse mechanism cannot be triggered by a macroscopic load when the truss is in the Kagome configuration. This is not the case however for the T-T configuration.

1.2.2 The fully triangular lattice

The pin-jointed fully triangular truss, see figure 1.3, has no collapse mechanism. The welded-jointed lattice has also been compared to the welded-jointed Kagome lattice when it comes to the actuation energy requirement. According to Wicks and Guest [17] the welded-jointed fully triangular lattice requires significantly more energy to actuate a single bar than the welded-jointed Kagome lattice for the same relative density.

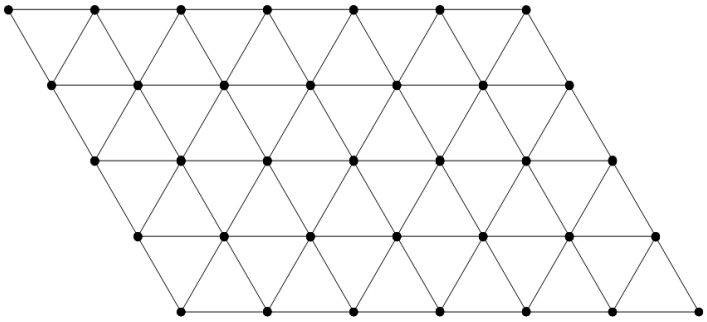

Figure 1.3: The fully triangular lattice

1.2.3 The novel lattice architecture by Nelissen *et al.*

Four novel lattice architectures were proposed by Nelissen *et al.* [12] in accordance with the design criteria created by Pronk *et al.* [15]. One of these lattices will be mentioned in this thesis. This will be the Kagome with concentric hexagons lattice or (KH). This lattice will be briefly analyised in appendix A.

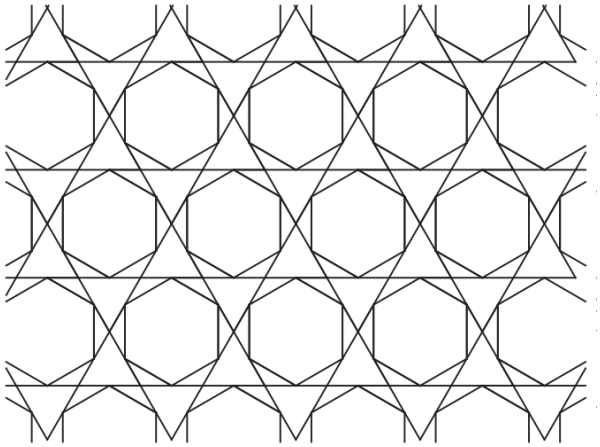

Figure 1.4: The Kagome with concentric hexagons lattice (KH) reproduced from Nelissen *et al.* [12].

1.3 Motivation

Pronk *et al.* [15] investigated in his work 'what makes a lattice suitable for actuation?' In his search to answer this question he compared two lattices, namely the Kagome lattice and the hexagonal cupola lattice. By comparing these lattices he also tried to find search criteria to find other lattice architectures that might be able to compete with the Kagome lattice, which is in the literature suggested to have excellent macroscopic properties while also having the capability to preform shape-morphing. His investigation resulted in the formulation of several design criteria.

Nelissen *et al.* [12] used these criteria to propose four novel lattice architectures. Comparing these novel architectures with the Kagome lattice resulted in a few conclusions. First, lattices that are able to compete with the Kagome lattice in terms of macroscopic properties and actuation properties exist. Second, the design criteria formulated by his predecessor are both overly constrictive as well as insufficient. These criteria have not been expanded on as of this writing. Both of the previous works only considered the initial configuration for both the macroscopic properties and the shape-morphing properties of a rigidly-jointed lattice.

The type of collapse mechanism of the pin-jointed truss is linked to the deformation behaviour of the welded-jointed lattice, influencing the macroscopic properties. This results in the following question. As the bending- and stretching-dominated properties of the rigidly-jointed lattice are linked to the collapse mechanisms of pin-jointed trusses, what is the effect of deformation on the rigidly-jointed lattice on the overall macroscopic properties, such as the Young's modulus and the Poisson's ratio?

To answer this question the Kagome lattice will be studied. Firstly, a novel matrix method will be used to investigate if the initial mechanism is preserved for a pin-jointed truss during a finite collapse and if it is not then where is this mechanism lost and what are the implications for the truss? Secondly, the commercial finite element package ABAQUS will be employed to compare the elastic macroscopic properties of the welded-jointed initial configurations to the welded-jointed configurations containing an angle of initial twist.

1.4 Outline

This thesis will be structured in the following manner, in order to answer the question raised in the previous section:

Chapter 2 will be used to get a deeper understanding of the pin-jointed Kagome truss and its collapse mechanism. How is this mechanism found and is this a finite mechanism to begin with as would be suggested by Hutchinson and Fleck [9]?

Chapter 3 continues with the results found in chapter 2 and expands the current matrix method, creating a novel nonlinear method. This novel method will be used to explore the characteristics of the mechanism during the collapse of the pin-jointed truss. Will the initial characteristics stay the same if the mechanism is excited, or will they change? And if the characteristics change when does this change occur?

Chapter 4 will entail the calculation of the macroscopic Young's modulus and Poisson's ratio for the welded-jointed Kagome lattice. Building further upon the knowledge, established in the previous chapter, that the configurations will not behave in the same way. In this chapter it will become clear what impact this change in behaviour has on the macroscopic Young's modulus and the Poisson's ratio of the welded-jointed lattice.

Chapter 5 will discuss the two most important findings of the study. These will be related to the macroscopic Young's modulus and Poisson's ratio.

Finally, a conclusion will be drawn from the information gathered in all the previous chapters in chapter 6. This will also include future work.

Supplementary information and figures will be listed in the Appendix, this includes the analysis of another lattice micro-architecture.

2. Linear analysis

In this chapter the pin-jointed Kagome truss will be studied. The matrix method will be applied in this chapter on this lattice architecture, to find out if the equivalent truss structure has a collapse mechanism. This method will in the remainder be referred to as the linear analysis as the analysis of the truss is only done using its initial configuration. This linear analysis will result in a collapse mechanism provided by the nullspace of the kinematic matrix. Conveniently, a collapse mechanism for the Kagome truss is already described in section 1.2.1. This mechanism will be used to confirm the result found in this chapter. Important to keep in mind is that the result of the linear analysis does not indicate whether or not the mechanism is finite or infinitesimal. Definite proof to show that it indeed is a finite mechanism will be provided in this chapter.

2.1 Matrix method

The mechanical properties of welded-jointed lattice materials are closely related to the static and kinematic properties of their pin-jointed counterpart. Therefore infinite lattice materials can be analysed by using the matrix method described by Pelligrino and Calladine (1986)[14]. This method has proven to be a useful tool in the quest for lattice architectures suitable for actuation, since it is key for identifying stretching-dominated lattice materials with high stiffness (Pronk *et al.* (2017) [15], Nelisson *et al.* (2018) [12]).

2.1.1 Equilibrium and kinematic equations

Equilibrium equations can be set up for a n-dimensional pin-jointed structure, where b is the number of bars and j the number of joints in an unit cell. The (n j × b) equilibrium matrix $\boldsymbol{A}$ relates the (b × 1) tension in the bars $\boldsymbol{t}$ with the (n j × 1) forces acting upon the joints $\boldsymbol{f}$ of the unit cell as

$$\boldsymbol{At} = \boldsymbol{f}. \tag{2.1}$$

The nullspace of the $\boldsymbol{A}$ matrix, or $\boldsymbol{N}(\boldsymbol{A})$, contains all linearly independent non-trivial solutions that satisfy $\boldsymbol{At} = \boldsymbol{0}$. These solutions are also known as the states of self-stress, that is all combinations of bar tensions that are in equilibrium with zero nodal loads, and only appear when the $\boldsymbol{A}$ matrix is rank deficient. The given states of self-stress are the linearly independent solutions of the nullspace analysis, linear combinations of these solutions can also be considered solutions for this analysis.

The (b × n j) compatibility matrix $\boldsymbol{B}$ relates the (n j × 1) nodal displacements $\boldsymbol{d}$ with the (b × 1) bar elongations $\boldsymbol{e}$ as

$$\boldsymbol{Bd} = \boldsymbol{e}. \tag{2.2}$$

The nullspace of matrix $\boldsymbol{B}$, or $\boldsymbol{N}(\boldsymbol{B})$, contains the linearly independent non-trivial solutions that satisfy $\boldsymbol{Bd} = \boldsymbol{0}$, also known as the inextensional displacement modes. Such displacements for the infinite truss must either be a rigid-body translation or a collapse mechanism, a rigid-body rotation would violate the periodicity constraint of an infinite truss. Again, a linear combination of the linearly independent solutions can be considered a solution.

It can be shown with the principle of virtual work [3] that the equilibrium matrix and the compatibility matrix are related by the general relationship:

$$\boldsymbol{B} = \boldsymbol{A}^{\boldsymbol{T}}. \tag{2.3}$$

Consequently, the rank of the equilibrium matrix $\boldsymbol{A}$ and the compatibility matrix $\boldsymbol{B}$ are the same. This also implies that the nullspaces of both matrices are connected.

2.1.2 Collapse mechanisms

The collapse mechanisms of pin-jointed trusses identified by the kinematic matrix can be classified into two categories, namely infinitesimal and finite mechanisms. For a finite mechanism the joints can freely move and the bars can rotate around the joints for a finite amount with absolutely no change in the bar lengths. For an infinitesimal mechanism, however, there will be some small changes in the lengths of the bars when the joints actually move. These changes may be of second or higher order terms in terms of joint displacements. The infinitesimal mechanisms 'tighten up' when mobilised, therefore locking the system and preventing movement [14].

The matrix method can only detect the absence of first-order changes in the lengths of the bars. As a consequence is unable to distinguish between finite and infinitesimal mechanisms, whether a mechanism is finite or not is thus determined by initiating the mechanism and monitoring the response of the repetitive pin-jointed truss [14].

Collapse mechanisms can be further divided into strain-producing mechanisms and non strain-producing mechanisms, that is whether or not the mechanism can be excited by a macroscopic load case. Pin-jointed truss structures that contain one or more strain-producing mechanisms imply the equivalent rigidly jointed lattice material to be bending-dominated. The mechanism can be excited with the use of a macroscopic load. Pin-jointed truss structures that only possess non strain-producing mechanisms or have no mechanism at all imply the equivalent rigidly-jointed lattice material to be stretching-dominated. The described mechanism can therefore not be excited by a macroscopic load. Lattices that are stretching-dominated have a much stiffer macroscopic response than their bending-dominated counterparts, due to the bending stiffness of slender beams being much lower than their axial stiffness.

2.1.3 Augmented kinematic analysis

Determining if a mechanism is strain-producing is done by calculating the nullspace of an augmented compatibility matrix. This augmented compatibility matrix shows, in addition to the normal joint displacements, the deformation of the unit cell by augmenting the allowed displacements [7]. This is achieved by including the displacements of nodes in adjacent unit cells connected to bars that cross the unit cell boundary. If the mechanism is non strain-producing then the last three rows of the nullspace of $\boldsymbol{B}_{\text{aug}}$ will only contain zeros, indicating no deformation to the unit cell. A strain-producing mechanism will yield at least one non-zero entry in the last three rows, indicating a deformation to the unit cell.

A few additions must be made to the standard kinematic analysis. It can be immediately noted that the elongation vector $\boldsymbol{e}$ does not need any augmentation, only the compatibility matrix $\boldsymbol{B}$ and the deformation vector $\boldsymbol{d}$ need modifications. Starting with the deformation vector, three extra terms will need to be included on top of the joint displacements $d_i^{(j)}$, where i and j denote the displacement in the x_i-direction of node j. These three extra terms contain information on the unit cell deformation, resulting in the following vector:

$$\boldsymbol{d}_{\text{aug}} = [d_1^{(1)} \quad d_2^{(1)} \quad ... \quad d_1^{(j)} \quad d_2^{(j)} \quad d_{11} \quad d_{12} \quad d_{22}]^T. \tag{2.4}$$

To augment the compatibility matrix a few extra nodes need to be defined outside of the unit cell, e.g. see figure 2.2(b). These extra nodes are connected to bars that cross unit cell boundaries, only half of all these bars need to be connected to extra nodes, due to the periodicity constraint. These extra nodes can be linked to existing nodes inside the unit cell due to the same constraint. Matrix $\boldsymbol{C}$ (b $\times$ 3) is made by carefully evaluating the bars that cross the periodic boundary. Appending the columns of matrix $\boldsymbol{C}$ with the columns of matrix $\boldsymbol{B}$ results in the augmented compatibility matrix $\boldsymbol{B}_{\text{aug}}$.

$$\boldsymbol{B}_{\text{aug}} = [\boldsymbol{B}|\boldsymbol{C}] \tag{2.5}$$

If a structure only contains non strain-producing mechanisms then removing the last three rows from the $\boldsymbol{N}(\boldsymbol{B}_{\text{aug}})$ will yield the same answer as $\boldsymbol{N}(\boldsymbol{B})$. However, it should be noted that if a structure does contain a strain-producing mechanism removing the last three rows of $\boldsymbol{N}(\boldsymbol{B}_{\text{aug}})$ will not yield the same answer as $\boldsymbol{N}(\boldsymbol{B})$. It is possible for mechanisms to show up in the nullspace of the augmented compatibility matrix that did not get identified by the normal analysis of the compatibility matrix. As previously mentioned, the results of $\boldsymbol{N}(\boldsymbol{B}_{\text{aug}})$ also have implications for $\boldsymbol{N}(\boldsymbol{A})$, see equation 2.3. If the mechanism is indicated to be strain-producing by $\boldsymbol{N}(\boldsymbol{B}_{\text{aug}})$ then no combination of the states of self-stress found by $\boldsymbol{N}(\boldsymbol{A})$ will be able to support all macroscopic loads. Likewise, if the mechanism is shown to be non strain-producing then a combination of the found states of self-stress will be able to support all macroscopic loads.

2.2 Analysis of the Kagome configuration

The first step is to define the unit cell that will be used for the linear analysis. Figure 2.1 shows the unit cell used, where the joints are indicated by Arabic numbers and the beams are indicated by Roman numerals. All bar lengths are of equal length l_0. Nodes 2, 3, 4 and 5 lie on the boundary of the unit cell. Tessellating the unit cell as is done in figure 2.2(a) shows that node 2 and node 5 overlap. They should be considered as the same node and therefore node 5 can be seen as a repeat of node 2, or 2 is the master node and 5 is the slave node. The same applies to nodes 3 and 4. This this is a direct consequence of the unit cell being doubly periodic, this is in 2D a requirement for a unit cell to be tessellatable. Consequently, the bars that are connected to node 4 and node 5 are linked to the deformation of the unit cell. The motion of these slave nodes during collapse will not be the same as the master nodes, these nodes will also experience the effects of the unit cell deformation. A slightly altered unit cell formulation as seen in figure 2.2(b) clearly shows that bars IV, V and VI cross the unit cell boundaries and therefore are affected by unit cell deformations. The unit cells shown in figures 2.1 and 2.2(b) are equivalent, it is up to the users preference which one is used.

The displacement vector $\boldsymbol{d}$ (6×1) only contains the information of the three master nodes, $\boldsymbol{d} = [d_1^{(1)} d_2^{(1)} d_1^{(2)} d_2^{(2)} d_1^{(3)} d_2^{(3)}]^T$, where $d_i^{(\text{j})}$ denotes the displacement in the x_i-direction of node j. The elongation vector will be a zero vector, for all analyses in this research, as only solutions that do not involve bar elongation are of interest. This is in order to find collapse mechanisms that do not require variations in the bar lengths in order to achieve collapse.

The compatibility matrix $\boldsymbol{B}$ (6×6) can be set up for this unit cell with the use of the truss geometry.

$$
\begin{aligned}
e_{\text{I}} &= d_1^{(2)} - d_1^{(3)}, \\
e_{\text{II}} &= -\frac{1}{2} d_1^{(1)} - \frac{\sqrt{3}}{2} d_2^{(1)} + \frac{1}{2} d_1^{(2)} + \frac{\sqrt{3}}{2} d_2^{(2)}, \\
e_{\text{III}} &= \frac{1}{2} d_1^{(1)} - \frac{\sqrt{3}}{2} d_2^{(1)} - \frac{1}{2} d_1^{(3)} + \frac{\sqrt{3}}{2} d_2^{(3)}, \\
e_{\text{IV}} &= -\frac{1}{2} d_1^{(1)} + \frac{\sqrt{3}}{2} d_2^{(1)} + \frac{1}{2} d_1^{(4)} - \frac{\sqrt{3}}{2} d_2^{(4)} = -\frac{1}{2} d_1^{(1)} + \frac{\sqrt{3}}{2} d_2^{(1)} + \frac{1}{2} d_1^{(3)} - \frac{\sqrt{3}}{2} d_2^{(3)}, \\
e_{\text{V}} &= \frac{1}{2} d_1^{(1)} + \frac{\sqrt{3}}{2} d_2^{(1)} - \frac{1}{2} d_1^{(5)} - \frac{\sqrt{3}}{2} d_2^{(5)} = \frac{1}{2} d_1^{(1)} + \frac{\sqrt{3}}{2} d_2^{(1)} - \frac{1}{2} d_1^{(2)} - \frac{\sqrt{3}}{2} d_2^{(2)}, \\
e_{\text{VI}} &= d_1^{(4)} - d_1^{(5)} = d_1^{(3)} - d_1^{(2)}.
\end{aligned}
\tag{2.6}
$$

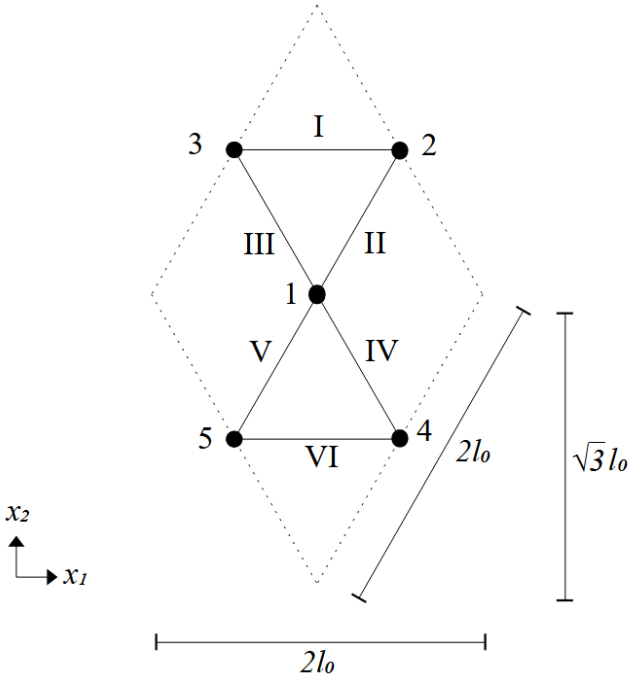

Figure 2.1: The Kagome unit cell used for the linear matrix analysis. Node numbers are indicated with Arabic numbers and bar numbers are indicated with Roman numerals.

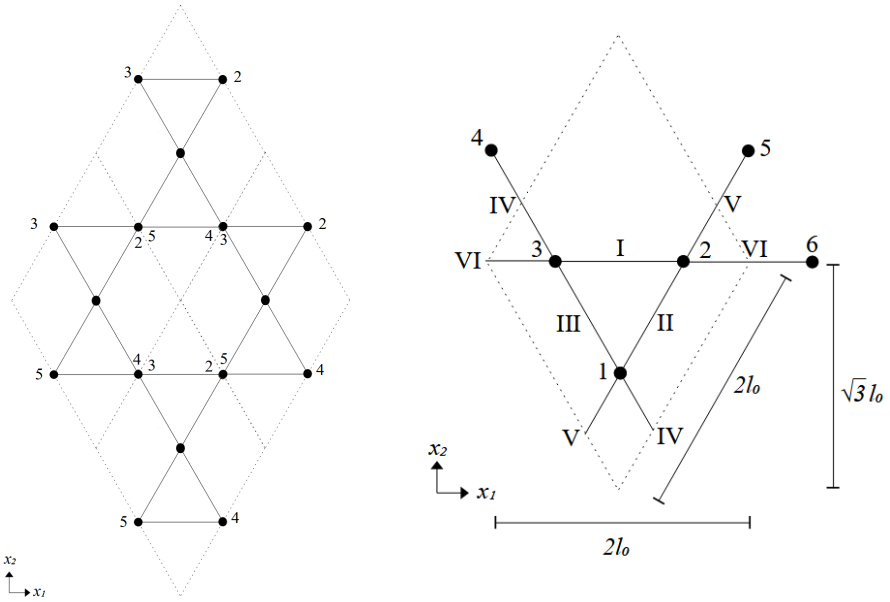

(a) (b)

Figure 2.2: (a) A tessellated version of figure 2.1. Node 2 and 5 overlap when the small unit cell is tessellated therefore they should be considered to be the same node. The same reasoning can be applied to node 3 and 4. (b) An alternative unit cell for the Kagome truss. This unit cell allows the bars to cross the boundary of the unit cell instead of placing the nodes onto the boundary of the unit cell.

The kinematic relation set up in equation 2.6 can be rewritten in matrix form by remembering $\boldsymbol{Bd} = \boldsymbol{e}$.

$$\boldsymbol{B} = \begin{bmatrix} 0 & 0 & 1 & 0 & -1 & 0 \\ -\frac{1}{2} & -\frac{\sqrt{3}}{2} & \frac{1}{2} & \frac{\sqrt{3}}{2} & 0 & 0 \\ \frac{1}{2} & -\frac{\sqrt{3}}{2} & 0 & 0 & -\frac{1}{2} & \frac{\sqrt{3}}{2} \\ -\frac{1}{2} & \frac{\sqrt{3}}{2} & 0 & 0 & \frac{1}{2} & -\frac{\sqrt{3}}{2} \\ \frac{1}{2} & \frac{\sqrt{3}}{2} & -\frac{1}{2} & -\frac{\sqrt{3}}{2} & 0 & 0 \\ 0 & 0 & -1 & 0 & 1 & 0 \end{bmatrix} \tag{2.7}$$

The standard kinematic analysis can now be performed. However, the standard analysis cannot find strain-producing mechanisms, that is collapse mechanisms that require the unit cell itself to deform in order to collapse. Therefore the information about the unit cell deformation needs to be included in the compatibility matrix. Firstly, the displacement vector is augmented by adding three new terms, related to the change in the unit cell size. These terms are defined as:

$$\begin{aligned} d_{11} &= 2l_0\varepsilon_{11}, \\ d_{12} &= 2l_0\varepsilon_{12}, \\ d_{22} &= \sqrt{3}l_0\varepsilon_{22}, \end{aligned} \tag{2.8}$$

which are the three planar strains ε_{ij} multiplied with the characteristic unit cell lengths as shown in figure 2.1. Adding these terms to the displacement vector $\boldsymbol{d}$ results in the augmented displacement vector (9×1):

$$\boldsymbol{d}_{\text{aug}} = [d_1^{(1)} \quad d_2^{(1)} \quad d_1^{(2)} \quad d_2^{(2)} \quad d_1^{(3)} \quad d_2^{(3)} \quad d_{11} \quad d_{12} \quad d_{22}]^T. \tag{2.9}$$

Secondly, the kinematic relations need to be augmented, this is achieved by describing the strains in terms of nodal displacements of periodic nodes.

$$\begin{aligned} d_1^{(4)} - d_1^{(3)} &= l_0\varepsilon_{\alpha 1} - \sqrt{3}l_0\varepsilon_{\alpha 2}, \\ d_1^{(5)} - d_1^{(2)} &= -l_0\varepsilon_{\alpha 1} - \sqrt{3}l_0\varepsilon_{\alpha 2}, \end{aligned} \tag{2.10}$$

where $\alpha = 1 \ldots 2$ in 2D analysis. This can be rewritten as:

$$\begin{aligned} d_1^{(4)} &= d_1^{(3)} + \frac{1}{2}d_{11} - \frac{\sqrt{3}}{2}d_{12}, & d_2^{(4)} &= d_2^{(3)} + \frac{1}{2}d_{12} - d_{22}, \\ d_1^{(5)} &= d_1^{(2)} - \frac{1}{2}d_{11} - \frac{\sqrt{3}}{2}d_{12}, & d_2^{(5)} &= d_2^{(2)} - \frac{1}{2}d_{12} - d_{22}. \end{aligned} \tag{2.11}$$

The augmented compatibility matrix can be constructed, now that slave nodes are related to the master nodes in terms of the strain endured by the unit cell. Similar to equation 2.2, the new augmented compatibility matrix relates the augmented displacement vector to the elongation of the bars, now including the information of the unit cell deformation.

$$\boldsymbol{B}_{\text{aug}}\boldsymbol{d}_{\text{aug}} = \boldsymbol{e} \tag{2.12}$$

Augmenting the relevant bar elongations from equation 2.6:

$$\begin{aligned}
e_{\text{IV}} &= -\frac{1}{2}d_1^{(1)} + \frac{\sqrt{3}}{2}d_2^{(1)} + \frac{1}{2}d_1^{(4)} - \frac{\sqrt{3}}{2}d_2^{(4)} = -\frac{1}{2}d_1^{(1)} + \frac{\sqrt{3}}{2}d_2^{(1)} + \frac{1}{2}d_1^{(3)} - \frac{\sqrt{3}}{2}d_2^{(3)} + \frac{1}{4}d_{11} - \frac{\sqrt{3}}{2}d_{12} + \frac{\sqrt{3}}{2}d_{22}, \\
e_{\text{V}} &= \frac{1}{2}d_1^{(1)} + \frac{\sqrt{3}}{2}d_2^{(1)} - \frac{1}{2}d_1^{(5)} - \frac{\sqrt{3}}{2}d_2^{(5)} = \frac{1}{2}d_1^{(1)} + \frac{\sqrt{3}}{2}d_2^{(1)} - \frac{1}{2}d_1^{(2)} - \frac{\sqrt{3}}{2}d_2^{(2)} + \frac{1}{4}d_{11} + \frac{\sqrt{3}}{2}d_{12} + \frac{\sqrt{3}}{2}d_{22}, \\
e_{\text{VI}} &= d_1^{(4)} - d_1^{(5)} = d_1^{(3)} - d_1^{(2)} + d_{11}.
\end{aligned} \tag{2.13}$$

For the undeformed configuration the augmented matrix $\boldsymbol{B}_{\text{aug}}$ of the Kagome truss is the following:

$$\boldsymbol{B}_{\text{aug}} = \begin{bmatrix}
0 & 0 & 1 & 0 & -1 & 0 & 0 & 0 & 0 \\
-\frac{1}{2} & -\frac{\sqrt{3}}{2} & \frac{1}{2} & \frac{\sqrt{3}}{2} & 0 & 0 & 0 & 0 & 0 \\
\frac{1}{2} & -\frac{\sqrt{3}}{2} & 0 & 0 & -\frac{1}{2} & \frac{\sqrt{3}}{2} & 0 & 0 & 0 \\
-\frac{1}{2} & \frac{\sqrt{3}}{2} & 0 & 0 & \frac{1}{2} & -\frac{\sqrt{3}}{2} & \frac{1}{4} & -\frac{\sqrt{3}}{2} & \frac{\sqrt{3}}{2} \\
\frac{1}{2} & \frac{\sqrt{3}}{2} & -\frac{1}{2} & -\frac{\sqrt{3}}{2} & 0 & 0 & \frac{1}{4} & \frac{\sqrt{3}}{2} & \frac{\sqrt{3}}{2} \\
0 & 0 & -1 & 0 & 1 & 0 & 1 & 0 & 0
\end{bmatrix}. \tag{2.14}$$

Comparing matrix 2.7 and 2.14 clearly confirms that the kinematic matrix $\boldsymbol{B}$ is a submatrix of the augmented kinematic matrix $\boldsymbol{B}_{\text{aug}}$. Both matrices are rank deficient by 3, meaning that 3 linearly independent displacement modes are found in the nullspace given as

$$\boldsymbol{N}(\boldsymbol{B}_{\text{aug}}) = \begin{bmatrix}
0 & 1 & 0 & 1 & 0 & 1 & 0 & 0 & 0 \\
1 & 0 & 1 & 0 & 1 & 0 & 0 & 0 & 0 \\
\sqrt{3} & 0 & 0 & 1 & 0 & -1 & 0 & 0 & 0
\end{bmatrix}^T. \tag{2.15}$$

The first two columns of $\boldsymbol{N}(\boldsymbol{B}_{\text{aug}})$ are rigid body translations in the x_2- and x_1-direction. The third column represents the linearised version of a possibly finite mechanism. This mechanism is non strain-producing, it has yet to be determined if the mechanism is finite or infinitesimal. The last three rows only contain zero entries i.e. no unit cell deformation is associated with any of the macroscopic strain inducing deformation modes. Therefore none of these displacement modes are strain-producing. Interestingly, all three displacement modes can be found by only analysing the normal compatibility matrix $\boldsymbol{N}(\boldsymbol{B})$ due to the fact that none of them are strain-producing. This could also be deduced by comparing the rank deficiency of both matrices. If a strain-producing mechanism is present then the rank deficiency of the augmented matrix should be higher than that of the non augmented matrix. It is not possible for the non augmented matrix to have a higher rank deficiency than the augmented matrix, as the non

strain-producing mechanisms will always show up in the nullspace of the augmented matrix.

An artist's impression of an increment of the mechanism described by the third row in equation 2.15 is depicted in figure 2.3. This motion seems to be in agreement with the mechanism described in section 1.2.1. The motion can be characterised as two connected triangles rotating with an equal but opposite angle around the same node.

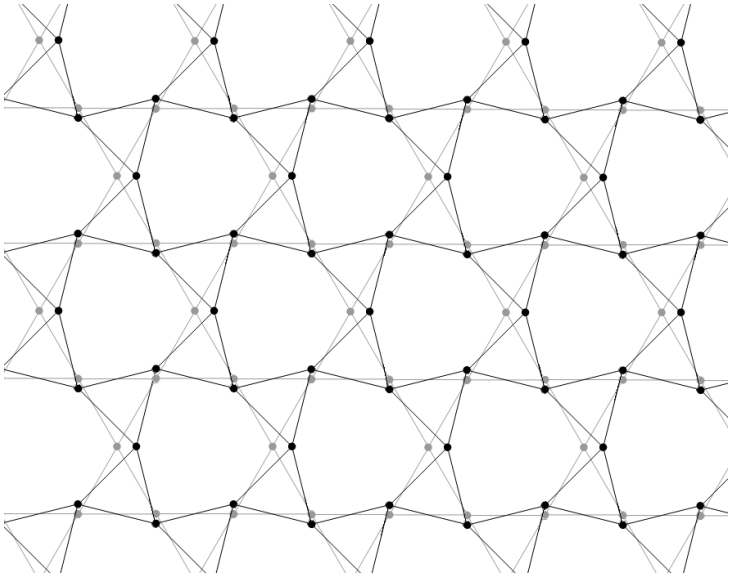

Figure 2.3: Linearised representation of the mechanism of the Kagome truss based on the mechanism found in equation 2.15. The gray structure is the undeformed starting position, while the black structure represents the deformed state after the mechanism is excited. Movement of the triangles is exaggerated to better show the movement of the structure.

2.3 Finite mechanism

The matrix method as described by Pellegrino and Calladine [14] can only detect finite and second- or higher-order infinitesimal mechanisms and is unable to distinguish between the two. The description of a collapse motion that preserves the bar lengths will be enough to prove the presence of the finite version of the mechanism. If this condition is violated then the mechanisms must be infinitesimal.

2.3.1 Characterising the motion

The mechanism in equation 2.15 implies that the slave nodes must exactly follow their respective master nodes, for the first deformation step, as the unit cell deformation is equal to zero. The motion in the unit cell therefore must have a symmetry line on $x_2^{(1)} = 0$. Extrapolating the motion of the unit cell results in nodes 2, 3, 4 and 5 rotating around node 1. Keeping the same angle ω as denoted in figure 1.2, the rotation can be described as:

$$\begin{aligned}
x_1^{(2)} &= x_1^{(1)} - l_0\cos(\omega + \frac{\pi}{3}), & x_2^{(2)} &= x_2^{(1)} + l_0\sin(\omega + \frac{\pi}{3}),\\
x_1^{(3)} &= x_1^{(1)} - l_0\cos(\omega), & x_2^{(3)} &= x_2^{(1)} + l_0\sin(\omega),\\
x_1^{(4)} &= x_1^{(1)} - l_0\cos(\omega + \frac{\pi}{3}), & x_2^{(4)} &= x_2^{(1)} - l_0\sin(\omega + \frac{\pi}{3}),\\
x_1^{(5)} &= x_1^{(1)} - l_0\cos(\omega), & x_2^{(5)} &= x_2^{(1)} - l_0\sin(\omega),
\end{aligned} \tag{2.16}$$

where l_0 denotes the starting length of the bar.

Figure 2.4(a) shows the rotation of the nodes around node 1, where angle $\omega = 7\pi/30$ is used to illustrate the rotation. However, the center of the new unit cell does not line up with the center of the old unit cell. A translation of the whole structure in x_1-direction is done to more clearly show the decrease in the unit cell dimensions in figure 2.4(b).

The completed motion for angle $\omega = 7\pi/30$ can be seen in figure 2.4(b). The complete collapse based on equation 2.16 is shown in figure 2.5 with six steps. The center of the unit cell has been fixated to the origin. Clearly, rotation and translation of triangles will not change the bar lenghts.

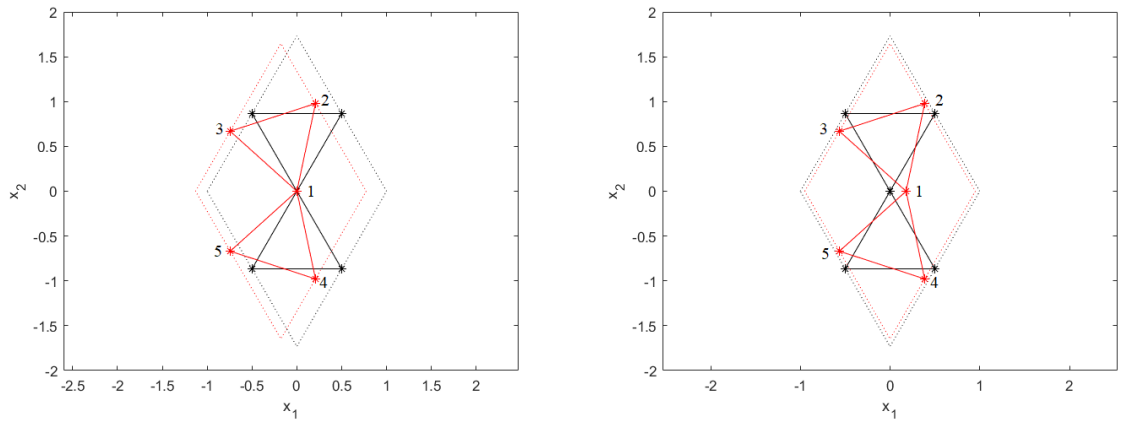

(a) Rotation (b) Translation

Figure 2.4: (a) The rotation of node 2, 3, 4, and 5 around node 1, $\omega = 7\pi/30$. The undeformed structure is given in black with a black dotted line to denote the unit cell. The red structure is the partly rotated configuration, with a red dotted unit cell outline. (b) The translation of the deformed structure so that the centers of the old and the new unit coincide.

The area of the unit cell can be calculated as:

$$A_c = ((x_1^{(2)} - x_1^{(5)})^2 + (x_2^{(2)} - x_2^{(5)})^2) \sin(\frac{\pi}{3}) \tag{2.17}$$

This area shrinks when the mechanism is induced as can be seen in figure 2.6. This decrease in area between the Kagome, T-T and fully triangular configuration is also in agreement with Hutchinson and Fleck [9], see section 1.2.1.

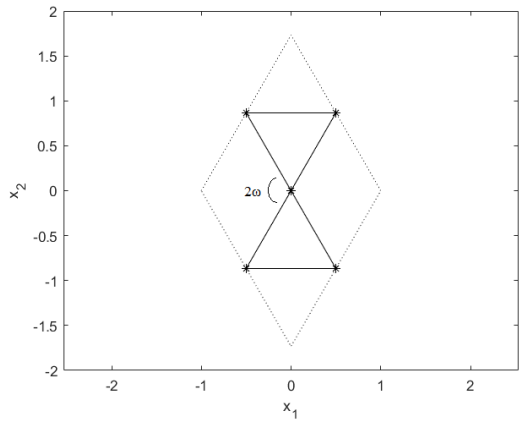

(a) $\omega = \dfrac{\pi}{3}$

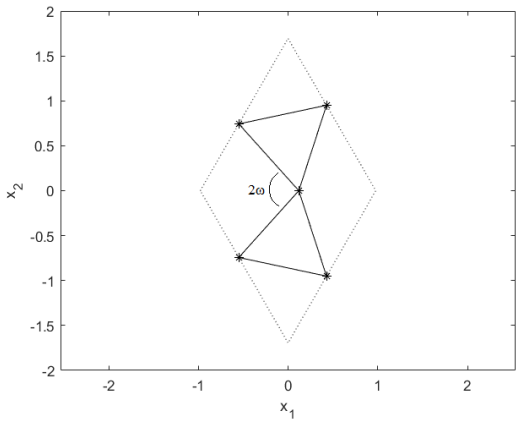

(b) $\omega = \dfrac{4\pi}{15}$

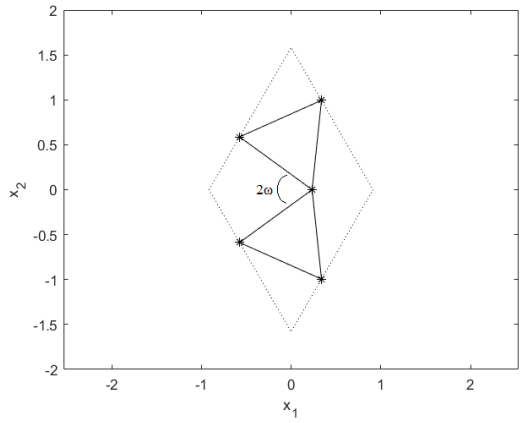

(c) $\omega = \dfrac{\pi}{5}$

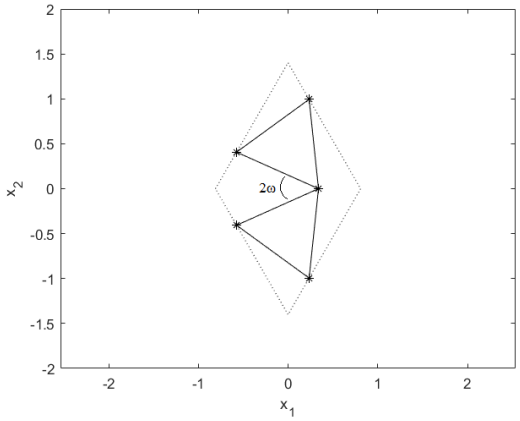

(d) $\omega = \dfrac{2\pi}{15}$

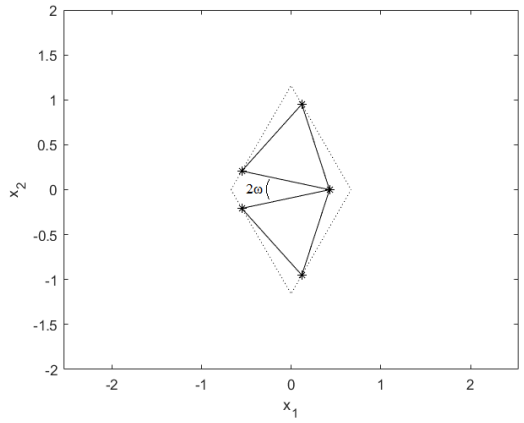

(e) $\omega = \dfrac{\pi}{15}$

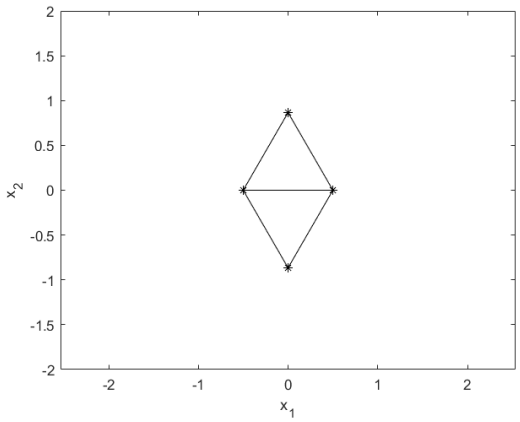

(f) $\omega = 0$

Figure 2.5: The collapse motion of the Kagome truss captured in 6 steps. Subfigure (a) is the starting point and therefore the undeformed configuration. Subfigures (b), (c), (d) and (e) show the intermediate steps before reaching the full collapse as shown in subfigure (f). The center of the unit cell is always located at the origin.

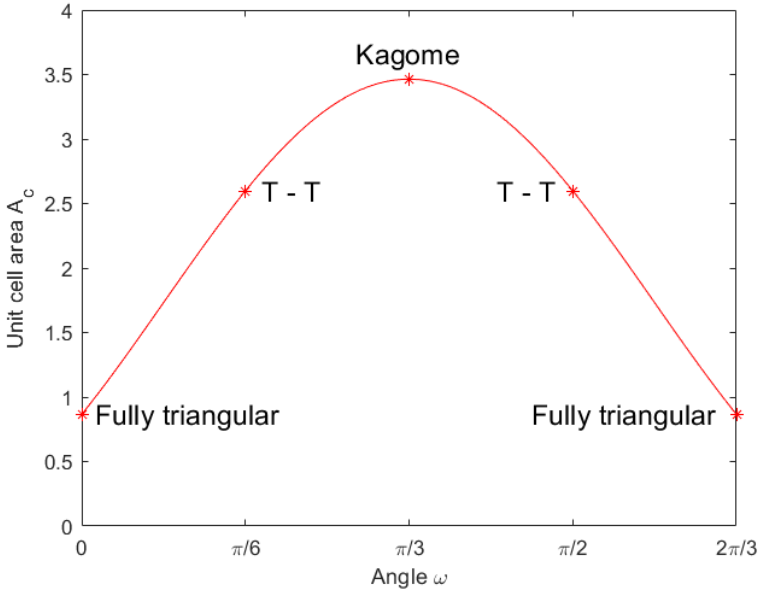

Figure 2.6: The area decrease caused by inducing the collapse mechanism. The highest area value is associated with the Kagome configuration. Collapsing the structure clockwise or counterclockwise does not influence the rate the area decreases.

2.4 Tessellation of the space

The periodicity of the unit cell must be preserved at any stage of collapse, in order to study infinite pin-jointed trusses, describing a finite collapse motion does not automatically satisfy this condition. Therefore the unit cell must be tessellatable at any configuration, if this is not the case then the results found by the matrix method will not be applicable to the whole truss. Master and slave nodes must overlap when two unit cell boundaries are aligned at any step of the motion in order for the cell to remain tessellatable. It will be proven that this is indeed the case for the Kagome truss.

The rhombus forming the unit cell will be chosen in such a way that the internal angles of the rhombus itself will be preserved. It can be split into two equilateral triangles at the symmetry line, as denoted by a dotted line in figure 2.7. The top triangle formed by the unit cell encapsulates the triangle formed by nodes 1, 2 and 3, as the unit cell has been formulated in such a way that the joints will always fall on the edges of the triangle, since the size of the unit cell depends on angle ω. This top triangle will be denoted as $\triangle$ ABC, note that points A, B, B$'$ and C are not joints from the Kagome truss, but simply points of interest of the unit cell. The unit cell if denoted with a dashed line. Both triangle $\triangle$ ABC and $\triangle$ DEF are equilateral triangles but the sides are not of equal length, making them similar triangles, $\triangle$ ABC $\sim$ $\triangle$ DEF. Three smaller triangles are formed due to this configuration. All angles in the three triangles can be calculated since the sum of interior angles of any triangle is π and similarly, a straight angle is also equal to π.

$$
\begin{array}{llll}
\triangle ADF & \angle DAF = \frac{\pi}{3} & \angle AFD = \omega & \angle ADF = \pi - \angle DAF - \angle AFD = \frac{2\pi}{3} - \omega, \\
\triangle BDE & \angle DBE = \frac{\pi}{3} & \angle BDE = \pi - \angle FDE - \angle ADF = \omega & \angle BED = \pi - \angle DBE - \angle BDE = \frac{2\pi}{3} - \omega, \\
\triangle CEF & \angle ECF = \frac{\pi}{3} & \angle CEF = \pi - \angle DEF - \angle BED = \omega & \angle CFE = \pi - \angle DFE - \angle AFD = \frac{2\pi}{3} - \omega.
\end{array}
$$

It can be proven in several ways that triangles are congruent. In this case ASA will be used, or angle-side-angle, meaning that if two angles are congruent and their included side is congruent with the other triangle then the pair of triangles must be congruent. It can be concluded that the three smaller triangles are congruent given the fact that lengths DE, EF and FD are equal and all angles attached to the sides are

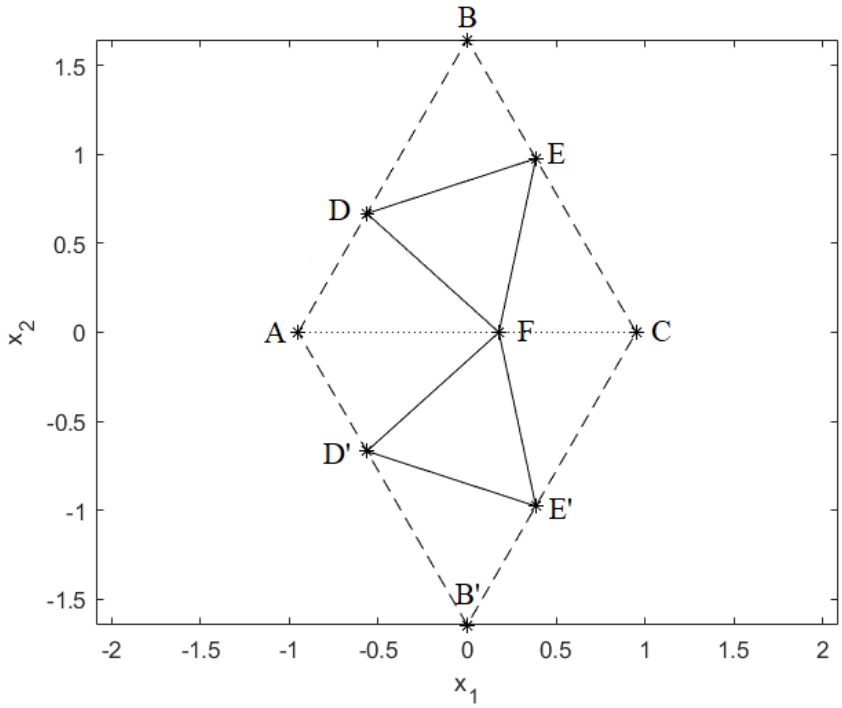

Figure 2.7: The Kagome unit cell divided into two symmetric triangles, each encapsulating 4 smaller triangles. The line of symmetry is located at $x_2 = 0$, denoted by a dotted line. The unit cell is denoted by a dashed line.

equal. This also implies that lengths AD, BE and CF are equal, similar lengths AF, BD and CE are equal.

The same relations can be found for the bottom triangle $\triangle$ AB′C, as it is the mirrored version of triangle $\triangle$ ABC. The equality's of the lengths can now be expanded into:

$$
\begin{aligned}
AB = BC = AC = AB' = B'C,\\
DE = EF = FD = E'F = FD',\\
AD = BE = CF = AD' = B'E',\\
AF = BD = CE = B'D' = CE'.
\end{aligned}
$$

Lastly, it must be shown that master and slave nodes align in order for the unit cell to properly 'fit'. This is done by aligning a second unit cell with the first unit cell, in this case side AB of the first unit cell will be aligned with side B′C of the second unit cell. It is known that sides AB and B′C are of equal length. The master node of the Kagome truss of the first unit cell, here denoted as D, is located on the line AB at a distance of AD seen from point A. The slave node of the second unit cell, denoted E′, is located on the line B′C at a distance of B′E′ as seen from B′. It can be concluded that joints D and E′ overlap due to the fact that it has been shown that distance AD is equal to distance B′E′. The same steps can be taken to show that nodes D′ and E also align. These relations are applicable for any angle ω, making the structure tessellatable at any configuration, see figure 2.8.

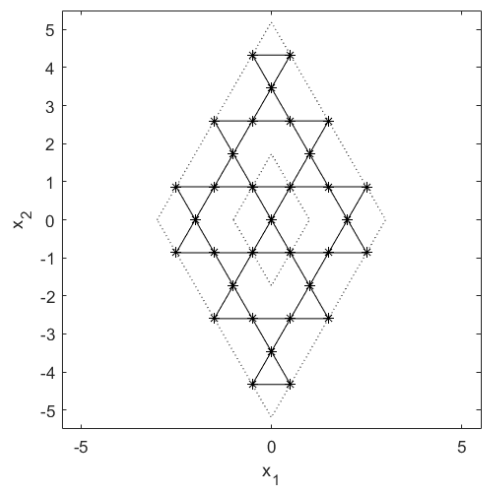

(a) $\omega = \frac{\pi}{3}$

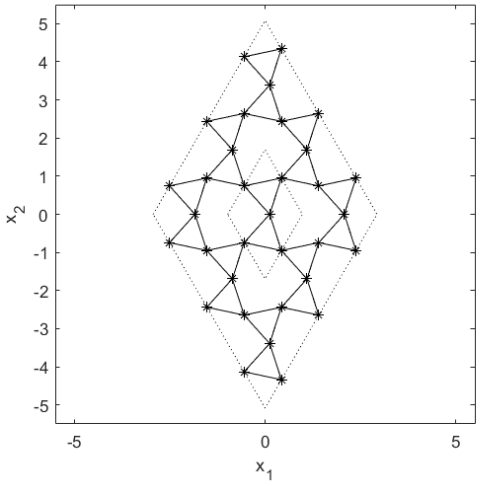

(b) $\omega = \frac{4\pi}{15}$

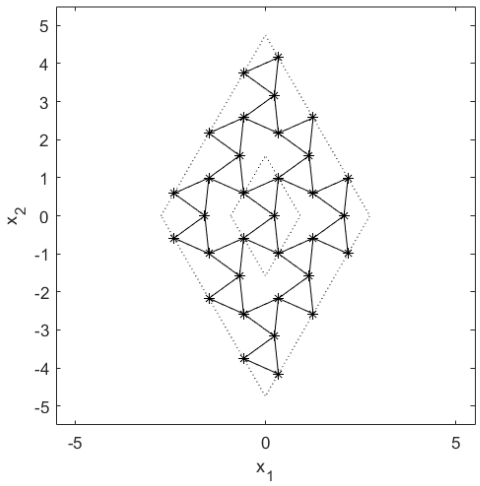

(c) $\omega = \frac{\pi}{5}$

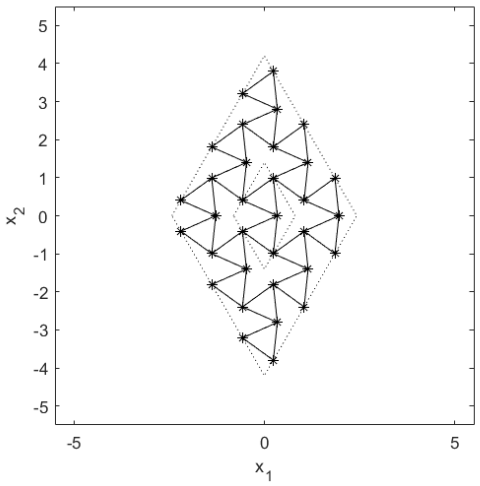

(d) $\omega = \frac{2\pi}{15}$

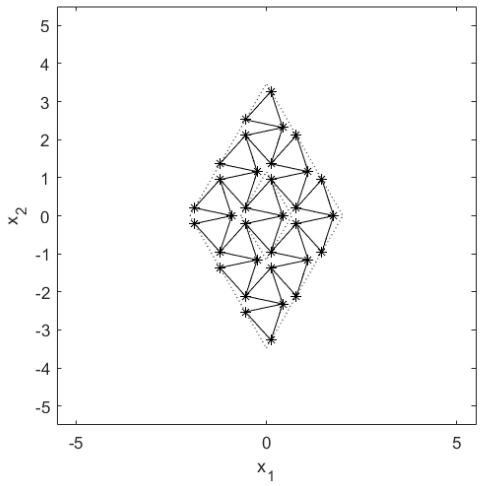

(e) $\omega = \frac{\pi}{15}$

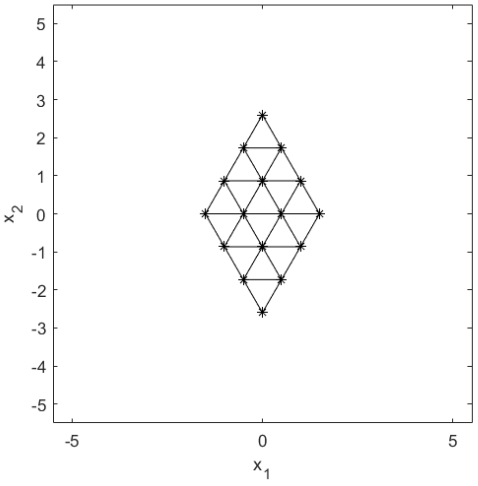

(f) $\omega = 0$

Figure 2.8: The collapse motion of a tessellated Kagome truss captured in 6 steps. Subfigure (a) is the starting point and therefore the undeformed configuration. Subfigures (b), (c), (d) and (e) show the intermediate steps before reaching the full collapse as shown in subfigure (f).

2.5 Discussion

The mechanism found in equation 2.15 can be concluded to be finite, now that the full motion has been characterised. And the results of the matrix method are applicable for the whole truss as it has been shown that the periodicity has been preserved for any value of ω.

Clearly, the unit cell area has shrunk during deformation, the ratio between the characteristic unit cell dimensions is preserved during deformation, while the area of the unit cell is not. The largest unit cell area decreases from the Kagome configuration to the smallest area at the fully triangular state, see the graph in figure 2.6. The folding direction of the structure does not change the rate of area decrease. This also implies that the relative density is smallest for the Kagome configuration and increases when during the collapse.

The Kagome truss and the fully triangular configuration both have a sixfold symmetry and thus the rigidly-jointed lattice are elastically isotropic. All rigidly-jointed intermediate configurations have a threefold symmetry and the rigid-jointed equivalents are thus also elastically isotropic [2]. This property is not evident when evaluating the small unit cells as seen in figure 2.5. This property can be seen much more clearly in figure 2.8. Two independent lines of symmetry are given by extending the lines of the unit cell itself, these unit cell boundaries naturally form these symmetry lines. The last independent line of symmetry is found by extending the symmetry line found within the unit cell, this symmetry remains intact for any value of ω. Therefore three independent lines of symmetry can be found at any intermediate configuration.

3. Nonlinear analysis

This chapter will continue with the mechanism found in the previous chapter. As was established in the previous chapter, the mechanism found by the linear analysis is finite. Therefore this mechanism can be translated into a motion. Hutchinson and Fleck (2006) [9] noticed that a relation exists between the pin-jointed Kagome truss, the triangular-triangular truss and the fully triangular truss. They are connected by the finite collapse described in the previous chapter, but at the same time the number and types of mechanisms are different for all structures. While the Kagome truss only has non strain-producing mechanisms, the triangular-triangular truss has one strain-producing mechanism and the fully triangular structure has no collapse mechanisms at all. This raises the questions: 'At what configuration does the pin-jointed truss lose its non strain-producing mechanism?', 'Does it regain this non strain-producing mechanism at any other configuration?' and 'When is the mechanism completely lost?'.

The mechanism will be excited in a pin-jointed truss in order to answer the above questions, as this will be able to determine the elastic response of the equivalent welded-jointed lattice is stretching- or bending-dominated. The unit cell illustrated in figure 3.1 will now be used to indicate the relations between the initial configuration and the rotated configurations. The same node numbering and bar numbering will be used as mentioned in figure 2.1. Angle θ will be used to relate the initial configuration to the rotated configuration, $\omega = \pi/3 - \theta$. This angle was chosen as it indicates how far away the rotated structure is from the initial configuration, that is the higher θ the further away the current configuration is from the initial configuration. Three cases will be investigated, namely:

$$\theta = 0, -\frac{\pi}{3} < \theta < 0 \cup 0 < \theta < \frac{\pi}{3}, \theta = -\frac{\pi}{3} \cup \frac{\pi}{3}, \tag{3.1}$$

or the initial configuration, the intermediate steps and the full collapse.

3.1 Setting up the nonlinear analysis

The full collapse motion used for this analysis inside a single unit cell can be described by two triangles rotating with respect to each other while being fixated at one corner of the triangles. The two triangles in the unit cell must be treated as if they were rigid bodies since none of the strut lengths are allowed to change. The two triangles also form equilateral triangles, and therefore all angles inside the triangles are known. In this case node 1 will be fixated at the origin, the other node positions are prescribed as follows:

$$\begin{aligned}
x_1^{(2)} &= x_1^{(1)} + l_0\cos(\frac{\pi}{3} + \theta), & x_2^{(2)} &= x_2^{(1)} + l_0\sin(\frac{\pi}{3} + \theta),\\
x_1^{(3)} &= x_1^{(1)} - l_0\cos(\frac{\pi}{3} - \theta), & x_2^{(3)} &= x_2^{(1)} + l_0\sin(\frac{\pi}{3} - \theta),\\
x_1^{(4)} &= x_1^{(1)} + l_0\cos(\frac{\pi}{3} + \theta), & x_2^{(4)} &= x_2^{(1)} - l_0\sin(\frac{\pi}{3} + \theta),\\
x_1^{(5)} &= x_1^{(1)} - l_0\cos(\frac{\pi}{3} - \theta), & x_2^{(5)} &= x_2^{(1)} - l_0\sin(\frac{\pi}{3} - \theta),
\end{aligned} \tag{3.2}$$

where l_0 stands for the bar length and angle θ will be used as a measure of deformation.

The unit cell dimensions are dependent on the configuration, the further the pin-jointed truss is rotated the smaller these dimensions become and the unit cell is at its largest in the initial configuration, see section 2.3. A line parallel to the characteristic unit cell length L_{12}, as seen in figure 3.1, can always be drawn between nodes 2 and 5. If this were not the case then the unit cell would no longer be able to be tessellated throughout space as node 2 and 5 would not align, the same constraint also applies to node 3

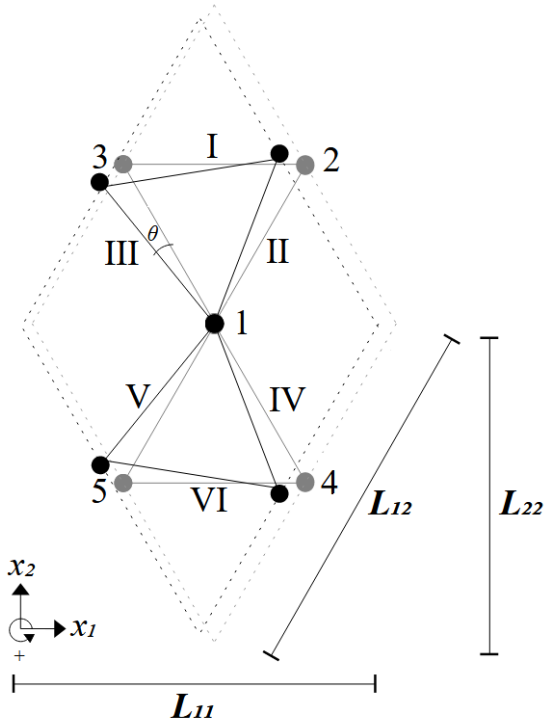

Figure 3.1: The Kagome unit cell used for the nonlinear matrix analysis. Node numbers are indicated with Arabic numbers and bar numbers are indicated with Roman numerals. In gray the undeformed configuration together with the undeformed unit cell. In black the deformed configuration and the corresponding unit cell. Angle θ indicates the degree of deformation.

and 4. Length L_{12} can be calculated by making use of the Pythagoras theorem and the relations defined in equation 3.2, length L_{11} and length L_{22} can be found from length L_{12}. The degree of deployment of the collapse mechanism is now dependent on angle θ and is defined as:

$$\begin{aligned} d_{11} &= \sqrt{(x_1^{(2)} - x_1^{(5)})^2 + (x_2^{(2)} - x_2^{(5)})^2}\varepsilon_{11}, \\ d_{12} &= \sqrt{(x_1^{(2)} - x_1^{(5)})^2 + (x_2^{(2)} - x_2^{(5)})^2}\varepsilon_{12}, \\ d_{22} &= \sqrt{(x_1^{(2)} - x_1^{(5)})^2 + (x_2^{(2)} - x_2^{(5)})^2}\sin(\frac{\pi}{3})\varepsilon_{22}. \end{aligned} \tag{3.3}$$

Rewriting the relations between the slave nodes and their master nodes, results in:

$$\begin{aligned} d_1^{(4)} &= d_1^{(3)} + \frac{\cos(\theta)}{\sqrt{2\cos(\theta)^2}}d_{11} - \frac{\sqrt{3}\cos(\theta)}{\sqrt{2\cos(\theta)^2}}d_{12}, \quad d_2^{(4)} = d_2^{(3)} + \frac{\cos(\theta)}{\sqrt{2\cos^2}}d_{12} - \frac{\cos(\theta)}{\sqrt{\cos(\theta)^2}}d_{22}, \\ d_1^{(5)} &= d_1^{(2)} - \frac{\cos(\theta)}{\sqrt{2\cos(\theta)^2}}d_{11} - \frac{\sqrt{3}\cos(\theta)}{\sqrt{2\cos(\theta)^2}}d_{12}, \quad d_2^{(5)} = d_2^{(2)} - \frac{\cos(\theta)}{\sqrt{2\cos(\theta)^2}}d_{12} - \frac{\cos(\theta)}{\sqrt{\cos(\theta)^2}}d_{22}. \end{aligned} \tag{3.4}$$

Finally, the augmented kinematic matrix $\boldsymbol{B}_{\text{aug}}$ that now depends on angle θ can be setup by using equation 3.4. $\boldsymbol{B}_{\text{aug}} =$

$$
\begin{bmatrix}
0 & 0 & \cos(\theta) & \sin(\theta) & -\cos(\theta) & -\sin(\theta) & 0 & 0 & 0 \\
-\cos(\frac{\pi}{3}+\theta) & -\sin(\frac{\pi}{3}+\theta) & \cos(\frac{\pi}{3}+\theta) & \sin(\frac{\pi}{3}+\theta) & 0 & 0 & 0 & 0 & 0 \\
\cos(\frac{\pi}{3}-\theta) & \sin(\frac{\pi}{3}-\theta) & 0 & 0 & -\cos(\frac{\pi}{3}-\theta) & -\sin(\frac{\pi}{3}-\theta) & 0 & 0 & 0 \\
-\cos(\frac{\pi}{3}+\theta) & \sin(\frac{\pi}{3}+\theta) & 0 & 0 & \cos(\frac{\pi}{3}+\theta) & -\sin(\frac{\pi}{3}+\theta) & \dfrac{\cos(\frac{\pi}{3}+2\theta)+\frac{1}{2}}{\sqrt{4\cos(\theta)^2}} & \dfrac{-\cos(\frac{\pi}{6}+2\theta)+\frac{\sqrt{3}}{2}}{\sqrt{2\cos(\theta)^2}} & \dfrac{\sin(\frac{\pi}{3}+2\theta)+\frac{\sqrt{3}}{2}}{\sqrt{2\cos(\theta)^2}} \\
\cos(\frac{\pi}{3}-\theta) & -\sin(\frac{\pi}{3}-\theta) & -\cos(\frac{\pi}{3}-\theta) & \sin(\frac{\pi}{3}-\theta) & 0 & 0 & \dfrac{\cos(2\theta-\frac{\pi}{3})+\frac{1}{2}}{\sqrt{4\cos(\theta)^2}} & \dfrac{\sin(\frac{\pi}{3}+2\theta)+\frac{\sqrt{3}}{2}}{\sqrt{2\cos(\theta)^2}} & \dfrac{\cos(\frac{\pi}{6}+2\theta)+\frac{\sqrt{3}}{2}}{\sqrt{2\cos(\theta)^2}} \\
0 & 0 & -\cos(\theta) & \sin(\theta) & \cos(\theta) & -\sin(\theta) & \dfrac{\cos(\theta)^2}{\sqrt{\cos(\theta)^2}} & \dfrac{-\sqrt{2}\sin(2\theta)}{\sqrt{2(\cos(2\theta)+1)^2}} & 0
\end{bmatrix}
\tag{3.5}
$$

Remember that the normal kinematic matrix $\boldsymbol{B}$ is a sub matrix of $\boldsymbol{B}_{\text{aug}}$, that consists of the 6 rows and first 6 columns of $\boldsymbol{B}_{\text{aug}}$. Both $\boldsymbol{B}_{\text{aug}}$ and $\boldsymbol{B}$ will only be valid for $-\pi/3 < \theta < \pi/3$, as will be illustrated in the following subsections.

3.2 Case 1: The initial configuration

The first case will be $\theta = 0$ or the initial configuration, this case will serve as a benchmark as the result should be the same as the one described in section 2.2. Substituting $\theta = 0$ into $\boldsymbol{B}_{\text{aug}}$ and calculating the row reduced echelon form or rref($\boldsymbol{B}_{\text{aug}}$) results in:

$$\text{rref}(\boldsymbol{B}_{\text{aug}}) = \begin{bmatrix} 1 & 0 & 0 & -\frac{\sqrt{3}}{2} & -1 & \frac{\sqrt{3}}{2} & 0 & 0 & 0 \\ 0 & 1 & 0 & -\frac{1}{2} & 0 & -\frac{1}{2} & 0 & 0 & 0 \\ 0 & 0 & 1 & 0 & -1 & 0 & 0 & 0 & 0 \\ 0 & 0 & 0 & 0 & 0 & 0 & 1 & 0 & 0 \\ 0 & 0 & 0 & 0 & 0 & 0 & 0 & 1 & 0 \\ 0 & 0 & 0 & 0 & 0 & 0 & 0 & 0 & 1 \end{bmatrix}. \tag{3.6}$$

The found matrix is rank deficient by three, thereby indicating that the nullspace

$$\boldsymbol{N}(\boldsymbol{B}_{\text{aug}}) = \begin{bmatrix} 0 & 1 & 0 & 1 & 0 & 1 & 0 & 0 & 0 \\ 1 & 0 & 1 & 0 & 1 & 0 & 0 & 0 & 0 \\ \sqrt{3} & 0 & 0 & 1 & 0 & -1 & 0 & 0 & 0 \end{bmatrix}^T, \tag{3.7}$$

must contain three linearly independent solutions. All found solutions are non strain-producing, indicated by the last three columns only containing zeros. The first two solutions are the rigid-body translations and the third solution is a non strain-producing mechanism. The same result can be found with the conventional matrix method:

$$\text{rref}(\boldsymbol{B}) = \begin{bmatrix} 1 & 0 & 0 & -\frac{\sqrt{3}}{2} & -1 & \frac{\sqrt{3}}{2} \\ 0 & 1 & 0 & -\frac{1}{2} & 0 & -\frac{1}{2} \\ 0 & 0 & 1 & 0 & -1 & 0 \\ 0 & 0 & 0 & 0 & 0 & 0 \\ 0 & 0 & 0 & 0 & 0 & 0 \\ 0 & 0 & 0 & 0 & 0 & 0 \end{bmatrix}. \tag{3.8}$$

Again the matrix is rank deficient by three and calculating the nullspace clearly shows the same linearly independent solutions as the solutions of the augmented matrix.

$$\boldsymbol{N}(\boldsymbol{B}) = \begin{bmatrix} 0 & 1 & 0 & 1 & 0 & 1 \\ 1 & 0 & 1 & 0 & 1 & 0 \\ \sqrt{3} & 0 & 0 & 1 & 0 & -1 \end{bmatrix}^T \tag{3.9}$$

The pin-jointed Kagome truss does not exhibit any strain-producing collapse mechanisms. Therefore the welded-jointed Kagome lattice relies on the axial stiffness of the lattice making the structure stretching governed. This case is in agreement with the solutions found in section 2.2.

3.3 Case 2: The intermediate steps

The second case will be applicable for $-\pi/3 < \theta < 0 \cup 0 < \theta < \pi/3$, or the intermediate configurations. Only positive values of θ will be mentioned as the negative equivalent angles give the same results. Reducing $\boldsymbol{B}_{\text{aug}}$ to its reduced echelon form results in:

$$\text{rref}(\boldsymbol{B}_{\text{aug}}) = \begin{bmatrix} 1 & 0 & 0 & 0 & -1 & 0 & 0 & 0 & \frac{-3(\cos(\theta)^2) + \sqrt{3}\cos(\theta)\sin(\theta)}{6\sin(\theta)\sqrt{(\cos(\theta)^2)}} \\ 0 & 1 & 0 & 0 & 0 & -1 & 0 & 0 & \frac{\sqrt{3}(\cos(\theta)^2 - \sqrt{3}\cos(\theta)\sin(\theta))}{6\sin(\theta)\sqrt{(\cos(\theta)^2)}} \\ 0 & 0 & 1 & 0 & -1 & 0 & 0 & 0 & \frac{-\sqrt{3}\cos(\theta)}{3\sqrt{(\cos(\theta)^2)}} \\ 0 & 0 & 0 & 1 & 0 & -1 & 0 & 0 & \frac{-\sqrt{3}\sqrt{1-(\sin(\theta)^2)}}{3\sin(\theta)} \\ 0 & 0 & 0 & 0 & 0 & 0 & 1 & 0 & \frac{-2\sqrt{3}}{3} \\ 0 & 0 & 0 & 0 & 0 & 0 & 0 & 1 & 0 \end{bmatrix}. \tag{3.10}$$

The rref form is also rank deficient by three, similar to the undeformed configuration. The three linearly independent solutions therefore are:

Nullspace $\boldsymbol{N}(\boldsymbol{B}_{\text{aug}})$:

$$\begin{bmatrix} 0 & 1 & 0 & 1 & 0 & 1 & 0 & 0 & 0 \\ 1 & 0 & 1 & 0 & 1 & 0 & 0 & 0 & 0 \\ \frac{-3(\cos(\theta)^2) + \sqrt{3}\cos(\theta)\sin(\theta)}{6\sin(\theta)\sqrt{(\cos(\theta)^2)}} & \frac{-\sqrt{3}(\cos(\theta)^2 + \sqrt{3}\cos(\theta)\sin(\theta))}{6\sin(\theta)\sqrt{(\cos(\theta)^2)}} & \frac{\sqrt{3}\cos(\theta)}{3\sqrt{(\cos(\theta)^2}} & \frac{-\sqrt{3}\sqrt{1-(\sin(\theta)^2)}}{3\sin(\theta)} & 0 & 0 & \frac{2\sqrt{3}}{3} & 0 & 1 \end{bmatrix}^T. \tag{3.11}$$

The solutions found are now no longer all non strain-producing, instead a strain-producing mechanism has appeared as indicated by non zero entries in the last three columns. The movements of the nodes are dependent on angle θ, while the deformation of the unit cell is not. And while $\boldsymbol{B}$ is still a sub matrix of $\boldsymbol{B}_{\text{aug}}$ the number of mechanisms found is no longer the same.

$$\text{rref}(\boldsymbol{B}) = \begin{bmatrix} 1 & 0 & 0 & 0 & -1 & 0 \\ 0 & 1 & 0 & 0 & 0 & -1 \\ 0 & 0 & 1 & 0 & -1 & 0 \\ 0 & 0 & 0 & 1 & 0 & -1 \\ 0 & 0 & 0 & 0 & 0 & 0 \\ 0 & 0 & 0 & 0 & 0 & 0 \end{bmatrix} \tag{3.12}$$

$$\boldsymbol{N}(\boldsymbol{B}) = \begin{bmatrix} 0 & 1 & 0 & 1 & 0 & 1 \\ 1 & 0 & 1 & 0 & 1 & 0 \end{bmatrix}^T \tag{3.13}$$

The mechanism found in the nullspace of the undeformed configuration is now no longer a part of $\boldsymbol{N}(\boldsymbol{B})$, instead only the rigid body translations appear.

The pin-jointed truss now has for any angle θ, bounded by $-\pi/3 < \theta < 0 \cup 0 < \theta < \pi/3$, a strain-producing mechanism. Therefore the welded-jointed equivalent lattice relies on the rotational stiffness and strength of the nodes and struts for its macroscopic stiffness, making the structure bending-dominated.

3.3.1 Example: The triangular-triangular configuration

Both Hutchinson and Fleck (2006) [9] and Pronk *et al.* [15] have compared the pin-jointed Triangular-triangular truss or T-T to the pin-jointed Kagome truss. The truss configuration can be seen in figure 1.2. It can easily be shown that the nonlinear method described in this chapter can find the linearised version of the mechanisms of the T-T truss. This is because the configuration can be described by equation 3.2, as this configuration occurs when angle $\theta = \pi/6$ and is therefore classified as an intermediate step towards collapse.

Substituting $\theta = \pi/6$ in matrix 3.10 results in the following row reduced matrix:

$$\text{rref}(\boldsymbol{B}_{\text{aug}}) = \begin{bmatrix} 1 & 0 & 0 & 0 & -1 & 0 & 0 & 0 & -\frac{2\sqrt{3}}{3} \\ 0 & 1 & 0 & 0 & 0 & -1 & 0 & 0 & 0 \\ 0 & 0 & 1 & 0 & -1 & 0 & 0 & 0 & -\frac{\sqrt{3}}{3} \\ 0 & 0 & 0 & 1 & 0 & -1 & 0 & 0 & -1 \\ 0 & 0 & 0 & 0 & 0 & 0 & 1 & 0 & \frac{-2\sqrt{3}}{3} \\ 0 & 0 & 0 & 0 & 0 & 0 & 0 & 1 & 0 \end{bmatrix}. \tag{3.14}$$

Calculating the nullspace:

$$\boldsymbol{N}(\boldsymbol{B}_{\text{aug}}) = \begin{bmatrix} 0 & 1 & 0 & 1 & 0 & 1 & 0 & 0 & 0 \\ 1 & 0 & 1 & 0 & 1 & 0 & 0 & 0 & 0 \\ \frac{2\sqrt{3}}{3} & 0 & \frac{\sqrt{3}}{3} & 1 & 0 & 0 & \frac{2\sqrt{3}}{3} & 0 & 1 \end{bmatrix}^T. \tag{3.15}$$

The nullspace of this configuration has like all other intermediate steps one strain-producing mechanism and 2 rigid-body modes.

3.4 Case 3: The full collapse

When $\theta = \pi/3$, the fully triangular configuration is attained, see figure 1.3. Remember that this configuration only looks similar to the true fully triangular truss. The truss is simply rotated but this does not change the nodal connectivity of the truss itself. The true fully triangular truss has a nodal connectivity of 6, while the folded version only has a nodal connectivity of 4, this will have impact on the response to macroscopic loads. The pin-jointed folded truss will react differently to different load cases, unlike the previously discussed configurations. Loading the structure with an uni- or biaxial compressive load will induce a stiffer response than any other loading case. This is due to a restriction in the collapse motion. The bars of the structure will be pushed together, essentially doubling the in-plane thickness of the bars, as these bars should not be able to cross over each other. Therefore the reaction of the folded configuration will be the same as if it was a true fully triangular truss. Any other load case

would open up the structure, by either pulling it open in when loaded with uni- or biaxial tension or sheared open with a shear load, therefore no extra stiffness is added to the structure. These properties do not apply to the regular fully triangular pin-jointed truss as the bars are not folded against each other.

3.4.1 Non compressive load cases

The earlier found $\boldsymbol{B}_{\text{aug}}$ based on the collapse of the Kagome truss is still valid for all load cases except uni- or biaxial compression. Simply substituting $\theta = \pi/3$ in $\boldsymbol{B}_{\text{aug}}$ results in:

$$\text{rref}(\boldsymbol{B}_{\text{aug}}) = \begin{bmatrix} 1 & 0 & 0 & 0 & -1 & 0 & 0 & 0 & 0 \\ 0 & 1 & 0 & 0 & 0 & -1 & 0 & 0 & \frac{2}{3} \\ 0 & 0 & 1 & 0 & -1 & 0 & 0 & 0 & -\frac{\sqrt{3}}{3} \\ 0 & 0 & 0 & 1 & 0 & -1 & 0 & 0 & \frac{1}{3} \\ 0 & 0 & 0 & 0 & 0 & 0 & 1 & 0 & -\frac{2\sqrt{3}}{3} \\ 0 & 0 & 0 & 0 & 0 & 0 & 0 & 1 & 0 \end{bmatrix}, \tag{3.16}$$

$$\boldsymbol{N}(\boldsymbol{B}_{\text{aug}}) = \begin{bmatrix} 0 & 1 & 0 & 1 & 0 & 1 & 0 & 0 & 0 \\ 1 & 0 & 1 & 0 & 1 & 0 & 0 & 0 & 0 \\ 0 & -\frac{2}{3} & \frac{\sqrt{3}}{3} & -\frac{1}{3} & 0 & 0 & \frac{2\sqrt{3}}{3} & 0 & 1 \end{bmatrix}^T, \tag{3.17}$$

$$\text{rref}(\boldsymbol{B}) = \begin{bmatrix} 1 & 0 & 0 & 0 & -1 & 0 \\ 0 & 1 & 0 & 0 & 0 & -1 \\ 0 & 0 & 1 & 0 & -1 & 0 \\ 0 & 0 & 0 & 1 & 0 & -1 \\ 0 & 0 & 0 & 0 & 0 & 0 \\ 0 & 0 & 0 & 0 & 0 & 0 \end{bmatrix}, \tag{3.18}$$

$$\boldsymbol{N}(\boldsymbol{B}) = \begin{bmatrix} 0 & 1 & 0 & 1 & 0 & 1 \\ 1 & 0 & 1 & 0 & 1 & 0 \end{bmatrix}^T. \tag{3.19}$$

The nullspace of this configuration has like all other rotated configurations a strain-producing mechanism, implying that the welded-jointed structure will behave in a bending-dominated way. Please note that mathematically it is viable to multiply the strain-producing mechanism with -1, this will switch the direction of collapse. Making a linearised representation based on both mechanisms will reveal that one of the mechanisms will simply rotate the truss open, while the other mechanism will allow the bars to cross over each other. Since bars cannot cross over this solution is not physically viable.

3.4.2 A uni- or biaxial compressive load case

The augmented compatibility matrix has to be reformulated for this case to combat the issues of bars being allowed to cross over each other. The overlapping bars will be considered to be single bars and overlapping nodes will also be considered to be single nodes. This overlap should be seen as two bars lying side by side, essentially doubling the in-plane thickness of the bars. In order to simulate this restriction in movement the nodal connectivity has been increased from 4 to 6. A bigger unit cell has been chosen to calculate the mechanisms more easily. The new unit cell is shown in figure 3.2. In essence, under these specific loading conditions the folded truss will behave like the fully triangular truss.

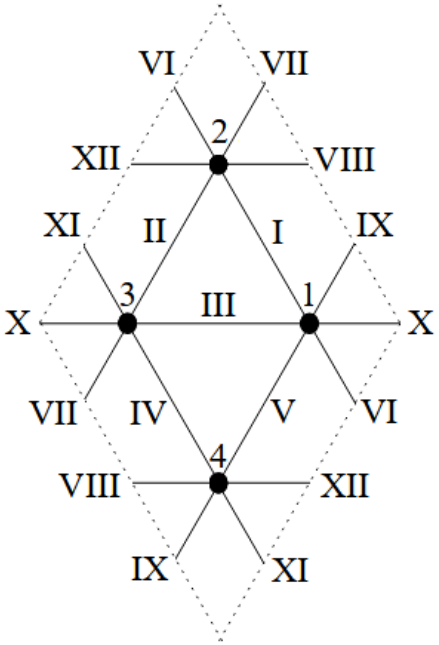

Figure 3.2: The fully triangular configuration used to investigate the purely compressive load case. The overlapping nodes have been removed and will be treated as if they were one node, the same will be done for the overlapping bars, in order to simulate the restriction in movement.

$$\boldsymbol{B}_{\text{aug}} = \begin{bmatrix} -\frac{1}{2} & -\frac{\sqrt{3}}{2} & \frac{1}{2} & \frac{\sqrt{3}}{2} & 0 & 0 & 0 & 0 & 0 & 0 & 0 \\ 0 & 0 & \frac{1}{2} & \frac{\sqrt{3}}{2} & -\frac{1}{2} & -\frac{\sqrt{3}}{2} & 0 & 0 & 0 & 0 & 0 \\ 1 & 0 & 0 & 0 & -1 & 0 & 0 & 0 & 0 & 0 & 0 \\ 0 & 0 & 0 & 0 & -\frac{1}{2} & \frac{\sqrt{3}}{2} & \frac{1}{2} & -\frac{\sqrt{3}}{2} & 0 & 0 & 0 \\ \frac{1}{2} & \frac{\sqrt{3}}{2} & 0 & 0 & -\frac{1}{2} & -\frac{\sqrt{3}}{2} & 0 & 0 & 0 & 0 & 0 \\ -\frac{1}{2} & \frac{\sqrt{3}}{2} & \frac{1}{2} & -\frac{\sqrt{3}}{2} & 0 & 0 & 0 & 0 & \frac{1}{4} & -\frac{\sqrt{3}}{2} & \frac{\sqrt{3}}{2} \\ 0 & 0 & -\frac{1}{2} & -\frac{\sqrt{3}}{2} & \frac{1}{2} & \frac{\sqrt{3}}{2} & 0 & 0 & \frac{1}{4} & \frac{\sqrt{3}}{2} & \frac{\sqrt{3}}{2} \\ 0 & 0 & -1 & 0 & 0 & 0 & 1 & 0 & \frac{1}{2} & \frac{\sqrt{3}}{2} & 0 \\ -\frac{1}{2} & -\frac{\sqrt{3}}{2} & 0 & 0 & 0 & 0 & \frac{1}{2} & \frac{\sqrt{3}}{2} & \frac{1}{4} & \frac{\sqrt{3}}{2} & \frac{\sqrt{3}}{2} \\ -1 & 0 & 0 & 0 & 1 & 0 & 0 & 0 & 1 & 0 & 0 \\ 0 & 0 & 0 & 0 & \frac{1}{2} & -\frac{\sqrt{3}}{2} & -\frac{1}{2} & \frac{\sqrt{3}}{2} & \frac{1}{4} & -\frac{\sqrt{3}}{2} & \frac{\sqrt{3}}{2} \\ 0 & 0 & 1 & 0 & 0 & 0 & -1 & 0 & \frac{1}{2} & -\frac{\sqrt{3}}{2} & 0 \end{bmatrix} \tag{3.20}$$

$$\boldsymbol{N}(\boldsymbol{B}_{\text{aug}}) = \begin{bmatrix} 0 & 1 & 0 & 1 & 0 & 1 & 0 & 1 & 0 & 0 & 0 \\ 1 & 0 & 1 & 0 & 1 & 0 & 1 & 0 & 0 & 0 & 0 \end{bmatrix}^T \tag{3.21}$$

The augmented kinematic matrix $\boldsymbol{B}_{\text{aug}}$ is now rank deficient by 2, this is in contrast to the rank deficiency of all other configurations. The found nullspace now only consists of the two rigid-body translations, and no longer has a mechanism. The welded-jointed lattice will react in a stretching-dominated way as indicated by the absence of an inextensional collapse mechanism.

It is important to note that this configuration no longer fulfills Maxwell's condition as the number of linearly independent states of self-stress is no longer equal to the number of linearly independent inextensional displacement modes. This can be checked by remembering that $\boldsymbol{B} = \boldsymbol{A}^T$ and calculating the nullspace of the equilibrium matrix. This will result in 6 linearly independent states of self-stress. By violating this criterion the welded-jointed lattice no longer fulfills the search criteria for lattice architectures suitable for actuation proposed by Pronk *et al.* [15].

3.5 Discussion

The shift from a pin-jointed truss only containing non strain-producing mechanisms into a pin-jointed truss containing one or more strain-producing mechanisms occurs immediately after triggering the finite mechanism. This implies no other configuration other than the welded-jointed Kagome exhibits stretching-dominated elastic response, see table 3.1. Only specific loading conditions in a fully collapsed configuration can recover the stretching-dominated elastic response. The rotated pin-jointed structures will therefore no longer be able to support any arbitrary 2D macroscopic load case, implying a reduction in the macroscopic stiffness of the rigidly-jointed lattice material.

Investigating the non strain-producing mechanism and the strain-producing mechanisms shows that these mechanisms are connected. If the non strain-producing mechanism of the undeformed configuration shows the initial collapse then the strain-producing mechanisms show the continued motion after the initial rotation. Therefore exciting the mechanism will immediately result in the non strain-producing mechanism being converted into a strain-producing mechanism. This also implies that the strain-producing mechanism is a finite mechanism. The total number of mechanisms is therefore the same for any configuration, until the fully collapsed configuration under a uni- or biaxial compressive load.

All strain-producing mechanisms have the same unit cell deformation that is independent of angle θ, which would suggest that the shape of the unit cell is preserved at any theta but the size is not.

	Kagome	intermediate configurations	fully collapsed	fully triangulated
	$\theta = 0$	$-\frac{\pi}{3} < \theta < 0$ $0 < \theta < \frac{\pi}{3}$	$\theta = -\frac{\pi}{3} \cup \frac{\pi}{3}$	$\theta = -\frac{\pi}{3} \cup \frac{\pi}{3}$
Non strain-producing mechanisms	3	2	2	2
Strain-producing mechanisms	0	1	1	0
States of self-stress	3	2	2	6
Deformation behavior in the rigidly-jointed form	Stretching-dominated	Bending-dominated	Bending-dominated	Stretching-dominated

Table 3.1: Static and kinematic properties of the Kagome truss during collapse.

4. Macroscopic properties

Chapter 3 discussed pin-jointed repetitive truss structures and the implication of exciting a finite mechanism on the static and kinematic determinacy of the infinite truss. The results of the pin-jointed truss and its collapse mechanism dictate the deformation behaviour of the equivalent welded-jointed lattice. As discussed in chapter 3, only the welded-jointed Kagome configuration exhibits the stretching-dominated property. Lattices that are stretching-dominated will be stiffer than bending-dominated lattices. This raises the question how the elastic properties of the other welded-jointed configurations, using θ described in chapter 3 as means of introducing twist, hold up against the elastic properties of the rigidly-jointed Kagome configuration.

This chapter will start by defining how the macroscopic Young's modulus of an infinite welded-jointed lattice is calculated. This is done by means of a homogenisation procedure on a doubly periodic unit cell. Afterwards a finite element model will be described. This model is then used to calculate the elastic response of the lattice to applied strain.

4.1 Homogenisation

Classical continuum theory cannot be used for welded-jointed lattice materials as it is based on the assumption that the transfer of load between neighbouring material points only occurs through a force vector, leading to the definition of symmetric stresses and strains. This assumption cannot be applied to welded-jointed lattice materials as the characteristic unit cell dimensions are considered to be much smaller than the wavelength λ of the stresses and strains [13].

The effective macroscopic stress Σ_{ij} and macroscopic strain E_{ij} are calculated with the use of a homogenization scheme. The scheme is based on the equivalence of the work done by the applied forces averaged over the representative volume element, W_{ext}, to the work done by the internal work done by the material, W_{int}:

$$W_{\text{ext}} = W_{\text{int}} \tag{4.1}$$

$$W_{\text{ext}} = \Sigma_{ij} E_{ij} \tag{4.2}$$

$$W_{\text{int}} = \frac{1}{V} \sum_{k=1}^{N} f_i^{(k)} u_i^{(k)} \tag{4.3}$$

Where V stands for the volume of the Representative element, $u_i^{(k)}$ and $f_i^{(k)}$ are the imposed displacement and the corresponding force on the boundary node k, with k = 1, ..., N, and N being the total number of boundary nodes of the representative volume element. Σ_{ij} and E_{ij} stand for the representative macroscopic stress and strain tensors. The displacement can be expressed in terms of the macroscopic strain and the local coordinate of the associated node $x_j^{(k)}$:

$$u_i^{(k)} = E_{ij} x_j^{(k)} \tag{4.4}$$

Rewriting gives the macroscopic strains E_{ij}:

$$E_{ij} = \frac{1}{V} \sum_{k=1}^{N} \frac{1}{2} (n_i^{(k)} u_j^{(k)} + n_j^{(k)} u_i^{(k)}) ds^{(k)}, \tag{4.5}$$

where $ds^{(k)}$ and $\boldsymbol{n}^{(k)}$ stand for the area and the unit normal vector for the surface associated with node k. The force acting on node k can be similarly given in terms of macroscopic stress components:

$$f_i^{(k)} = \Sigma_{ij} n_j^{(k)} ds^{(k)}, \tag{4.6}$$

rewriting:

$$\Sigma_{ij} = \sum_{k=1}^{N} \frac{1}{2} (f_i^{(k)} x_j^{(k)} + f_j^{(k)} x_i^{(k)}), \tag{4.7}$$

see [15].

Finally the macroscopic Young's modulus can be calculated as:

$$E^* = \frac{\Sigma_{ii}}{E_{ii}}. \tag{4.8}$$

4.1.1 Homogenisation of the Kagome lattice

The unit cell has periodic boundary conditions in both the x_1- and x_2-direction, implying an infinitely large lattice structure. The representative volume element is shown in figure 4.1. Firstly, the nodes located on the boundary of the unit cell will be subjected to a displacement field to determine the macroscopic strain. Secondly, the macroscopic stress will be found with the use of the reaction forces resulting from the previously placed displacement field.

The configurations, that are twisted in accordance with the mechanism of the pin-jointed truss, will be indicated with angle θ as described in figure 4.4. Inside the unit cell a symmetry line can be drawn at $x_2 = 0$. This symmetry line is valid for any configuration bounded by $0 \leq \theta < \pi/3$.

All bar lengths have a length of l_0 and an in-plane thickness of w. The length between the dashed symmetry line $x_2 = 0$ and $x_2^{(1)}$ will be defined height H, the length between $x_1^{(3)}$ and $x_1^{(4)}$ will be defined as length L and as these coordinates will accurately describe the lengths even when the welded-jointed lattice is twisted in accordance with the mechanism, due to the periodicity constraint. Length H is also equal to $L\sin(\pi/3)$. A thickness t will be equal to the out-of-plane thickness. The surface area dS corresponding to the nodes is equal for every node and is defined as Lt, similarly the top area A_{top} is equal to Lt. Lastly, the volume V for this representative element is equal to $2LHt$. All measurements have been summarised in table 4.1.

Length	L	$x_1^{(4)} - x_1^{(3)}$
Height	H	$x_2^{(1)}$ or $L\sin(\frac{\pi}{3})$
Surface area	dS	Lt
Top area	A_{top}	Lt
Volume	V	$2LHt$
Relative density	$\bar{\rho}(w)$	$\sqrt{3}\frac{w}{l}$

Table 4.1: Measurements of the unit cell depicted in figure 4.1

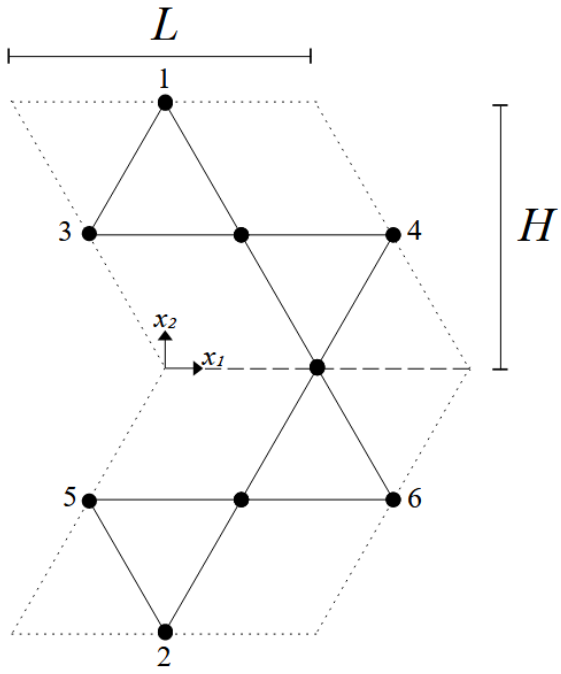

Figure 4.1: A representative volume element of the Kagome lattice. The unit cell can be tessellated by shifting the cell with length L in the x_1-direction and by shifting the cell by length $2H$ in the x_2-direction. Only the nodes on the unit cell boundary have been numbered as the reaction of the internal nodes to applied strains and forces is not important for the averaging process.

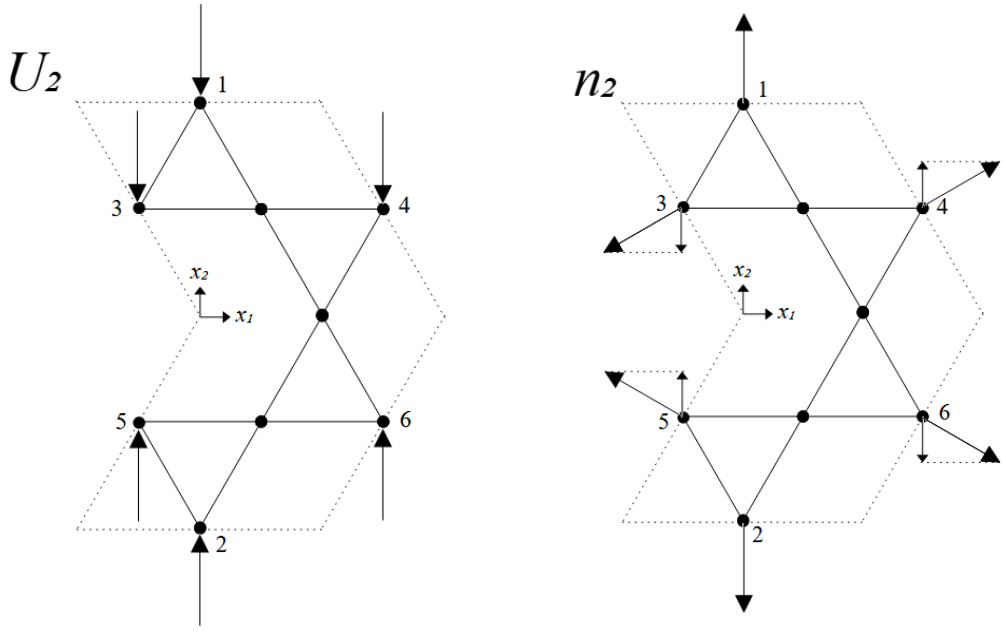

(a) (b)

Figure 4.2: (a) A uniaxial displacement field U_2 placed on the representative volume element of the Kagome lattice. (b) The unit normals of the unit cell boundary.

Figure 4.2(a) shows the prescribed displacement U_2 and figure 4.2(b) the unit normal vectors $\boldsymbol{n}$ associated

with the boundary nodes. The macroscopic strain as described in equation 4.5 can be rewritten as the uniaxial strain E_{22}:

$$E_{22} = \frac{1}{V}\sum_{k=1}^{6} n_2^{(k)} u_2^{(k)} ds^{(k)}. \tag{4.9}$$

Expanding the summation of equation 4.9 leads to:

$$\sum_{k=1}^{6} n_2^{(k)} u_2^{(k)} ds^{(k)} = [n_2^{(1)} u_2^{(1)} ds^{(1)} + n_2^{(2)} u_2^{(2)} ds^{(2)}] + [n_2^{(3)} u_2^{(3)} ds^{(3)} + n_2^{(4)} u_2^{(4)} ds^{(4)} + n_2^{(5)} u_2^{(5)} ds^{(5)} + n_2^{(6)} u_2^{(6)} ds^{(6)}].$$

The following simplifications can be applied due to the periodicity and symmetry conditions of the unit cell, $u_2^{(1)} = u_2^{(3)} = u_2^{(4)} = -u_2^{(2)} = -u_2^{(5)} = -u_2^{(6)}$, resulting in:

$$\sum_{k=1}^{6} n_2^k u_2^{(k)} ds^{(k)} = [n_2^{(1)} - n_2^{(2)}] u_2^{(1)} ds^{(1)} + [n_2^{(3)} + n_2^{(4)} - n_2^{(5)} - n_2^{(6)}] u_2^{(3)} ds^{(3)}.$$

The n_2 components of the normals can also be related to each other, namely: $n_2^{(1)} = -n_2^{(2)}$ and $n_2^{(3)} = -n_2^{(4)} = -n_2^{(5)} = n_2^{(6)}$, substitution results in:

$$\sum_{k=1}^{6} n_2^{(k)} u_2^{(k)} = [n_2^{(1)} - (-n_2^{(1)})] u_2^{(1)} ds^{(1)} + [n_2^{(3)} + (-n_2^{(3)}) - (-n_2^{(3)}) - (+n_2^{(3)})] u_2^{(3)} ds^{(3)} = 2 n_2^{(1)} u_2^{(1)} ds^{(1)},$$

$$E_{22} = \frac{2 n_2^{(1)} u_2^{(1)} ds^{(1)}}{V} = \frac{2 n_2^{(1)} u_2^{(1)} Lt}{2LHt},$$

and finally the uniaxial strain E_{22} can be expressed as:

$$E_{22} = \frac{U_2}{H}. \tag{4.10}$$

Very similar steps can be taken to show that the uniaxial strain in x_1-direction, or E_{11}, is expressed as:

$$E_{11} = -\frac{2U_1}{L}, \tag{4.11}$$

with U_1 being a uniaxial displacement field in x_1-direction, see appendix C.

Figure 4.3 shows the uniaxial compressive load case resulting from the prescribed displacements that will be used to determine the macroscopic stress Σ_{22}. Starting with equation 4.7 the uniaxial compression can be expressed as:

$$\Sigma_{22} = \frac{1}{V}\sum_{k=1}^{6} x_2^{(k)} f_2^{(k)}. \tag{4.12}$$

Expanding the summation from equation 4.13 results in:

$$\sum_{k=1}^{6} x_2^{(k)} f_2^{(k)} = [x_2^{(1)} f_2^{(1)} + x_2^{(2)} f_2^{(2)}] + [x_2^{(3)} f_2^{(3)} + x_2^{(4)} f_2^{(4)} + x_2^{(5)} f_2^{(5)} + x_2^{(6)} f_2^{(6)}].$$

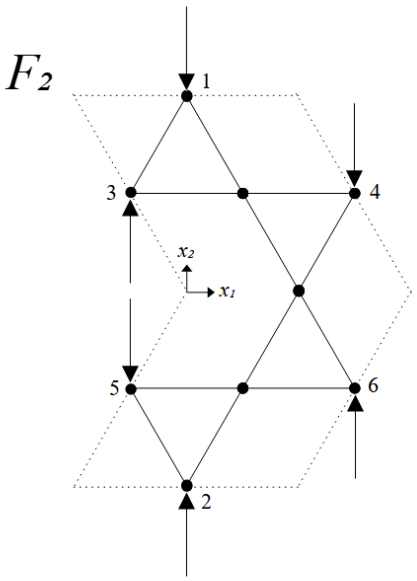

Figure 4.3: The reaction forces in x_2-direction, as a result of placing displacement field U_2 on the nodes, can be seen in this figure.

The x_2 coordinates can be related to each other due to periodicity and symmetry constraints. $x_2^{(1)} = -x_2^{(2)}$, $x_2^{(3)} = x_2^{(4)} = -x_2^{(5)} = -x_2^{(6)}$, these relations are valid for any configuration between $0 \leq \theta < \pi/3$, therefore the summation can be reduced to:

$$\sum_{k=1}^{6} x_2^{(k)} f_2^{(k)} = x_2^{(1)}[f_2^{(1)} - f_2^{(2)}] + x_2^{(3)}[f_2^{(3)} + f_2^{(4)} - f_2^{(5)} - f_2^{(6)}].$$

The summation can be further reduced by realising that all the forces are equivalent in length to each other, resulting in:

$$\sum_{k=1}^{6} x_2^{(k)} f_2^{(k)} = x_2^{(1)}[f_2^{(1)} - -f_2^{(1)}] + x_2^{(3)}[f_2^{(3)} + -f_2^{(3)} - -f_2^{(3)} - +f_2^{(3)}] = 2x_2^{(1)} f_2^{(1)},$$

$$\Sigma_{22} = \frac{2x_2^{(1)} f_2^{(1)}}{2LHt} = \frac{2H f_2^{(1)}}{2LHt}.$$

Finally, the macroscopic uniaxial stress can be expressed as:

$$\Sigma_{22} = \frac{F_2}{A_{top}}. \tag{4.13}$$

Using equations 4.13 and 4.10 result in the macroscopic Young's modulus, expressed in terms of applied displacement and the reaction forces:

$$E^* = \frac{\Sigma_{22}}{E_{22}} = \frac{H}{A_{top}} \frac{F_2}{U_2}. \tag{4.14}$$

This relation is valid for all configurations bounded by $0 \leq \theta < \pi/3$ and as the lattice behaves isotropic.

4.2 Model

The results found in the previous section will now be used to calculate the macroscopic Young's modulus of the welded-jointed lattice. All finite element calculations are performed in the commercial finite element program ABAQUS (2020 edition). The material properties of the bars are representative of aluminium with $E_{alu} = 70$ Gpa and $\nu = 0.33$ and have linear elastic behavior. The bars are assumed to have a rectangular cross-section, where the out-of-plane thickness t is a constant and the in-plane thickness w will be varied in order to systematically vary relative densities $\bar{\rho}$. The in-plane thickness must be bounded in order to preserve the slenderness of the bars, therefore the relative density will be varied from 0.01 to 0.15, corresponding to aspect ratios $0.0058 < \frac{w}{l} < 0.087$. The in-plane thickness will only be calculated for the non-twisted Kagome micro-architecture, and these thicknesses will be preserved for all other twisted Kagome configurations. The elements used in the finite element calculations are three-node quadratic Timoshenko beam elements, these elements are referred to as B22 elements in ABAQUS. The calculations were both performed with and without accounting for the geometric nonlinearities. Angle θ, indicating the amount of twist, will be varied between $0 \leq \theta < \pi/3$, the negative angles would give the same result, as it only switches the direction of twist, and will therefore not be analysed further.

The unit cell, representing an infinitely large lattice, may even be further reduced if internal symmetries are present. The unit cell presented in figure 4.1 can therefore be reduced to the one illustrated in figure 4.4 by making use of the symmetry line at $x_2 = 0$.

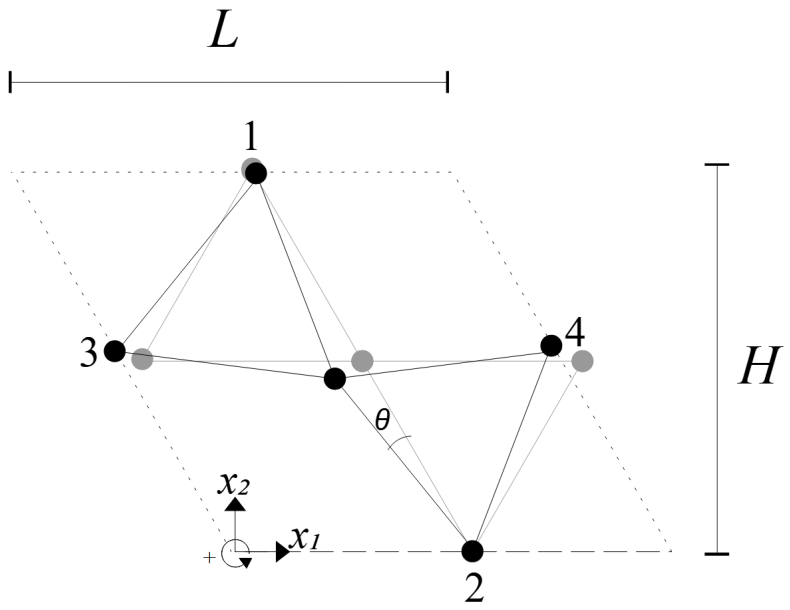

Figure 4.4: The representative welded-jointed structure used for the Finite Element analysis. Angle θ determines the amount of twist in the undeformed configuration. The dotted lines stand for the periodic boundary and the dashed line is the symmetric boundary.

Starting with the periodic boundaries. Nodes 3 and 4 must align in x_2-direction, thus the displacement of node 3 and 4 in x_2-direction must be equal, while in x_1-direction it must be equal and opposite. The rotations of the periodic nodes must also be equal to the rotation of their counterparts, to properly fit.

The symmetry conditions in this case need to be defined for nodes 1 and 2. The symmetry condition that is applicable to node 1 is not obvious from the unit cell depicted in figure 4.4. Instead it becomes more clear when taking figure 4.1 into consideration. In figure 4.1 node 1 and node 2 (not the same node 2 as in figure 4.4) form a pair. In order for node 1 and node 2 to properly fit they must have an equal rotation,

due to the periodicity constraint. At the same time node 2 is a mirror image of node 1 and therefore the symmetric constraint implies that the rotation of these nodes is equal but opposite. Both conditions can only be satisfied at the same time if the rotation of node 1 is therefore equal to zero. The displacement of node 2, as depicted in figure 4.4, in x_2-direction must be equal to zero as the loading will be symmetrical on both sides, effectively nullifying each other. The same applies to the rotation of the node.

Combining the conditions results in:

Node 1:			$\phi^{(1)} = 0.$
Node 2:		$u_2^{(2)} = 0,$	$\phi^{(2)} = 0.$
Node 3 & 4:	$u_1^{(3)} = -u_1^{(4)},$	$u_2^{(3)} = u_2^{(4)},$	$\phi^{(3)} = \phi^{(4)}.$

A small displacement will be applied to node 1 in x_2-direction. The effective strain in x_2-direction, based on section 4.1 can be written as:

$$u_2^{(1)} - u_2^{(2)} = \varepsilon_{22}^* H, \tag{4.15}$$

and the effective strain in x_1-direction is written as:

$$u_1^{(4)} - u_1^{(3)} = \varepsilon_{11}^* L. \tag{4.16}$$

Similarly, the effective stress in x_2-direction, based on section 4.1, is expressed as:

$$\sigma_{22}^* = \frac{rf_2^{(1)}}{Lt}, \tag{4.17}$$

where $rf_2^{(1)}$ stands for the reaction force in x_2-direction of node 1.

Combining equation 4.15 and 4.17 results in a normalised macroscopic Young's modulus E^*:

$$E^* = \frac{\sigma_{22}^*}{\varepsilon_{22}^*}\frac{1}{E_{alu}} = \frac{H}{Lt}\frac{rf_2^{(1)}}{u_2^{(1)} - u_2^{(2)}}\frac{1}{E_{alu}}. \tag{4.18}$$

The macroscopic Poisson's ratio is found using equations 4.15 and 4.16:

$$\nu = -\frac{\varepsilon_{11}^*}{\varepsilon_{22}^*}. \tag{4.19}$$

4.3 Results

4.3.1 Geometrically linear calculations

In total the Young's moduli and Poisson's ratios have been calculated several times for different undeformed rigidly-jointed configurations. The first three configurations are used to study what happens when a small initial twist is applied and the rest are used to study how larger initial twists affect the Young's modulus and the Poisson's ratio. These repetitive rigidly-jointed lattices are subjected to an uniaxial compression with $\varepsilon_{22} = 0.01$.

In the geometrically linear setting the Young's modulus of the twisted configurations with small values of θ were predicted to be similar to that of the Kagome lattice, see figure 4.5(a). For the Kagome

configuration the relation between the normalised Young's modulus E^* as a function of the relative density $\bar{\rho}$ scales linearly indicating stretching-dominated elastic deformation. This linearity is due to the axial stiffness of the beam scaling linearly with the in-plane thickness w. This is clearly visible in figure 4.6, as the bars in subfigures 4.6(b)-4.6(f) are being deformed by stretching and compressing the bars. This is also the only configuration with a constant Poisson's ratio as can be seen in figure 4.5(b).

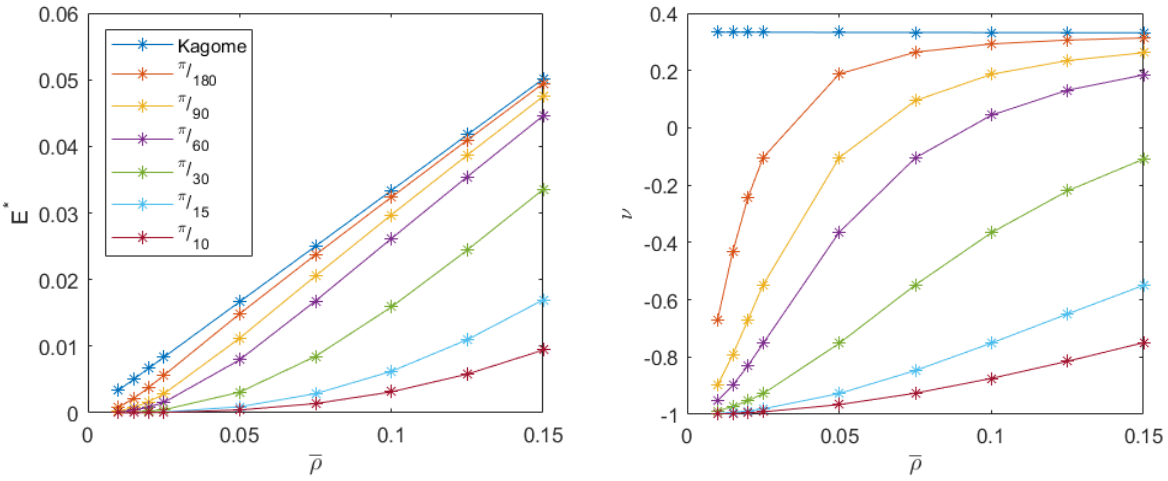

(a) (b)

Figure 4.5: (a) The normalised Young's modulus E^* as a function of the relative density $\bar{\rho}$ in the geometrically linear setting. (b) The Poisson's ratio ν as a function of the relative density $\bar{\rho}$ in the geometrically linear setting. In both subfigures the lines represent the different configurations, ranging from no twist to a twist of $\theta = \pi/10$.

None of the initially twisted configurations can be described as scaling linearly, the configurations with large twist angles can be better described as scaling cubically as a function of the relative density. The cubical scaling indicates a bending-dominated response and is due to the bending stiffness of a beam scaling cubically with the in-plane thickness w. Investigating the elastic response under uniaxial compression in a similar fashion as the Kagome configuration reveals a fundamentally different response. The lattice deformation of the twisted Kagome micro-architecture is reminiscent to the collapse mechanism of the pin-jointed truss, see figure 4.7, instead of stretching or compressing the bars themselves. As a demonstration the initial twist angle of $\pi/180$ was chosen combined with the same relative density and applied strain as the Kagome lattice in figure 4.6. The other investigated configurations behave in a similar fashion as the one depicted, simply rotating as a response to the applied strain. The Young's modulus of the twisted configurations $\pi/180$ and $\pi/90$ are able to get within 90% of the Young's modulus of the Kagome lattice, but only for the higher relative densities $\bar{\rho} \geq 0.075$. The Young's modulus of the lower relative densities instead is only a fraction of the untwisted counterparts.

The Poisson's ratio of the twisted configurations with small twist angles is very sensitive to the relative density, unlike the Kagome configuration which does not depend on θ. The configurations with small initial twist angles that are able to approach the same Young's modulus of the Kagome lattice also approach the same Poisson's ratio as the Kagome lattice. The relative density of the lattice plays an important factor in the preservation of the Young's modulus and the Poisson's ratio of the Kagome lattice. The same does not apply to the configurations with large initial twists. Varying the relative density no longer results in a strongly fluctuating Poisson's ratio, instead the ratio still fluctuates but no longer gets even remotely close to Poisson's ratio of the Kagome configuration.

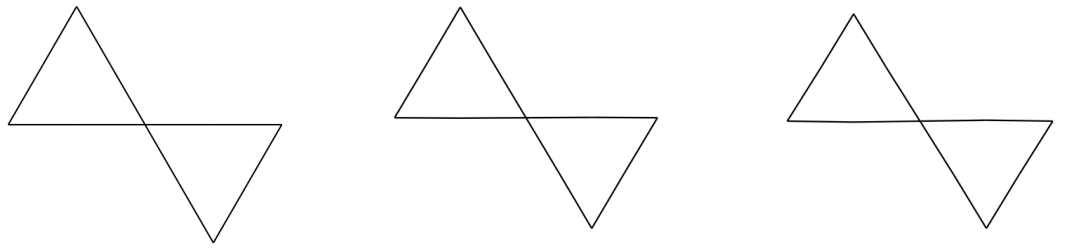

(a) The starting configuration (b) $\varepsilon_{22} = 0.01$ (c) $\varepsilon_{22} = 0.025$

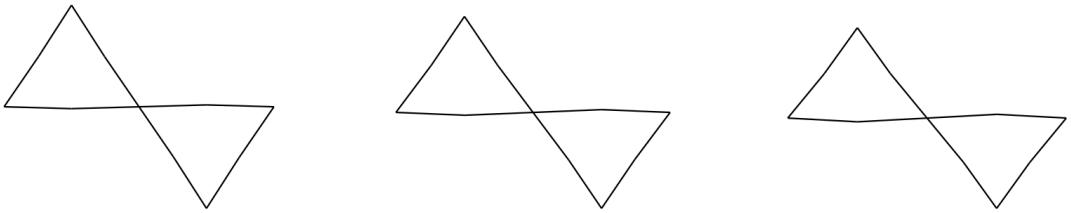

(d) $\varepsilon_{22} = 0.05$ (e) $\varepsilon_{22} = 0.075$ (f) $\varepsilon_{22} = 0.1$

Figure 4.6: Elastic response of a rigidly-jointed Kagome unit cell with relative density $\bar{\rho} = 0.1$ under uniaxial compression. (a) is the undeformed configuration. The response of the lattice in subfigures (b)-(f) shows a stretching-dominated response as predicted in section 3.2. The deformation has been amplified by a factor 2.

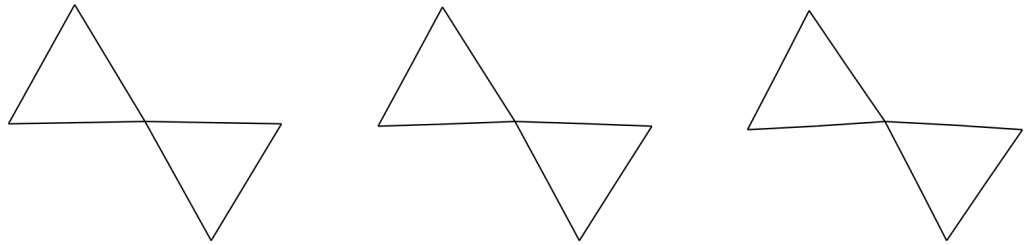

(a) The starting configuration (b) $\varepsilon_{22} = 0.01$ (c) $\varepsilon_{22} = 0.025$

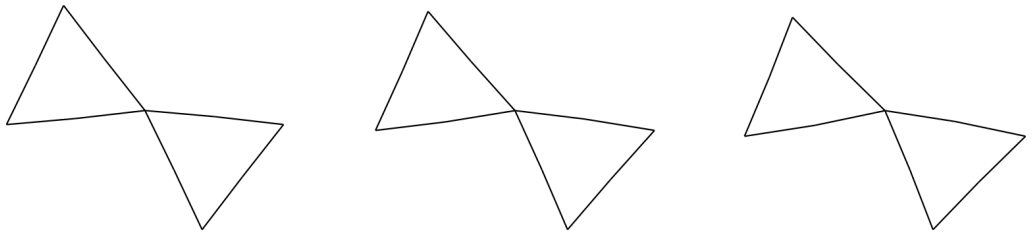

(d) $\varepsilon_{22} = 0.05$ (e) $\varepsilon_{22} = 0.075$ (f) $\varepsilon_{22} = 0.1$

Figure 4.7: Elastic response of a twisted Kagome unit cell, twisted with $\theta = \frac{\pi}{180}$ and $\bar{\rho} = 0.1$ under uniaxial compression.(a) is the undeformed configuration. The response to the uniaxial compression as shown in (b)-(f) shows the elastic deformation is reminiscent to the collapse mechanism of the pin-jointed counterpart described in section 3.3.

4.3.2 Geometrically nonlinear calculations

The same calculations as described in section 4.3.1 will now be repeated while accounting for the geometrically nonlinear finite element analysis. The Young's moduli and Poisson's ratios have been recalculated using the setting in ABAQUS NLgeom ON.

Figure 4.8(a) shows the normalised effective Young's modulus E^* as a function of the relative density $\bar{\rho}$. The same scaling is present in these calculations, where only the welded-jointed Kagome lattice scales linearly with the relative density implying stretching dominated elastic deformation while all the other welded-jointed configurations with a range of twist in their initial configuration scale cubically with the relative density implying bending-dominated deformation. Again comparing figures 4.9 and 4.10, it can be clearly seen that the responses to the applied strain are fundamentally different. The welded-jointed configuration of Kagome gives a stretching-dominated response, whereas all other twisted welded-jointed configurations give a bending-dominated response, as was predicted in section 3.5. A tessellated version of figure 4.10 is given in appendix B, it can be seen that the lattice resembles the collapse motion of the pin-jointed Kagome truss depicted in figure 2.8.

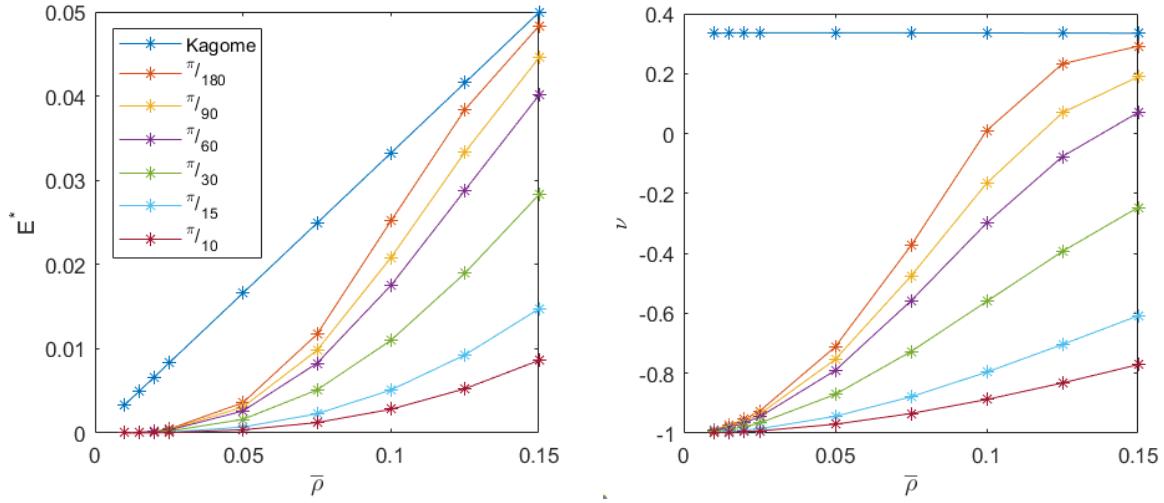

Figure 4.8: (a) The normalised Young's modulus E^* as a function of the relative density $\bar{\rho}$ in the geometrically nonlinear setting. (b) The Poisson's ratio ν as a function of the relative density $\bar{\rho}$ in the geometrically nonlinear setting. In both subfigures the lines represent the different configurations, ranging from no twist to a twist of $\theta = \pi/10$.

A stark difference between the geometrically linear calculations and the geometrically nonlinear calculations is visible especially in the responses of the configurations with a small initial twist. The Young's modulus of these configurations at the lower end of the relative density are no longer able to approach the Young's modulus of the Kagome lattice. The configuration $\theta = \pi/180$ is only able to get within 90% of the original Young's modulus for $\bar{\rho} \geq 0.125$. The reduction in the Young's modulus is more severe than what would be assumed from the linear calculations, especially in the lower range of $\bar{\rho}$. In the higher range of $\bar{\rho}$ the configurations with a small initial twist angles are able to compete again, unlike the configurations with larger initial twist angles, similar to the geometrically linear results.

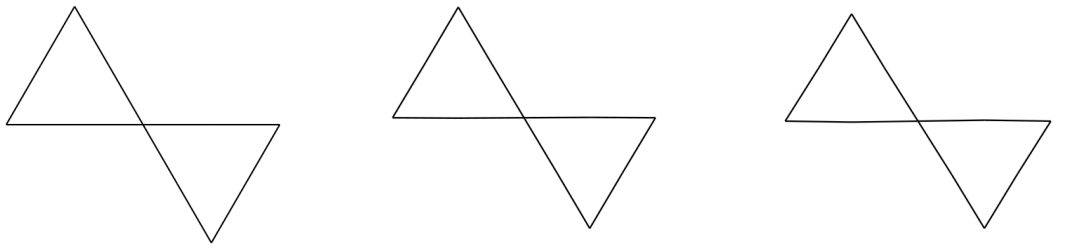

(a) The starting configuration (b) $\varepsilon_{22} = 0.01$ (c) $\varepsilon_{22} = 0.025$

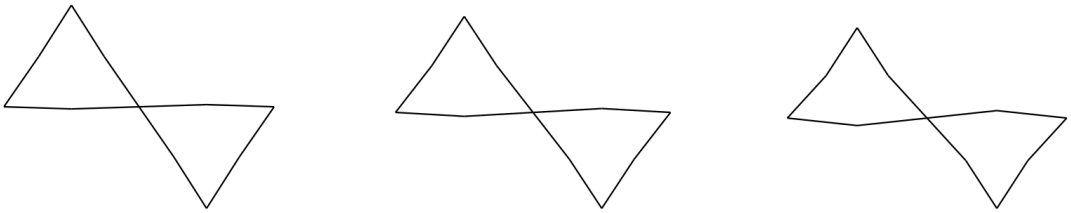

(d) $\varepsilon_{22} = 0.05$ (e) $\varepsilon_{22} = 0.075$ (f) $\varepsilon_{22} = 0.1$

Figure 4.9: Elastic response of a rigidly-jointed Kagome unit cell with relative density $\bar{\rho} = 0.1$ see (a), under uniaxial compression in a nonlinear setting. The response of the lattice in subfigures (b)-(f) shows a stretching-dominated response as predicted in section 3.2. The deformation has been amplified by a factor 2.

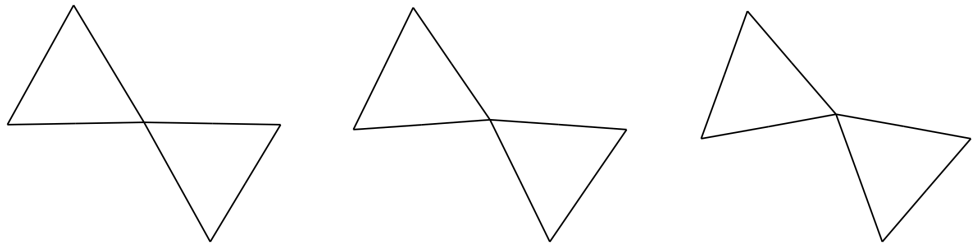

(a) The starting configuration (b) $\varepsilon_{22} = 0.01$ (c) $\varepsilon_{22} = 0.025$

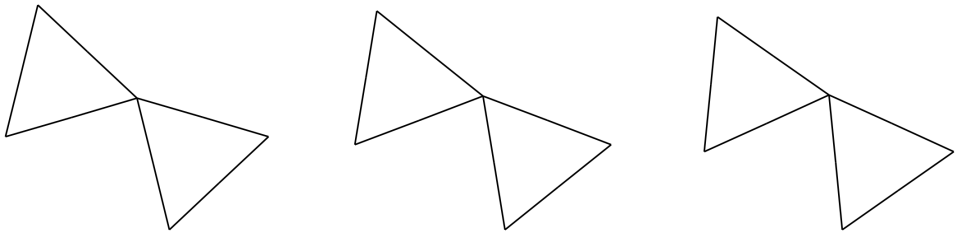

(d) $\varepsilon_{22} = 0.05$ (e) $\varepsilon_{22} = 0.075$ (f) $\varepsilon_{22} = 0.1$

Figure 4.10: Elastic response of a rigidly-jointed Kagome unit cell, that has been twisted by an angle of $\frac{\pi}{180}$ and has a relative density $\bar{\rho} = 0.1$ see (a), under uniaxial compression in a nonlinear setting. The response as shown in (b)-(f) shows the elastic deformation is reminiscent to the collapse mechanism of a pin-jointed counterpart described in section 3.3.

The Poisson's ratio is again independent of the relative density for the Kagome configuration, unlike the twisted configurations. The Poisson's ratio widely varies for the 3 configurations with relatively small twist angles. The twisted configuration $\theta = \pi/180$ almost approaches the same ν as the Kagome configuration. The 3 configurations with relatively large twist angles stay relatively close to the initial ν found at the smallest relative density. This is due to lattices on the lower end of $\bar{\rho}$ rotating further than their denser counterparts, thereby varying the Poisson's ratio more as this is depend on the angle of twist. The stark difference in behaviour of the Poisson's ratio, between the Kagome configuration and the twisted configurations, is due to the fundamentally different responses to applied strain. Both the relative density and the initial angle of twist play a big role in the Poisson's ratio of the twisted configurations.

Interestingly, the Poisson's ratio for most twisted configurations is negative that is the decrease of the initial length H in x_2-direction due to the applied strain is associated with a decrease in the initial length L in x_1-direction of the lattice. It would seem that it is possible to tune the initial Poisson's ratio of the lattice by varying the relative density and the initial twist of the lattice.

Figure 4.11 shows both the decay of the Young's modulus versus the angle of twist θ in the initial configuration and the Poisson's ratio versus the angle of twist θ in the initial configuration for both the geometrically linear and the geometrically nonlinear calculations. The angle of twist is expressed in percentage of the maximum collapse angle $\theta_{\max}$, for this lattice $\theta_{\max} = \pi/3$. The linear results are represented by a solid line while the nonlinear results are shown with a dashed line, the color of the line indicates the relative density. All used relative densities follow a similar decay path for both the Young's modulus and Poisson's ratio. A steep initial decay in the Young's modulus and Poisson's ratio followed by a low plateau for higher angles of twist.

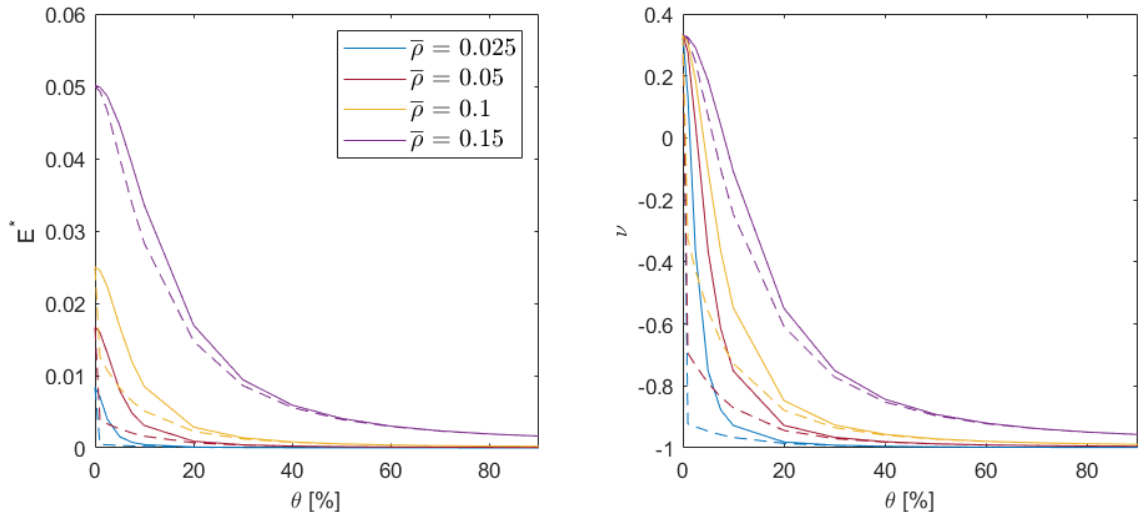

(a) (b)

Figure 4.11: (a) The decay of the Young's modulus as a function of the twist angle θ. (b) The decay of the Poisson's ratio as a function of the twist angle θ. The solid lines represent the geometrically linear calculations while the dashed lines represent the geometrically nonlinear calculations, in both cases the color indicates the relative density. The twist angle is expressed as a percentage of the maximum twist, in the case of Kagome the maximum twist angle $\theta_{\max} = \pi/3$.

4.3.3 Large strain for twisted configurations

In the previous Young's modulus calculations the welded-jointed lattice was subjected to uniaxial compression with $\varepsilon_{22} = 0.01$ and the initial twist of the lattice was varied. As figure 4.8(a) shows the Young's modulus is negatively dependent on the initial twist of the lattice, decreasing as the initial twist increases. Figure 4.10 shows the elastic response of the twisted Kagome lattice for higher strain values. Clearly, the deformation shown is reminiscent of the collapse mechanism of a pin-jointed counterpart as described in section 3.3. Combining the information from both figures would suggest that the stress need to increase the strain does not scale linearly.

A small initial twist of $\theta = \pi/360$ was given to the unit cell in order to stimulate the bending-dominated response. Strain is prescribed in the same fashion as previously described and the stress calculated by ABAQUS is normalised to more easily compare different relative densities. The normalised stress versus strain graph, figure 4.12, for the Kagome lattice shows that increasing the strain first results in a fast increasing stress value but quickly plateaus after this initial increase. The plateau is dependent on the relative density, where the higher this density the more stress is required to reach this plateau. For very large strains the stress will go up again. This will happen when further rotation is no longer possible and the cell walls touch each other, also known as densification.

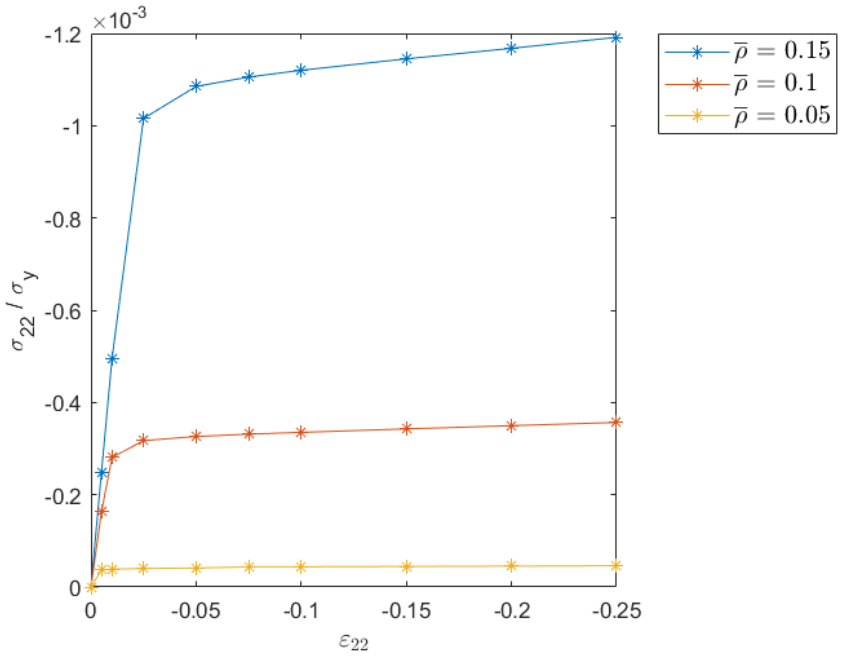

Figure 4.12: Stress in x_2-direction versus the strain in x_2-direction of three different relative densities. An initially steep increase in the stress followed by a plateau in the stress can be observed for all relative densities.

Similarly, comparing the deformation depicted in figure 4.10 and the results in figure 4.8(b) would suggest that the value of the Poisson's ratio decreases if the applied strain value is increased. This negative dependence can be observed in figure 4.13. Therefore the value of the Poisson's ratio depends on the initial twist, the relative density and the applied strain.

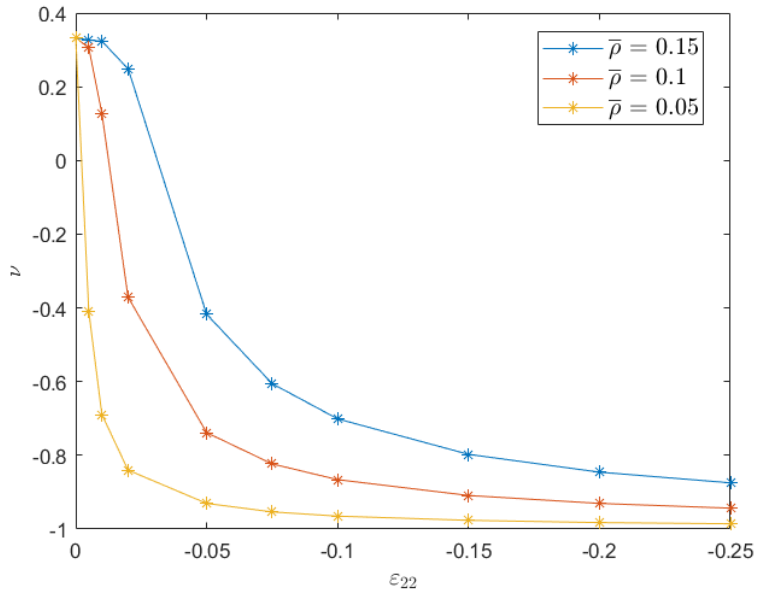

Figure 4.13: The Poisson's ratio versus the strain in x_2-direction for three different relative densities.

4.3.4 Shape-morphing the Kagome lattice

The actuation of the Kagome lattice has been investigated by Nelissen *et al.* [12]. The resulting deformation of the lattice is reminiscent of the collapse mechanism of the pin-jointed truss. This can be clearly seen when comparing subfigures 4.14(a) and 4.14(b), as a single layer with twisted triangles is visible on both the left and right side of the actuator. The layers above and below the actuator remain largely unaffected.

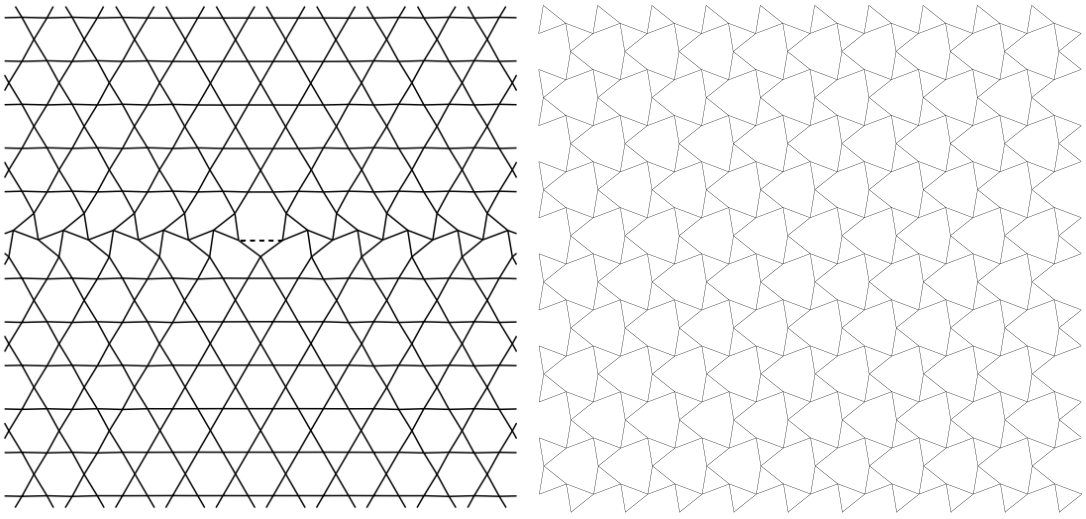

(a) (b)

Figure 4.14: (a) Single member actuation, magnified by a factor 70, of the Kagome lattice reproduced from Nelissen *et al.* [12]. (b) The excited mechanism in the pin-jointed truss. The deformation visible in (a) is reminiscent of the collapse mechanism depicted in (b).

The actuated layer will no longer be stretching-dominated as the actuator is able to introduce twist in the lattice. This introduced twist means that the lattice will respond in a bending-dominated manner

to actuation. Which is favourable as the energy required to actuate a bending-dominated lattice is much lower than a stretching dominated lattice. At the same time this introduced twist also implies that a weak layer is created and the overall lattice will no longer be able to support all macroscopic loads. The property favourable for actuation is at the same time less desirable to the overall macroscopic stiffness of the lattice. Therefore the high passive stiffness will not be maintained during shape-morphing.

4.3.5 Buckling of the bars

It is important to keep in mind that the bars described for the lattice materials are slender beams. Slender beams are notorious for buckling under compressive loads. The critical compressive load can be found by considering the behaviour of an ideal column, which is assumed to be perfectly straight and compressed by a centrally applied load. The straight form is a stable equilibrium if the load P is lower than the critical load. An unstable equilibrium will be reached by increasing the load P, when this happens the column will no longer be able to return to the perfectly straight configuration even when the load is removed [16]. The critical load will be defined as P_{cr}.

According to Timoshenko [16] the critical load is defined as:

$$P_{cr} = \frac{k^2 \pi^2 E_s I}{l^2}, \tag{4.20}$$

where the critical load is a function of the Young's modulus of the solid material E_s, the moment of inertia I, the length of the bars l and k a factor determined by the member end boundary conditions. This load can be rewritten as the critical elastic buckling stress:

$$\sigma_{cr} = \frac{P_{cr}}{A} = \frac{k^2 \pi^2 E_s t w^3}{12 l^2} \frac{1}{wt} = \frac{k^2 \pi^2 E_s}{12} \frac{w^2}{l^2}. \tag{4.21}$$

In order for buckling to occur the critical elastic buckling stress must be smaller or equal than the yield stress or $\sigma_{cr} \leq \sigma_y$. The relative density of the Kagome lattice can be expressed as $\bar{\rho}(w) = \sqrt{3}\frac{w}{l}$. Combining this and equation 4.21 results in the critical relative density:

$$\bar{\rho}_{cr} = \frac{6}{k\pi} \sqrt{\frac{\sigma_{cr}}{E_s}}. \tag{4.22}$$

This minimum relative density should be kept in mind, as it will be important for stretching-dominated structures under compressive loads. For pin-jointed beams, where joint rotation is allowed, $k = 1$. Beams that do not allow for any joint rotation imply k = 2. Rigidly-jointed lattices cannot be described as fully pin-jointed and also do not fully restrict rotations around the joints. The value of k for rigidly-jointed structures should therefore lie somewhere in between the two mentioned values [5].

The most optimistic case can be calculated as $\sigma_{cr} = \sigma_y$, where $\sigma_y = 414$ MPa and the Young's modulus of the aluminium alloy (2014-T6) is $E_s = 70$ GPa. The critical relative density, for $k = 1$, becomes equal to 0.14 or an aspect ratio of 0.081 $\frac{w}{l}$. For $k = 2$, the critical density becomes 0.073 or an aspect ratio of 0.045 $\frac{w}{l}$. Reviewing the results calculated by ABAQUS reveals that the system has negative eigenvalues and therefore buckling has probably occurred. The negative eigenvalues occurred for the Kagome configuration for all values of $\bar{\rho} \leq 0.125$. The negative eigenvalues do not appear for the configurations with an initial twist, as loading these configurations will simply result in further rotation.

4.4 Discussion

Introducing twist to the lattice has an effect on the overall macroscopic stiffness of the lattice. According to the results of the nonlinear matrix method, see chapter 3, a big difference in macroscopic stiffness is expected. This is due to the conversion from the non strain-producing mechanism to a strain-producing mechanism for the pin-jointed truss meaning that a stretching-dominated welded-jointed lattice will now exhibit a bending-dominated response to macroscopic forces, thereby reducing the stiffness. Linear calculations would suggest that the reduction in macroscopic stiffness is not severe for smaller twist angles and for higher relative densities the lattices with introduced twist would even be able to compete with the regular Kagome lattice. In stark contrast, the nonlinear calculations show severe loss of macroscopic stiffness especially at lower relative densities.

It can be seen that the Kagome lattice and the twisted lattice have a fundamentally different response to the prescribed strain load by comparing the different deformed lattices. For the Kagome lattice the bars are being deformed while being loaded. Any configuration that has an initial twist will only further increase the angle of twist instead of deforming the bars themselves. Notice that the response of the regular Kagome lattice to applied strain is very similar in figures 4.6 and 4.9. The same applies to the twisted configuration in figures 4.7 and 4.10. The nonlinear configurations for the twisted lattices simply increase the angle of twist further for the same strain values. And as figure 4.11(a) shows the angle of twist negatively impacts the overall stiffness, the larger the twist angle the lower the stiffness of the lattice. Similarly, the Poisson's ratio decreases as a function of the angle of initial twist, as seen in figure 4.11(b).

As shown in 4.11(b), the variation of the Poisson's ratio depends on both the initial twist of the lattice and the relative density. Figure 4.12 also shows that the value of the Poisson's ratio is dependent on the applied strain. The Poisson's ratios of the twisted structures are only positive for the initial few degrees of twist but quickly become negative, creating auxetic materials. Auxetic materials exhibit mechanical properties that are hardly observed in nonauxetic materials, such as variable permeability, high shear stiffness, and increased energy absorption capabilities [4]. Conveniently, the dependence on the relative density, the initial twist and applied strain also imply that it is possible to tailor the Poisson's ratio to a desired value.

The high passive stiffness of the Kagome lattice, for which the lattice was selected, will not be maintained during actuation. A degradation in the Young's modulus of the lattice is expected due to the introduction of twist by the actuator in a single layer.

Something that does not get picked up by linear calculations is buckling. It is important to consider the possibility of this phenomenon occurring as slender beams are known for buckling. For the regular Kagome lattice buckling is a possibility that should be kept in mind due to the slenderness of the beams. In fact, the results of the nonlinear calculations indicate negative eigenvalues of the system, suggesting that buckling has occurred. The occurrence of buckling does however not have to mean complete loss of macroscopic stiffness. Noteworthy is that the finite element model assumes in-plane deformations and therefore in-plane buckling was assumed. The out-of-plane thickness t is however always smaller than the in-plane width w and it would therefore not be unreasonable to assume that out-of-plane buckling is more likely than in-plane buckling. The occurrence of buckling can also be utilised in the enhancement of energy absorbing materials [18].

Notable is that buckling does not occur for the lattices with an initially twisted configuration as the triangles in the lattice simply increases the angle of twist instead of deforming the bars. This is however not the case for the twisted configurations of the KH lattice, see appendix A. For the twisted KH configurations further twist of the triangles occurs for small strains, but for larger applied strain values the deformation switches from rotation of triangles to deformation of the bars.

5. Discussion

5.1 The Young's modulus of the lattice

The Kagome lattice has been praised for its optimal in-plane stiffness [10], while it is at the same time also capable of shape-morphing. The lattice reacts to macroscopic loads in a stretching-dominated manner, while internal actuation leads to a bending-dominated response. This has led to this micro-architecture being an ideal candidate for shape-morphing, due to its high passive stiffness and low actuation energy requirement. However, most of these studies have only considered the small deformation approximation when describing the macroscopic stiffness of the material and assumed that this stiffness is preserved while shape-morphing. This however does not seem to be the case for the Kagome lattice.

The Kagome truss has a finite collapse mechanism that can be fully described with the use of a single variable angle. The truss also only contains a non strain-producing mechanism in the initial state where no excitation of the mechanism has taken place, giving rise to the favourable high macroscopic stiffness. Actuating the rigidly-jointed lattice introduces deformation reminiscent of the mechanism of the truss. Actuation will therefore immediately cause the loss of the stretching-dominated property. Consequently, the initial configuration has a fundamentally different response to prescribed strain than a configuration where an actuator is deployed. Essentially creating a weak layer in the lattice that will not be able to support all macroscopic loads. The ideal macroscopic stiffness will therefore not be achievable during shape-morphing.

Even before the lattice is actively morphed, the ideal macroscopic stiffness might not be achievable. Only a perfect lattice will be able to achieve the optimal macroscopic stiffness. It is not possible to manufacture a perfect lattice in practise. Small defects, like twists in the unactuated lattice, will therefore result in a lower passive stiffness than theoretically predicted. The weak layers created by actuation might therefore not induce a dramatic loss of passive stiffness, compared to the stiffness found in the initial state.

This degradation in passive stiffness is also observable in other lattice micro-architectures such as the KH lattice, see appendix A. This pin-jointed equivalent truss like the Kagome truss has a non strain-producing mechanism in its initial configuration that is converted into a strain-producing mechanism the instant that the mechanism is excited. Similarly even the small angles of twist will severely impact the macroscopic stiffness.

5.2 The Poisson's ratio of the lattice

An interesting property appears when an angle of twist is introduced in the Kagome lattice. The Poisson's ratio varies depending on angle of twist, the relative density of the lattice and the applied strain.

The Kagome configuration remains largely unaffected by the changes in the relative density when it comes to the Poisson's ratio. This is not the case for the initially twisted configurations. The twisted configurations show large variations in Poisson's ratio, especially for the configurations that only have relatively small twist angles such as $\pi/180$, when the relative density is varied. This variation in Poisson's ratios is due to the fact that when strain is applied the configurations with a small angle of twist will continue to rotate, instead of deforming the beams like the Kagome configuration does. If the angle of twist is large enough or if the relative density is small enough the Poisson's ratio can even be negative, resulting in auxetic materials. This is a rare property for isotropic materials. This property is not unique to the Kagome lattice, as it can also be observed when introducing twist to the KH lattice, see appendix A.

This would also imply that it is possible to tailor the Poisson's ratio, by means of introducing twist to the triangles, to the desired application.

6. Conclusion

6.1 General conclusion

Finally the question, what is the effect of deformation in the form of introduced twist of the lattice on the overall macroscopic properties, such as the Young's modulus and the Poisson's ratio?, can be answered for the Kagome lattice.

Firstly, according to the matrix method, triggering a mechanism for the pin-jointed Kagome truss will result in instantaneous loss of the stretching-dominated property in the rigidly-jointed lattice counterpart. This is due to the non strain-producing mechanism being converted into a strain-producing mechanism. At no configuration other than the initial configuration and the fully collapsed configuration was the non strain-producing mechanism found again. Numerical experiments confirm that the elastic response of the rigidly-jointed lattice fundamentally differs between the Kagome configuration and the twisted configurations. Therefore the attractive properties the rigidly-jointed material was selected for are instantly lost after introducing any twist in the lattice by for example actuation.

Secondly, it is possible to tune the initial Poisson's ratio of the lattice to fit specific applications. This can be done by adjusting the initial angle of twist, the relative density of the lattice or adjusting the applied strain. Poisson's ratios between 0.33 and approximately -1 are possible to achieve, by simply adjusting the previously mentioned variables.

6.2 Future work

The presented research in this thesis can be further improved and expanded on, a few suggestions for further research are presented here.

- It has been shown in this thesis that the Kagome and KH trusses instantly convert their non strain-producing mechanism to a strain-producing mechanism when their mechanisms are excited. This does not imply that this is a property of all lattice micro-architectures share. A lattice micro-architecture could perhaps be designed that can preserve a non strain-producing mechanism or that obtains a non strain-producing mechanism during its collapse.

- The Poisson's ratio for both discussed lattices varied widely, many configurations even exhibit auxetic behaviour. Application and a more in-depth analysis of this phenomenon might be of interest for this field of research.

- Pronk *et al.* [15] formulated several design criteria for lattices suitable for shape-morphing. His successor Nelissen *et al.* [12] has shown that these selection criteria are both over restrictive and insufficient simultaneously. Improving further upon these criteria could result in even more micro-architectures capable of competing with the Kagome lattice.

A. Kagome with concentric hexagons

A finite mechanism can be found for the KH truss as will be described in this part. Unlike the Kagome truss no convenient collapse motion can be found in the literature for the KH truss, it has yet to be identified. The undeformed truss will first be analysed with the matrix method so that a linearised representation of a non strain-producing and hopefully finite mechanism can be constructed. This representation will be used to make an educated guess on the movements that will come afterwards, thus deciphering the full motion.

For convenience a similar unit cell as the one described by Nelisson *et al.* (2019) [12] will be used for this analysis, slightly changed to include nodes outside of the unit cell, figure A.1. Again the joints are indicated with Arabic numbers and the beams are indicated by Roman numerals. Not all bars are the same length for this truss, the short bars will have a length L and the longer bars have a length of $\sqrt{3}$L. Nodes 1 to 9 are the master nodes while nodes 10 to 14 are the slave nodes connected to the beams that cross the unit cell boundaries. These slave nodes are used for the augmentation of the analysis.

A.1 Linear analysis

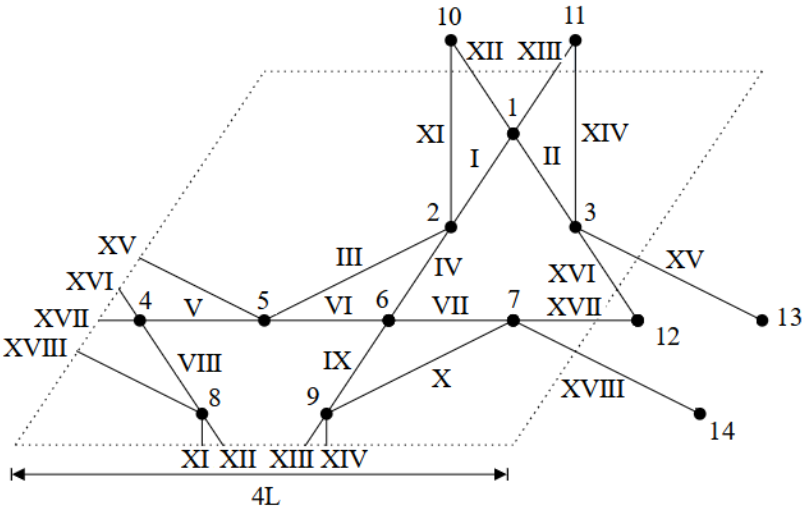

Figure A.1: The KH unit cell used for the pin-jointed matrix analysis. Node numbers are indicated with Arabic numbers and bar numbers are indicated with Roman numerals.

The compatibility matrix $\boldsymbol{B}$ (9 x 9) and the displacement vector $\boldsymbol{d}$ (9 x 1) can be set up, using the undeformed truss. These will be used as the starting point for the augmentation of the analysis. Firstly, the extra terms for the displacement vector, found with the characteristic unit cell lengths of KH, will be defined as:

$$\begin{aligned} d_{11} &= 4\mathrm{L}\epsilon_{11}, \\ d_{12} &= 4\mathrm{L}\epsilon_{12}, \\ d_{22} &= 2\sqrt{3}\mathrm{L}\epsilon_{22}. \end{aligned} \tag{A.1}$$

Expanding the displacement vector to be a (12 x 1) vector. Secondly, the terms described in A.1 can be used to augment the kinematic relations.

$$
\begin{aligned}
d_1^{(10)} &= d_1^{(8)} + \frac{1}{2}d_{11} + \frac{\sqrt{3}}{2}d_{12}, & d_2^{(10)} &= d_2^{(8)} + \frac{1}{2}d_{12} + d_{22},\\
d_1^{(11)} &= d_1^{(9)} + \frac{1}{2}d_{11} + \frac{\sqrt{3}}{2}d_{12}, & d_2^{(11)} &= d_2^{(9)} + \frac{1}{2}d_{12} + d_{22},\\
d_1^{(12)} &= d_1^{(4)} + d_{11}, & d_2^{(12)} &= d_2^{(4)} + d_{12},\\
d_1^{(13)} &= d_1^{(5)} + d_{11}, & d_2^{(13)} &= d_2^{(5)} + d_{12},\\
d_1^{(14)} &= d_1^{(8)} + d_{11}, & d_2^{(14)} &= d_2^{(8)} + d_{12}.
\end{aligned}
\tag{A.2}
$$

Resulting in the following augmented kinematic matrix $\boldsymbol{B}_{\text{aug}}$ (18 x 21):

$$
\begin{bmatrix}
\frac{1}{2} & \frac{\sqrt{3}}{2} & -\frac{1}{2} & -\frac{\sqrt{3}}{2} & 0 & 0 & 0 & 0 & 0 & 0 & 0 & 0 & 0 & 0 & 0 & 0 & 0 & 0 & 0 & 0 & 0\\
-\frac{1}{2} & \frac{\sqrt{3}}{2} & 0 & 0 & \frac{1}{2} & -\frac{\sqrt{3}}{2} & 0 & 0 & 0 & 0 & 0 & 0 & 0 & 0 & 0 & 0 & 0 & 0 & 0 & 0 & 0\\
0 & 0 & \frac{\sqrt{3}}{2} & \frac{1}{2} & 0 & 0 & 0 & 0 & -\frac{\sqrt{3}}{2} & -\frac{1}{2} & 0 & 0 & 0 & 0 & 0 & 0 & 0 & 0 & 0 & 0 & 0\\
0 & 0 & \frac{1}{2} & \frac{\sqrt{3}}{2} & 0 & 0 & 0 & 0 & 0 & 0 & -\frac{1}{2} & -\frac{\sqrt{3}}{2} & 0 & 0 & 0 & 0 & 0 & 0 & 0 & 0 & 0\\
0 & 0 & 0 & 0 & 0 & 0 & -1 & 0 & 1 & 0 & 0 & 0 & 0 & 0 & 0 & 0 & 0 & 0 & 0 & 0 & 0\\
0 & 0 & 0 & 0 & 0 & 0 & 0 & 0 & -1 & 0 & 1 & 0 & 0 & 0 & 0 & 0 & 0 & 0 & 0 & 0 & 0\\
0 & 0 & 0 & 0 & 0 & 0 & 0 & 0 & 0 & 0 & -1 & 0 & 1 & 0 & 0 & 0 & 0 & 0 & 0 & 0 & 0\\
0 & 0 & 0 & 0 & 0 & 0 & -\frac{1}{2} & \frac{\sqrt{3}}{2} & 0 & 0 & 0 & 0 & 0 & 0 & \frac{1}{2} & -\frac{\sqrt{3}}{2} & 0 & 0 & 0 & 0 & 0\\
0 & 0 & 0 & 0 & 0 & 0 & 0 & 0 & 0 & 0 & \frac{1}{2} & \frac{\sqrt{3}}{2} & 0 & 0 & 0 & 0 & -\frac{1}{2} & -\frac{\sqrt{3}}{2} & 0 & 0 & 0\\
0 & 0 & 0 & 0 & 0 & 0 & 0 & 0 & 0 & 0 & 0 & 0 & \frac{\sqrt{3}}{2} & \frac{1}{2} & 0 & 0 & -\frac{\sqrt{3}}{2} & -\frac{1}{2} & 0 & 0 & 0\\
0 & 0 & 0 & -1 & 0 & 0 & 0 & 0 & 0 & 0 & 0 & 0 & 0 & 0 & 0 & 0 & 0 & 1 & 0 & \frac{1}{2} & 1\\
\frac{1}{2} & -\frac{\sqrt{3}}{2} & 0 & 0 & 0 & 0 & 0 & 0 & 0 & 0 & 0 & 0 & 0 & 0 & -\frac{1}{2} & \frac{\sqrt{3}}{2} & 0 & 0 & -\frac{1}{4} & 0 & \frac{\sqrt{3}}{2}\\
-\frac{1}{2} & -\frac{\sqrt{3}}{2} & 0 & 0 & 0 & 0 & 0 & 0 & 0 & 0 & 0 & 0 & 0 & 0 & 0 & 0 & \frac{1}{2} & \frac{\sqrt{3}}{2} & \frac{1}{4} & \frac{\sqrt{3}}{2} & \frac{\sqrt{3}}{2}\\
0 & 0 & 0 & 0 & 0 & -1 & 0 & 0 & 0 & 0 & 0 & 0 & 0 & 0 & 0 & 0 & 0 & 1 & 0 & \frac{1}{2} & 1\\
0 & 0 & 0 & 0 & -\frac{\sqrt{3}}{2} & \frac{1}{2} & 0 & 0 & \frac{\sqrt{3}}{2} & -\frac{1}{2} & 0 & 0 & 0 & 0 & 0 & 0 & 0 & 0 & \frac{\sqrt{3}}{2} & -\frac{1}{2} & 0\\
0 & 0 & 0 & 0 & -\frac{1}{2} & \frac{\sqrt{3}}{2} & \frac{1}{2} & -\frac{\sqrt{3}}{2} & 0 & 0 & 0 & 0 & 0 & 0 & 0 & 0 & 0 & 0 & \frac{1}{2} & -\frac{\sqrt{3}}{2} & 0\\
0 & 0 & 0 & 0 & 0 & 0 & 1 & 0 & 0 & 0 & 0 & 0 & -1 & 0 & 0 & 0 & 0 & 0 & 1 & 0 & 0\\
0 & 0 & 0 & 0 & 0 & 0 & 0 & 0 & 0 & 0 & 0 & 0 & -\frac{\sqrt{3}}{2} & \frac{1}{2} & \frac{\sqrt{3}}{2} & -\frac{1}{2} & 0 & 0 & \frac{\sqrt{3}}{2} & -\frac{1}{2} & 0
\end{bmatrix}
\tag{A.3}
$$

Lastly, the nullspace of the augmented matrix is calculated.

$$
\boldsymbol{N}(\boldsymbol{B}_{\text{aug}}) = \begin{bmatrix}
1 & 0 & 1 & 0 & 1 & 0 & 1 & 0 & 1 & 0 & 1 & 0 & 1 & 0 & 1 & 0 & 1 & 0 & 0 & 0 & 0\\
0 & 1 & 0 & 1 & 0 & 1 & 0 & 1 & 0 & 1 & 0 & 1 & 0 & 1 & 0 & 1 & 0 & 1 & 0 & 0 & 0\\
\frac{1}{2} & -\frac{\sqrt{3}}{6} & 0 & 0 & 1 & 0 & \frac{1}{2} & -\frac{\sqrt{3}}{6} & \frac{1}{2} & -\frac{\sqrt{3}}{6} & \frac{1}{2} & -\frac{\sqrt{3}}{6} & \frac{1}{2} & -\frac{\sqrt{3}}{2} & 1 & 0 & 0 & 0 & 0 & 0 & 0
\end{bmatrix}^T
\tag{A.4}
$$

The first two columns of the nullspace contain the rigid body translations in the x_1- and x_2-directions. The third column describes a possible finite non strain-producing collapse mechanism, since the last three rows only contain zeros. A linearised representation of the mechanism is plotted in figure A.2. The motion can be characterised by the expansion of what used to be the triangle formed by node 1 & 6 & 12 and the collapse of what used to be the triangle formed by node 4 & 6 & 1. The hexagons, which can be seen a the tessellated version of the unit cell, have started to shift into a triangular shape.

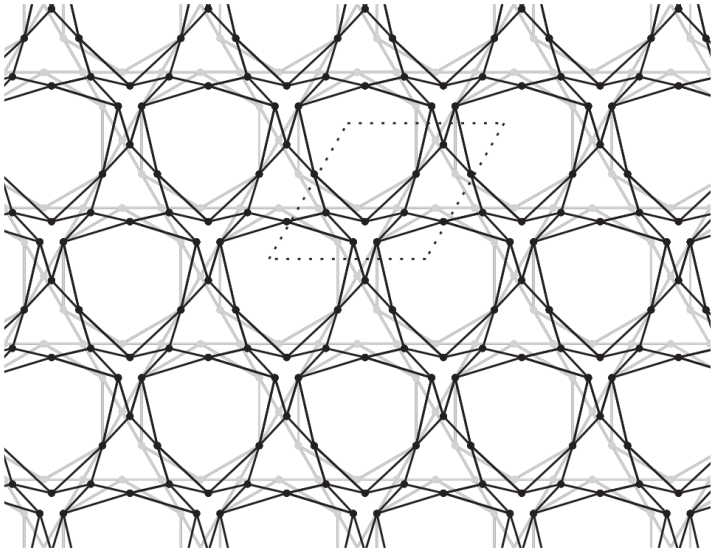

Figure A.2: A linearised representation of the possibly finite non strain-producing mechanism found in equation A.4 accoding to Nelissen *et al.* [12]. The gray structure is the undeformed begin position, while the black structure represents the deformed state after the mechanism is excited.

A.2 Finite mechanism

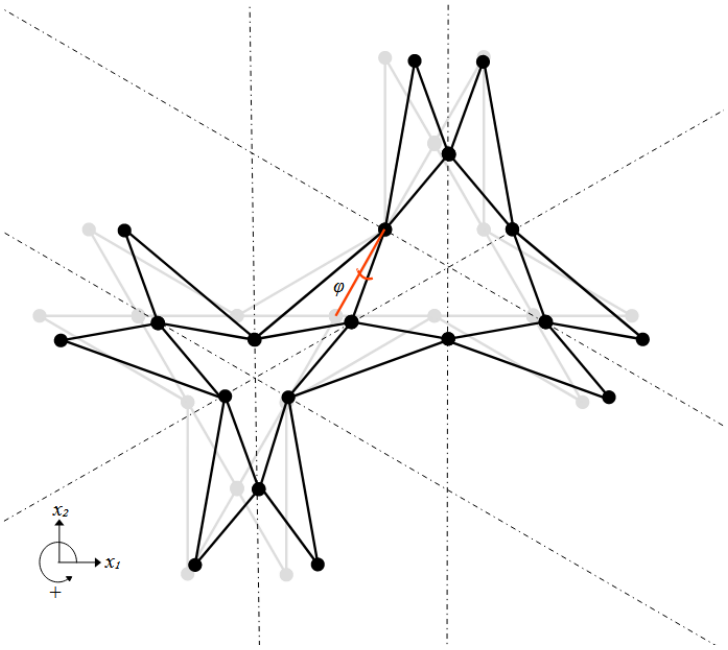

Figure A.3: The dash-dotted lines form symmetry lines. Since the triangles can be treated as rigid bodies, angle ϕ can be used to accurately prescribe the position of the nodes relative to each other while preserving the strut lengths.

Similar to the Kagome truss, a single deformation angle can be identified to describe the full collapse motion, confirming that this mechanism is indeed a finite mechanism. Figure A.3 shows the the symmetry lines that are implied by the linear representation. The threefold symmetry also implies that the welded-jointed lattice will behave in an isotropic fashion to macroscopic loads. The full motion can be constructed by simply mirroring the movement of a single triangle rotated by angle ϕ .The completed

motion is illustrated by four subfigures in figure A.4.

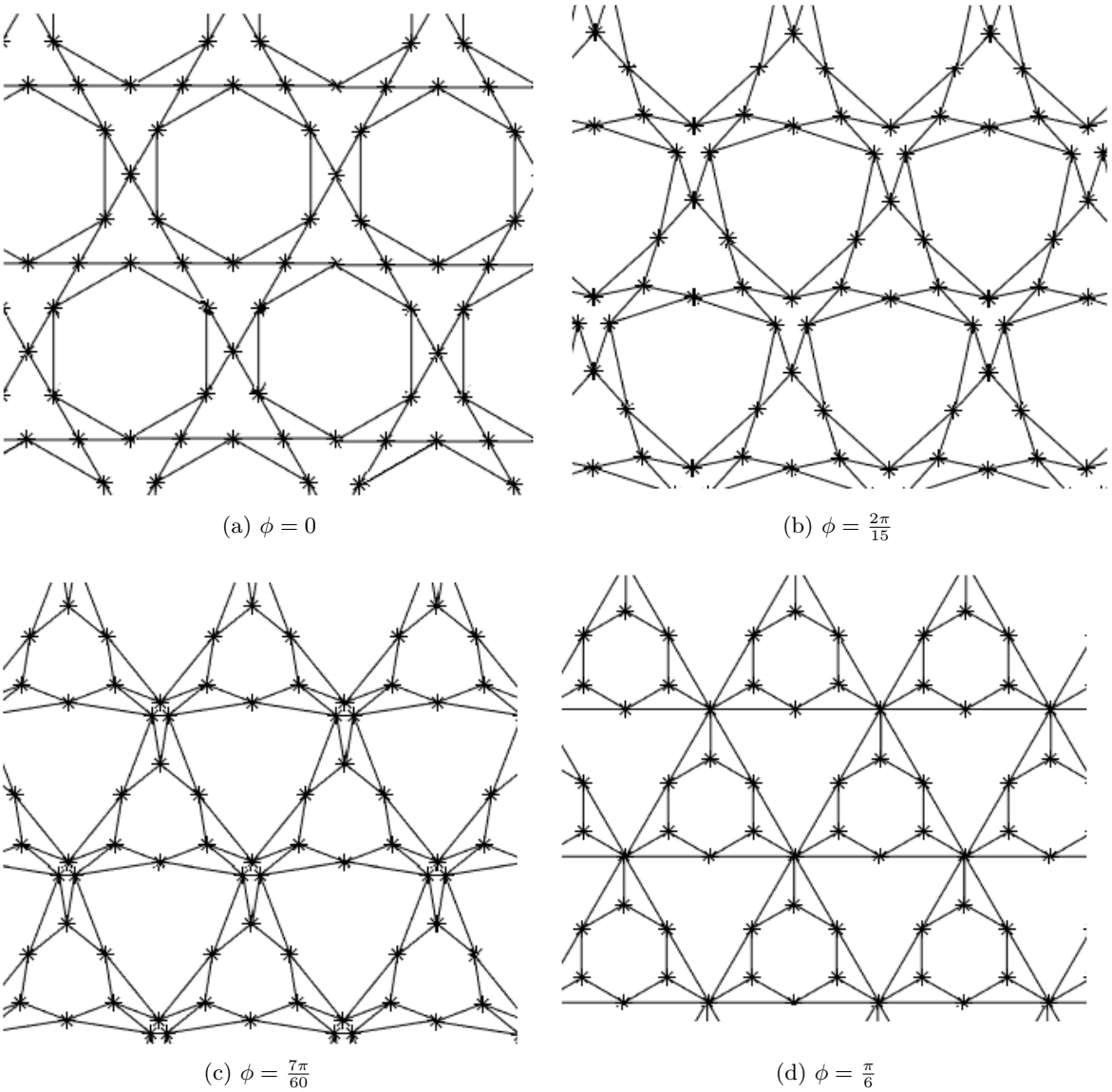

(a) $\phi = 0$ (b) $\phi = \frac{2\pi}{15}$

(c) $\phi = \frac{7\pi}{60}$ (d) $\phi = \frac{\pi}{6}$

Figure A.4: The collapse motion of a tessellated KH truss captured in 4 steps. Subfigure (a) is the starting point and therefore the undeformed configuration. Subfigures (b) and (c) show the intermediate steps before reaching the full collapse as shown in subfigure (d).

A.3 Nonlinear analysis

The matrix method will now redefined in such a way that the augmented kinematic matrix is dependent on the collapse angle ϕ. As this is very similar to chapter 3 the steps to do this will not be given. The augmented matrix has been split into 2 parts due to the size of the matrix. Therefore $\boldsymbol{B}_{\text{aug}} = [\boldsymbol{B}|\boldsymbol{C}]$ with $\boldsymbol{B}$ = A.5 and $\boldsymbol{C}$ = A.6.

$$
\begin{bmatrix}
\cos(\phi-\frac{\pi}{3}) & -\sin(\phi-\frac{\pi}{3}) & -\cos(\phi-\frac{\pi}{3}) & \sin(\phi-\frac{\pi}{3}) & 0 & 0 & 0 & 0 & 0 & 0 & 0 & 0 & 0 & 0 & 0 & 0 \\
-\cos(\phi-\frac{\pi}{3}) & -\sin(\phi-\frac{\pi}{3}) & 0 & 0 & \cos(\phi-\frac{\pi}{3}) & \sin(\phi-\frac{\pi}{3}) & 0 & 0 & 0 & 0 & 0 & 0 & 0 & 0 & 0 & 0 \\
0 & 0 & \cos(\phi+\frac{\pi}{6}) & \cos(\phi-\frac{\pi}{3}) & 0 & 0 & 0 & 0 & -\cos(\phi+\frac{\pi}{6}) & -\cos(\phi-\frac{\pi}{3}) & 0 & 0 & 0 & 0 & 0 & 0 \\
0 & 0 & \cos(\phi+\frac{\pi}{3}) & \sin(\phi+\frac{\pi}{3}) & 0 & 0 & 0 & 0 & 0 & -\cos(\phi+\frac{\pi}{3}) & -\sin(\phi+\frac{\pi}{3}) & 0 & 0 & 0 & 0 & 0 \\
0 & 0 & 0 & 0 & 0 & 0 & -\cos(\phi) & \sin(\phi) & \cos(\phi) & -\sin(\phi) & 0 & 0 & 0 & 0 & 0 & 0 \\
0 & 0 & 0 & 0 & 0 & 0 & 0 & 0 & -\cos(\phi) & -\sin(\phi) & \cos(\phi) & \sin(\phi) & 0 & 0 & 0 & 0 \\
0 & 0 & 0 & 0 & 0 & 0 & 0 & 0 & 0 & -\cos(\phi) & \sin(\phi) & \cos(\phi) & 0 & 0 & 0 & 0 \\
0 & 0 & 0 & 0 & 0 & 0 & -\cos(\phi-\frac{\pi}{3}) & -\sin(\phi-\frac{\pi}{3}) & 0 & 0 & 0 & 0 & \cos(\phi-\frac{\pi}{3}) & \sin(\phi-\frac{\pi}{3}) & 0 & 0 \\
0 & 0 & 0 & 0 & 0 & 0 & 0 & 0 & \sin(\phi+\frac{\pi}{6}) & \cos(\phi+\frac{\pi}{6}) & 0 & 0 & 0 & 0 & -\sin(\phi+\frac{\pi}{6}) & -\cos(\phi+\frac{\pi}{6}) \\
0 & 0 & 0 & 0 & 0 & 0 & 0 & 0 & 0 & 0 & \sin(\phi+\frac{\pi}{3}) & \cos(\phi+\frac{\pi}{3}) & 0 & 0 & -\sin(\phi+\frac{\pi}{3}) & -\cos(\phi+\frac{\pi}{3}) \\
0 & 0 & -\sin(\phi) & -\cos(\phi) & 0 & 0 & 0 & 0 & 0 & 0 & 0 & \sin(\phi) & \cos(\phi) & 0 & 0 & 0 \\
\cos(\phi+\frac{\pi}{3}) & -\sin(\phi+\frac{\pi}{3}) & 0 & 0 & 0 & 0 & 0 & 0 & 0 & 0 & 0 & -\cos(\phi+\frac{\pi}{3}) & \sin(\phi+\frac{\pi}{3}) & 0 & 0 & 0 \\
-\cos(\phi+\frac{\pi}{3}) & -\sin(\phi+\frac{\pi}{3}) & 0 & 0 & 0 & 0 & 0 & 0 & 0 & 0 & 0 & 0 & 0 & \cos(\phi+\frac{\pi}{3}) & \sin(\phi+\frac{\pi}{3}) & 0 \\
0 & 0 & 0 & 0 & \sin(\phi) & -\cos(\phi) & 0 & 0 & 0 & 0 & 0 & 0 & 0 & -\sin(\phi) & \cos(\phi) & 0 \\
0 & 0 & 0 & 0 & -\cos(\phi+\frac{\pi}{6}) & \cos(\phi-\frac{\pi}{3}) & 0 & 0 & \cos(\phi+\frac{\pi}{6}) & -\cos(\phi-\frac{\pi}{3}) & 0 & 0 & 0 & 0 & 0 & 0 \\
0 & 0 & 0 & 0 & -\cos(\phi+\frac{\pi}{3}) & \sin(\phi+\frac{\pi}{3}) & \cos(\phi+\frac{\pi}{3}) & -\sin(\phi+\frac{\pi}{3}) & 0 & 0 & 0 & 0 & 0 & 0 & 0 & 0 \\
0 & 0 & 0 & 0 & 0 & 0 & \cos(\phi) & \sin(\phi) & 0 & 0 & 0 & -\cos(\phi) & -\sin(\phi) & 0 & 0 & 0 \\
0 & 0 & 0 & 0 & 0 & 0 & 0 & 0 & 0 & 0 & 0 & -\sin(\phi+\frac{\pi}{3}) & \cos(\phi+\frac{\pi}{3}) & \sin(\phi+\frac{\pi}{3}) & -\cos(\phi+\frac{\pi}{3}) & 0
\end{bmatrix}
\tag{A.5}
$$

$$
\begin{bmatrix}
0 & 0 & 0 \\
0 & 0 & 0 \\
0 & 0 & 0 \\
0 & 0 & 0 \\
0 & 0 & 0 \\
0 & 0 & 0 \\
0 & 0 & 0 \\
0 & 0 & 0 \\
0 & 0 & 0 \\
\frac{\sin(2\phi)}{4|\cos(\phi)|} & \frac{\cos(2\phi-\frac{\pi}{3})+\frac{1}{2}}{2|\cos(\phi)|} & \frac{\cos(\phi)^2}{|\cos(\phi)|} \\
-\frac{\cos(2\phi+\frac{\pi}{3})+\frac{1}{2}}{4|\cos(\phi)|} & \frac{\sin(2\phi)}{2|\cos(\phi)|} & \frac{\sin(\phi+\frac{\pi}{3})+\frac{\sqrt{3}}{2}}{2|\cos(\phi)|} \\
\frac{\cos(2\phi+\frac{\pi}{3})+\frac{1}{2}}{4|\cos(\phi)|} & \frac{\cos(2\phi+\frac{\pi}{6})+\frac{\sqrt{3}}{2}}{2|\cos(\phi)|} & \frac{\sin(\phi+\frac{\pi}{3})+\frac{\sqrt{3}}{2}}{2|\cos(\phi)|} \\
-\frac{\sin(2\phi)}{4|\cos(\phi)|} & \frac{\cos(2\phi-\frac{\pi}{3})+\frac{1}{2}}{2|\cos(\phi)|} & \frac{\cos(\phi)^2}{|\cos(\phi)|} \\
\frac{\cos(2\phi+\frac{\pi}{6})+\frac{\sqrt{3}}{2}}{2|\cos(\phi)|} & -\frac{\cos(2\phi-\frac{\pi}{3})+\frac{1}{2}}{2|\cos(\phi)|} & 0 \\
\frac{\cos(2\phi+\frac{\pi}{3})+\frac{1}{2}}{2|\cos(\phi)|} & -\frac{\sin(2\phi+\frac{\pi}{3})+\frac{\sqrt{3}}{2}}{2|\cos(\phi)|} & 0 \\
\frac{\cos(\phi)^2}{|\cos(\phi)|} & \frac{\sin(2\phi)}{2|\cos(\phi)|} & 0 \\
\frac{\sin(2\phi+\frac{\pi}{3})+\frac{\sqrt{3}}{2}}{2|\cos(\phi)|} & -\frac{\cos(2\phi+\frac{\pi}{3})+\frac{1}{2}}{2|\cos(\phi)|} & 0
\end{bmatrix}
\tag{A.6}
$$

Now again only three different situations are found. The undeformed configuration has a non strain-producing mechanism. The intermediate configurations all contain one strain-producing mechanism, similar to the fully collapsed truss under a non compressive load. Similar to the Kagome truss, KH immidiately converts the non strain-producing mechanism into a strain-producing mechanism. This can be found by substituting ϕ with the values $\phi = 0$ and $-\frac{\pi}{6} < \phi < 0 \cup 0 < \phi < \frac{\pi}{6}$. To investigate the nullspace of full collapse under uni- or biaxial compression will require the reformulation of the unit cell.

Noteworthy is that the steps between the initial configuration and the full collapse show the exact same unit cell deformations independent of the collapse angle ϕ, see the nullspace given in equation A.7. This deformation is the same as the deformation found in chapter 3 for the Kagome truss.

$$
\begin{bmatrix}
1 & 0 & -\frac{\cos(\phi)^2-\sqrt{3}\cos(\phi)\sin(\phi)}{4|\cos(\phi)\sin(\phi)|} \\
0 & 1 & \frac{\cos(\phi)(9\sin(\phi)+\sqrt{3}\cos(\phi))}{12|\cos(\phi)\sin(\phi)|} \\
1 & 0 & \frac{\sqrt{3}\cos(\phi)}{6|\cos(\phi)|} \\
0 & 1 & \frac{\cos(\phi)}{2|\cos(\phi)|} \\
1 & 0 & -\frac{\cos(\phi)(3\cos(\phi)-2\sqrt{3}\sin(\phi))}{6|\cos(\phi)\sin(\phi)|} \\
0 & 1 & \frac{\cos(\phi)}{2|\cos(\phi)|} \\
1 & 0 & -\frac{\cos(\phi)^2-\sqrt{3}\cos(\phi)\sin(\phi)}{4|\cos(\phi)\sin(\phi)|} \\
0 & 1 & \frac{\sqrt{3}\cos(\phi)^2+\sqrt{3}\sin(\phi)cos(\phi)}{12|\cos(\phi)\sin(\phi)|} \\
1 & 0 & -\frac{3\cos(\phi)^2+\sqrt{3}\cos(\phi)\sin(\phi)}{12|\cos(\phi)\sin(\phi)|} \\
0 & 1 & \frac{\sqrt{3}\cos(\phi)^2+\sin(\phi)\cos(\phi)}{4|\cos(\phi)sin(\phi)|} \\
1 & 0 & -\frac{3\cos(\phi)^2-\sqrt{3}\cos(\phi)\sin(\phi)}{12|\cos(\phi)\sin(\phi)|} \\
0 & 1 & \frac{\sqrt{3}\cos(\phi)^2+\sqrt{3}\sin(\phi)\cos(\phi)}{12|\cos(\phi)\sin(\phi)|} \\
1 & 0 & -\frac{\cos(\phi)^2-\sqrt{3}\cos(\phi)\sin(\phi)}{4|\cos(\phi)\sin(\phi)|} \\
0 & 1 & \frac{\sqrt{3}\cos(\phi)^2+\sin(\phi)\cos(\phi)}{4|\cos(\phi)\sin(\phi)|} \\
1 & 0 & -\frac{3\cos(\phi)^2+\sqrt{3}\cos(\phi)\sin(\phi)}{6|\cos(\phi)\sin(\phi)|} \\
0 & 1 & 0 \\
1 & 0 & 0 \\
0 & 1 & 0 \\
0 & 0 & \frac{2\sqrt{3}}{3} \\
0 & 0 & 0 \\
0 & 0 & 1
\end{bmatrix}
\tag{A.7}
$$

A.4 Results

	KH $\phi = 0$	$-\frac{\pi}{6} < \phi < 0 \cup 0 < \phi < \frac{\pi}{6}$
Non strain-producing mechanisms	3	2
Strain-producing mechanisms	0	1
Deformation behavior of a welded-jointed equivalent lattice	Stretching-dominated	Bending-dominated

A.5 Macroscopic properties

The macroscopic properties of a deforming KH lattice will be calculated in this section. The material properties of the bars are representative of aluminium and have linear elastic behavior. The bars are assumed to have a rectangular cross-section, where the out-of-plane thickness t is a constant and the in-plane thickness w will be varied in order to systematically vary relative densities $\bar{\rho}$, similar to section 4.2.

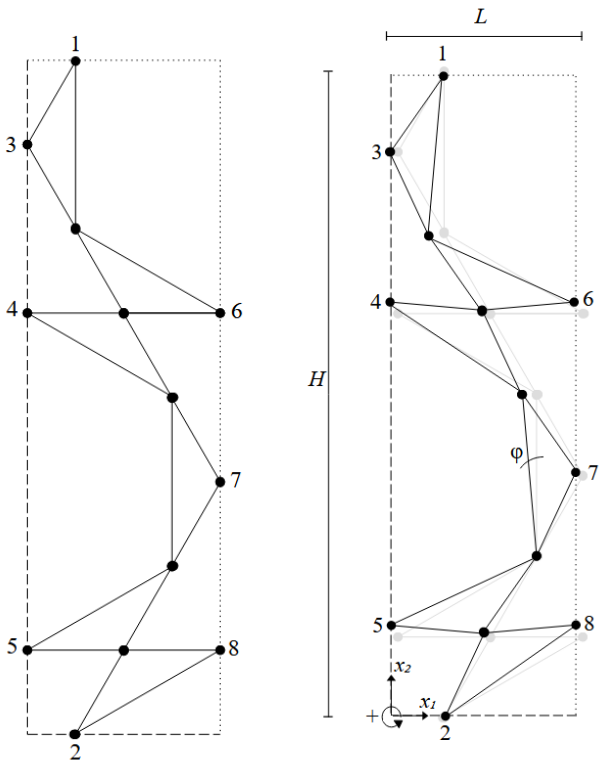

Figure A.5: (a) The initial unit cell used for the FEM analysis of KH (b) The excited states of KH related to the initial configuration

The unit cell used for this analysis is given in figure A.5, where angle ϕ denotes the degree of collapse of the structure. The dashed lines represent the lines of symmetry, while the dotted lines represent the periodic boundaries. Uniaxial strain ε_{11}^* will be applied to the unit cell. The nodes lying on the boundary of the unit cell must adhere to the following conditions:

Node 1 & 2:	$u_1^{(1)} = u_1^{(2)},$	$u_2^{(1)} = -u_2^{(2)},$	$\phi^{(1)} = \phi^{(2)}.$
Node 3:	$u_1^{(3)} = 0,$		$\phi^{(3)} = 0.$
Node 4:	$u_1^{(4)} = 0,$		$\phi^{(4)} = 0.$
Node 5:	$u_1^{(5)} = 0,$		$\phi^{(5)} = 0.$
Node 6:	$u_1^{(6)} = u_1^{(8)},$		$\phi^{(6)} = 0.$
Node 7:	$u_1^{(7)} = u_1^{(8)},$		$\phi^{(7)} = 0.$
Node 8:	$u_1^{(8)} - u_1^{(5)} = \varepsilon_{11}^* L,$		$\phi^{(8)} = 0.$

Resulting in the effective strain in x_1-direction:

$$u_1^{(8)} - u_1^{(5)} = \varepsilon_{11}^*, \tag{A.8}$$

the effective strain in x_2-direction:

$$u_2^{(1)} - u_2^{(2)} = \varepsilon_{22}^*, \tag{A.9}$$

and the effective stress in x_1-direction:

$$\sigma_{11}^* = \frac{rf_1^{(6)} + rf_1^{(7)} + rf_1^{(8)}}{Ht}. \tag{A.10}$$

The previous equations can then be combined, resulting in the normalised Young's modulus E^*:

$$E^* = \frac{\sigma_{11}^*}{\varepsilon_{11}^*} \frac{1}{E_{alu}}, \tag{A.11}$$

and in the macroscopic Poisson's ratio:

$$\nu = -\frac{\varepsilon_{22}}{\varepsilon_{11}}. \tag{A.12}$$

The geometrically nonlinear calculations results are shown in figure A.6. Again, the twisted configurations can only compete with the initial configuration for very high relative densities and small angles of twist. The Poisson's ratio varies greatly depending on the relative density and initial twist.

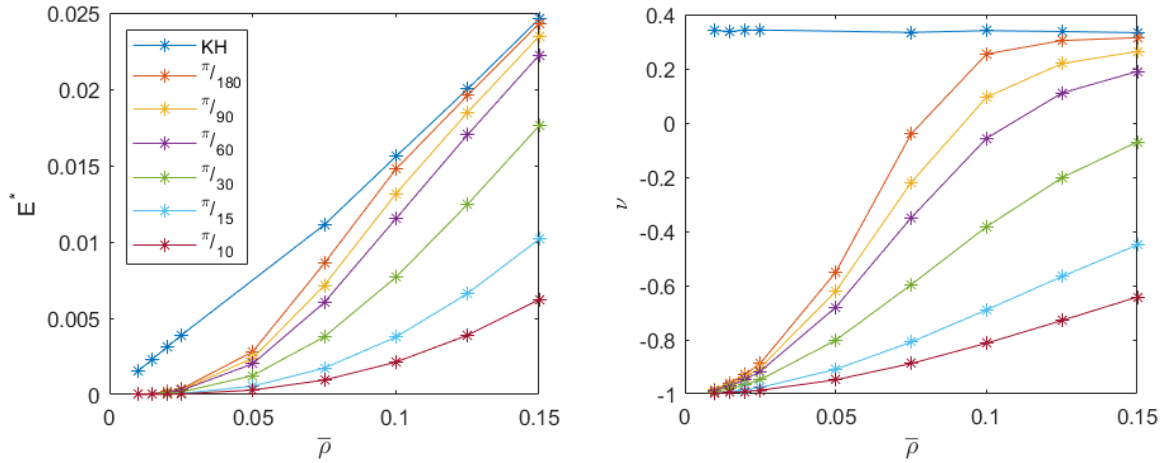

(a) (b)

Figure A.6: $\varepsilon_{11}^* = 0.01$ (a) The normalised Young's modulus E^* as a function of the relative density $\bar{\rho}$ in the geometrically nonlinear setting. (b) The Poisson's ratio ν as a function of the relative density $\bar{\rho}$ in the geometrically nonlinear setting.

An interesting observation can be made by comparing figures A.7 and A.8. In figure A.7 the beams deform when the lattice is exposed to the uniaxial strain, no rotation is observed. The twisted structure initially in figure A.8 rotates the triangles. However, in subfigure (d) a switch happens. No longer is the structure continuing its rotation but now it is deforming the beams in a similar fashion as depicted in figure A.7.

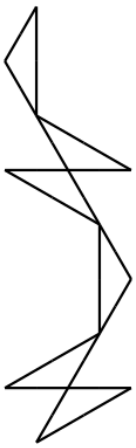

(a) The starting configuration

(b) $\varepsilon_{11} = 0.01$

(c) $\varepsilon_{11} = 0.025$

(d) $\varepsilon_{11} = 0.05$

(e) $\varepsilon_{11} = 0.075$

(f) $\varepsilon_{11} = 0.1$

Figure A.7: Elastic response of a rigidly-jointed KH unit cell with relative density $\bar{\rho} = 0.1$ under uniaxial compression. (a) is the undeformed configuration. Subfigures (b)-(f) shows the deformation of the bars in response to the compressive load.

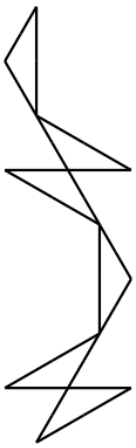

(a) The starting configuration

(b) $\varepsilon_{11} = 0.01$

(c) $\varepsilon_{11} = 0.025$

(d) $\varepsilon_{11} = 0.05$

(e) $\varepsilon_{11} = 0.075$

(f) $\varepsilon_{11} = 0.1$

Figure A.8: Elastic response of a rigidly-jointed KH unit cell with relative density $\bar{\rho} = 0.1$ under uniaxial compression. Where (a) is the starting configuration, with initial twist of $\frac{\pi}{180}$. Subfigures (b)-(c) show the initial rotation of the triangles in response to the compressive load. In subfigures (d)-(f) the rotation of the triangles is no longer continued and instead the bars themselves are being deformed in a similar fashion as the initial configuration of the KH lattice.

B. Tessellated response to uniaxial compression

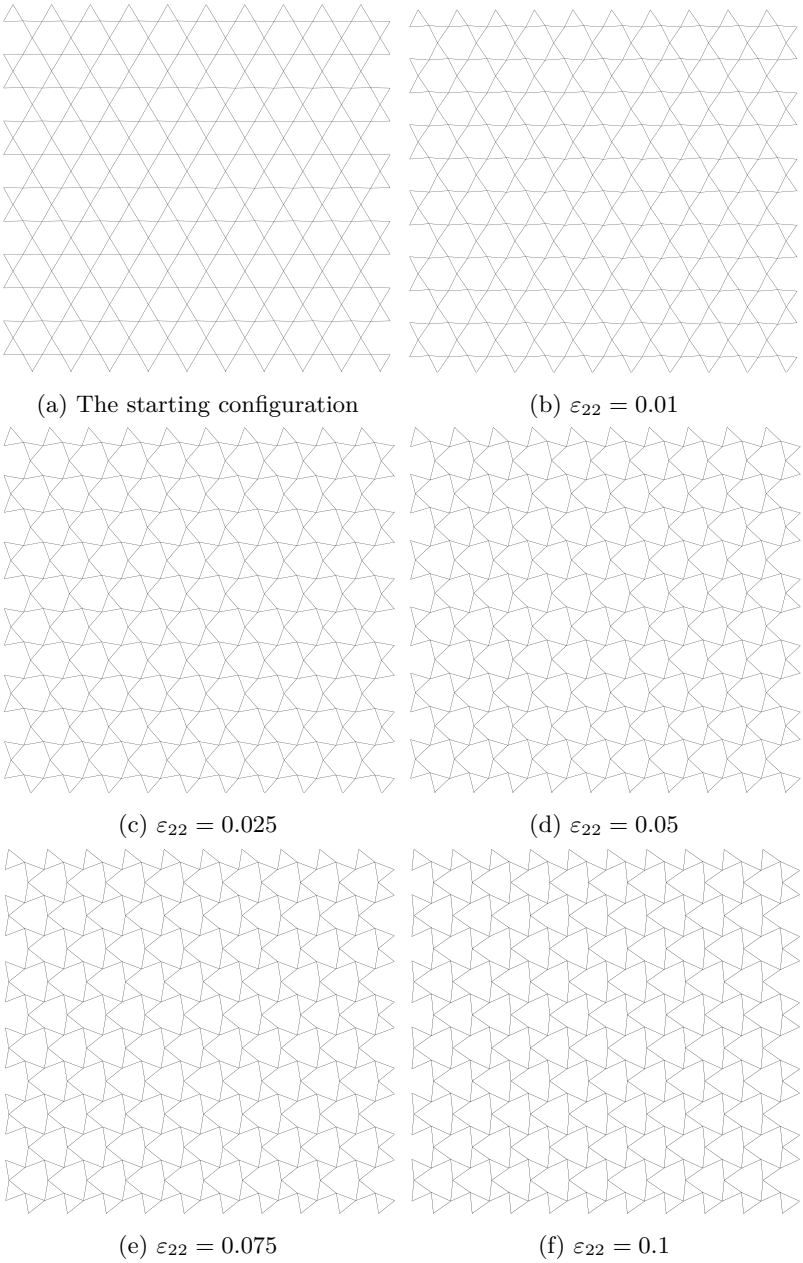

(a) The starting configuration

(b) $\varepsilon_{22} = 0.01$

(c) $\varepsilon_{22} = 0.025$

(d) $\varepsilon_{22} = 0.05$

(e) $\varepsilon_{22} = 0.075$

(f) $\varepsilon_{22} = 0.1$

Figure B.1: The deformation response of a kagome lattice, that has been twisted by an angle of $\frac{\pi}{180}$ see (a), under uniaxial compression. The response as shown in (b)-(f) is reminiscent collapse mechanism of the pin-jointed truss as predicted in section 2.

C. Homogenisation of the Kagome lattice, uniaxial strain E_{11}

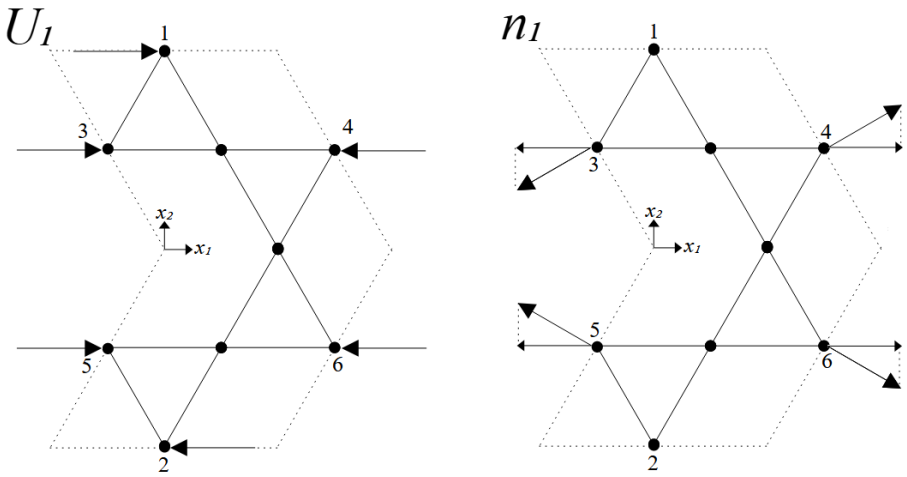

Figure C.1: A uniaxial displacement field U_1 is placed on the representative volume element of the Kagome lattice as can be seen on the left. The normals with respect to the unit cell can be seen on the right.

Figure C.1 shows the prescribed displacement U_1 and the unit normal vectors $\boldsymbol{n}$ associated with the boundary nodes. The macroscopic strain as described in equation 4.5 can be rewritten as the uniaxial strain E_{11}:

$$E_{11} = \frac{1}{V}\sum_{k=1}^{6} n_1^{(k)} u_1^{(k)} ds^{(k)}. \tag{C.1}$$

Expanding the summation of equation C.1 leads to:

$$\sum_{k=1}^{6} n_1^{(k)} u_1^{(k)} ds^{(k)} = [n_1^{(1)} u_1^{(1)} ds^{(1)} + n_1^{(2)} u_1^{(2)} ds^{(2)}] + [n_1^{(3)} u_1^{(3)} ds^{(3)} + n_1^{(4)} u_1^{(4)} ds^{(4)} + n_1^{(5)} u_1^{(5)} ds^{(5)} + n_1^{(6)} u_1^{(6)} ds^{(6)}].$$

The components of the normals are related, namely: $n_1^{(1)} = n_1^{(2)} = 0$ and $n_1^{(3)} = -n_1^{(4)} = n_1^{(5)} = -n_1^{(6)}$, reformulation results in:

$$\sum_{k=1}^{6} n_1^{(k)} u_1^{(k)} = n_1^{(3)} [u_1^{(3)} + u_1^{(5)} - u_1^{(4)} - u_1^{(6)}] ds^{(3)}.$$

The following simplifications can be applied due to the periodicity and symmetry conditions of the unit cell, $u_1^{(3)} = -u_1^{(4)} = u_1^{(5)} = -u_1^{(6)}$, resulting in:

$$\sum_{k=1}^{6} n_1^{(k)} u_1^{(k)} = n_1^{(3)} [u_1^{(3)} + u_1^{(3)} - (-u_1^{(3)}) - (-u_1^{(3)})] ds^{(3)} = 4 n_1^{(3)} u_1^{(3)} ds^{(3)}.$$

$$E_{11} = \frac{4 n_1^{(3)} u_1^{(3)} ds^{(3)}}{V} = \frac{4 \frac{-\sqrt{3}}{2} u_1^{(3)} 2lt}{4\sqrt{3} l^2 t}$$

And finally the uniaxial strain E_{11} can be expressed as:

$$E_{11} = -\frac{2U_1}{L}. \tag{C.2}$$

D. Matlab code: Matrix method

```
%% Lattice input, KH example see unit cell defined in Appendix A
%Number of bars and joints in the unit cell
b = 18;
j = 9;

%Coordinates of the nodes in the unit cell plus the 'imaginary' nodes from outside the unit cell
%
x = [ sym(0) sym(-1/2) sym(1/2) sym(-3) sym(-2)...
     sym(-1) sym(0) sym(-5/2) sym(-3/2) sym(-1/2)...
     sym(1/2) sym(1) sym(2) sym(3/2) sym(7/2)...
     sym(3) sym(4) sym(5/2) sym(2) sym(3/2)...
     sym(5/2) sym(4) sym(3) sym(2) sym(7/2)...
     sym(1) sym(1/2) sym(1/2) sym(-1/2) sym(0)...
     sym(-1/2) sym(0) sym(-1) sym(-3/2) sym(-2)...
     sym(-2) sym(-7/2) sym(-3) sym(-4) sym(-5/2)...
     sym(-7/2) sym(-4)];
y = [ sym(0) sym(-sqrt(3)/2) sym(-sqrt(3)/2) sym(-sqrt(3)) sym(-sqrt(3))...
     sym(-sqrt(3)) sym(-sqrt(3)) sym((-3*sqrt(3))/2) sym((-3*sqrt(3))/2)...
     sym(sqrt(3)/2) sym(sqrt(3)/2) sym(-sqrt(3)) sym(-sqrt(3)) ...
     sym((-3*sqrt(3))/2) sym(-sqrt(3)/2) sym(-sqrt(3)) sym(-sqrt(3))...
     sym((-3*sqrt(3))/2) sym(-2*sqrt(3)) sym((-5*sqrt(3))/2)...
     sym((-5*sqrt(3))/2) sym(-3*sqrt(3)) sym(-3*sqrt(3)) sym(-3*sqrt(3))...
     sym((-7*sqrt(3))/2) sym(-3*sqrt(3)) sym((-7*sqrt(3))/2)...
     sym((-9*sqrt(3))/2) sym((-9*sqrt(3))/2) sym(-4*sqrt(3))...
     sym((-7*sqrt(3))/2) sym(-3*sqrt(3)) sym(-3*sqrt(3))...
     sym((-5*sqrt(3))/2) sym(-2*sqrt(3)) sym(-3*sqrt(3))...
     sym((-7*sqrt(3))/2) sym(-3*sqrt(3)) sym(-3*sqrt(3))...
     sym((-5*sqrt(3))/2) sym(-sqrt(3)/2) sym(-sqrt(3))];

%Alternative input is to define a variable angle and relate the positions of the nodes to each other and the angle

%L1 = 1;      %conveniently only using bars with length 1
%phi = 0;     % Collapse angle of KH
%x(2) = sym(-1/2); y(2) = sym(-sqrt(3)/2);
%x(6) = x(2) - L1*cos(pi/3+phi); y(6) = y(2) - L1*sin(pi/3+phi);
%x(1) = x(2) + L1*cos(pi/3-phi); y(1) = y(2) + L1*sin(pi/3-phi);
%x(7) = x(6) + L1*cos(0-phi); y(7) = y(6) + L1*sin(0-phi);
%x(12) = x(7) + L1*cos(0+phi); y(12) = y(7) + L1*sin(0+phi);
%x(3) = x(1) + L1*cos(pi/3-phi); y(3) = y(1) - L1*sin(pi/3-phi);
%x(5) = x(6) - L1*cos(0+phi); y(5) = y(6) - L1*sin(0+phi);
%x(9) = x(6) - L1*sin(pi/6+phi); y(9) = y(6) - L1*cos(pi/6+phi);
%x(14) = x(12) + L1*sin(pi/6+phi); y(14) = y(12) - L1*cos(pi/6+phi);
%x(13) = x(12) + L1*cos(0-phi); y(13) = y(12) + L1*sin(0-phi);
%x(11) = x(1) + L1*cos(pi/3+phi); y(11) = y(1) + L1*sin(pi/3+phi);
%x(10) = x(1) - L1*cos(pi/3+phi); y(10) = y(1) + L1*sin(pi/3+phi);
%x(4) = x(5) - L1*cos(0-phi); y(4) = y(5) - L1*sin(0-phi);
%x(8) = x(4) + L1*cos(pi/3-phi); y(8) = y(4) - L1*sin(pi/3-phi);


```

```
%Bar lengths, order of the lengths is based on the numbering of the bars in the unit cell
L = [ sym(1) sym(1) sym(sqrt(3)) sym(1) sym(1) sym(1) sym(1) sym(1)...
    sym(1) sym(sqrt(3)) sym(sqrt(3)) sym(1) sym(1) sym(sqrt(3))...
    sym(sqrt(3)) sym(1) sym(1) sym(sqrt(3)) ];
L1 = 1;

%Initial unit cell length, this will need to be related to the collapse angle if the alternative node input is used or if another configuration is used
l = [ sym(4) sym(4) sym(2*sqrt(3))];
%Alternative l = [abs(x(13)-x(5)) abs(x(13)-x(5)) abs(y(10)-y(9))];

%connectivity, take care with the 'imaginary' bars, ordering of the nodes is very important
%Line 63 :Bar 1 is connected to nodes 1 & 2 and does not go through a periodic boundary
%Line 73 :Bar 11 is connected to nodes 2 & 10 but since it crosses a periodic boundary, it is actually node 2 connected to node 8 represented by node 10, therefore the input is 2, 8, 10!
icon(1,1) = 1; icon(1,2) = 2;                                  pbc(1) = sym(1);
icon(2,1) = 1; icon(2,2) = 3;                                  pbc(2) = sym(1);
icon(3,1) = 2; icon(3,2) = 5;                                  pbc(3) = sym(1);
icon(4,1) = 2; icon(4,2) = 6;                                  pbc(4) = sym(1);
icon(5,1) = 4; icon(5,2) = 5;                                  pbc(5) = sym(1);
icon(6,1) = 5; icon(6,2) = 6;                                  pbc(6) = sym(1);
icon(7,1) = 6; icon(7,2) = 7;                                  pbc(7) = sym(1);
icon(8,2) = 4; icon(8,1) = 8;                                  pbc(8) = sym(1);
icon(9,1) = 6; icon(9,2) = 9;                                  pbc(9) = sym(1);
icon(10,1) = 7; icon(10,2) = 9;                                pbc(10) = sym(1);
icon(11,1) = 2; icon(11,2) = 8; icon(11,3) = 10;               pbc(11) = sym(-1);
icon(12,1) = 1; icon(12,2) = 8; icon(12,3) = 10;               pbc(12) = sym(-1);
icon(13,1) = 1; icon(13,2) = 9; icon(13,3) = 11;               pbc(13) = sym(-1);
icon(14,1) = 3; icon(14,2) = 9; icon(14,3) = 11;               pbc(14) = sym(-1);
icon(15,1) = 3; icon(15,2) = 5; icon(15,3) = 13;               pbc(15) = sym(-1);
icon(16,1) = 3; icon(16,2) = 4; icon(16,3) = 12;               pbc(16) = sym(-1);
icon(17,1) = 7; icon(17,2) = 4; icon(17,3) = 12;               pbc(17) = sym(-1);
icon(18,1) = 7; icon(18,2) = 8; icon(18,3) = 14;               pbc(18) = sym(-1);


%% Calculate mechanics for the initial configuration
Baug = sym(zeros(b,2*j+3)); %Augmented Kinematic matrix Baug = [B|C]
%Augmentation of the d vector
for k = 1:2*j
    for i = 1:b
        if (icon(i,3)==k)
            d(2*i-1,1) = (x(icon(i,3))-x(icon(i,2)))*(1/l(1));      %d_11
            d(2*i-1,2) = (y(icon(i,3))-y(icon(i,2)))*(1/l(2));      %d_12
            d(2*i,1) = (x(icon(i,3))-x(icon(i,2)))*(1/l(2));        %d_12
            d(2*i,2) = (y(icon(i,3))-y(icon(i,2)))*(1/l(3));        %d_22
        end
    end
end
```

```
99
100 %Calculation of the Bmatrix
101 for k = 1:j
102     for i = 1:b
103         if (icon(i,1)==k) && (pbc(i) == 1)
104             Baug(i,2*k-1) = Baug(i,2*k-1)-((x(icon(i,2))...
105                 -x(icon(i,1)))/L(i));
106             Baug(i,2*k)=Baug(i,2*k)-pbc(i)*((y(icon(i,2))...
107                 -y(icon(i,1)))/L(i));
108         elseif (icon(i,2)==k) && (pbc(i) == 1)
109             Baug(i,2*k-1)=Baug(i,2*k-1)-pbc(i)*((x(icon(i,1))...
110                 -x(icon(i,2)))/L(i));
111             Baug(i,2*k)=Baug(i,2*k)-pbc(i)*((y(icon(i,1))...
112                 -y(icon(i,2)))/L(i));
113         elseif (icon(i,2)==k) && (pbc(i) == -1)
114             Baug(i,2*k-1)=Baug(i,2*k-1)-pbc(i)*((x(icon(i,3))...
115                 -x(icon(i,1)))/L(i));
116             Baug(i,2*k)=Baug(i,2*k)-pbc(i)*((y(icon(i,3))...
117                 -y(icon(i,1)))/L(i));
118         elseif (icon(i,1)==k) && (pbc(i) == -1)
119             Baug(i,2*k-1)=Baug(i,2*k-1)-pbc(i)*((x(icon(i,1))...
120                 -x(icon(i,3)))/L(i));
121             Baug(i,2*k)=Baug(i,2*k)-pbc(i)*((y(icon(i,1))...
122                 -y(icon(i,3)))/L(i));
123         end
124     end
125 end
126 %Calculation of the C part of Baug
127 for i = 1:b
128     if (pbc(i) == -1)
129         Baug(i,2*j+1) = Baug(i,2*j+1)-pbc(i)*(((x(icon(i,3))...
130             -x(icon(i,1)))/L(i))*d(2*i-1,1));
131         Baug(i,2*j+2) = Baug(i,2*j+2)-pbc(i)*(((y(icon(i,3))...
132             -y(icon(i,1)))/L(i))*d(2*i,1))-pbc(i)*...
133             (((x(icon(i,3))-x(icon(i,1)))/L(i))*d(2*i-1,2));
134         Baug(i,2*j+3) = Baug(i,2*j+3)-pbc(i)*(((y(icon(i,3))...
135             -y(icon(i,1)))/L(i))*d(2*i,2));
136     end
137 end
138
139 B = Baug(1:18,1:18);
140 NullA = null(sym(B')); NullB = null(sym(B));
141 NullBaug = null(sym(Baug));
```

Bibliography

[1] Michael F Ashby et al. *Metal foams: a design guide*. Elsevier, (2000).

[2] C. Ayas and C. Tekoglu. "On the sufficient symmetry conditions for isotropy of elastic moduli". In: *Journal of Applied Mechanics, Transactions ASME* 85.7 (2018).

[3] C.R. Calladine. "Buckminster Fuller's "Tensegrity" structures and Clerk Maxwell's rules for the construction of stiff frames". In: *International Journal of Solids and Structures* 14.2 (1978), pp. 161–172.

[4] H. Cho, D. Seo, and D. -. Kim. "Mechanics of auxetic materials". In: Handbook of Mechanics of Materials. 2019, pp. 733–757.

[5] M. S. A. Elsayed and D. Pasini. "Multiscale structural design of columns made of regular octet-truss lattice material". In: *International Journal of Solids and Structures* 47.14-15 (2010).

[6] N.A. Fleck, V.S. Deshpande, and M.F. Ashby. "Micro-architectured materials: Past, present and future". In: *Proceedings of the Royal Society A: Mathematical, Physical and Engineering Sciences* 466.2121 (2010), pp. 2495–2516.

[7] S.D. Guest and J.W. Hutchinson. "On the determinacy of repetitive structures". In: *Journal of the Mechanics and Physics of Solids* 51.3 (2003), pp. 383–391.

[8] R. G. Hutchinson and N. A. Fleck. "Microarchitectured cellular solids - The hunt for statically determinate periodic trusses". In: *ZAMM Zeitschrift fur Angewandte Mathematik und Mechanik* 85.9 (2005), pp. 607–617.

[9] R.G. Hutchinson and N.A. Fleck. "The structural performance of the periodic truss". In: *Journal of the Mechanics and Physics of Solids* 54.4 (2006), pp. 756–782.

[10] S. Hyun and S. Torquato. "Optimal and manufacturable two-dimensional, Kagomé-like cellular solids". In: *Journal of Materials Research* 17.1 (2002), pp. 137–144.

[11] W.E.D Nelissen. *2D Lattice Materials for Actuation (master's thesis)*. University of technology Delft, Delft, (2018).

[12] W.E.D. Nelissen, C. Ayas, and C. Tekõglu. "2D lattice material architectures for actuation". In: *Journal of the Mechanics and Physics of Solids* 124 (2019), pp. 83–101.

[13] P.R. Onck. "Cosserat modeling of cellular solids". In: *Comptes Rendus - Mecanique* 330.11 (2002), pp. 717–722.

[14] S. Pellegrino and C.R. Calladine. "Matrix analysis of statically and kinematically indeterminate frameworks". In: *International Journal of Solids and Structures* 22.4 (1986), pp. 409–428.

[15] T.N. Pronk, C. Ayas, and C. Tekõglu. "A quest for 2D lattice materials for actuation". In: *Journal of the Mechanics and Physics of Solids* 105 (2017), pp. 199–216.

[16] S. Timoshenko and J. Gere. *Theory of elastic stability*. New York: McGraw-Hill Book Company, 1963.

[17] N. Wicks and S. D. Guest. "Single member actuation in large repetitive truss structures". In: *International Journal of Solids and Structures* 41.3-4 (2004), pp. 965–978.

[18] S. Zhu et al. "Lattice materials composed by curved struts exhibit adjustable macroscopic stress-strain curves". In: *Materials Today Communications* 14 (2018), pp. 273–281.